



POLITECNICO
MILANO 1863

SCUOLA DI INGEGNERIA INDUSTRIALE
E DELL'INFORMAZIONE

Computational study of the hemodynamics in healthy and diseased pulmonary arteries

TESI DI LAUREA MAGISTRALE IN
MATHEMATICAL ENGINEERING - INGEGNERIA MATEMATICA

Author: **Eleonora Sharon Dacatra**

Student ID: 945527

Advisor: **Prof. Christian Vergara**^a

Co-advisors: **Ivan Fumagalli**^b, **Stefano Maria Marianeschi**^c

Academic Year: 2020-21

^aLaboratory of Biological Structure Mechanics (LaBS), Dipartimento di Chimica, Materiali e Ingegneria Chimica “Giulio Natta” Politecnico di Milano, Milan, Italy.

^bModellistica e Calcolo Scientifico (MOX), Dipartimento di Matematica, Politecnico di Milano, Milan, Italy.

^cCardiac Surgery, ASST Grande Ospedale Metropolitano Niguarda, Milan, Italy.

Abstract

The purpose of this work is to provide a computational study of the hemodynamics in the pulmonary artery of two patients with a repaired congenital heart disease (Tetralogy of Fallot). The two patients, after living for years without a pulmonary valve, underwent a pulmonary valve replacement (PVR) operation. We adopt a 3D-0D geometric multiscale coupled fluid dynamics model of the heart circulation based on the Navier-Stokes equations for the 3D domain of the pulmonary artery, reconstructed thanks to the computed tomographies of the patients provided by the Niguarda Hospital of Milan, and on electrical circuit analogies for the rest of the circulation. We propose a novel comparison among a healthy, a pre-operative and a post-operative scenario in order to assess the efficacy of the valve replacement operation in an image-based patient-specific context. Moreover, we perform a study on the flow repartition at the main pulmonary bifurcation based on three different approaches for the imposition of boundary conditions. The method has been implemented in the Finite Element C++ library *Life^X*.

Keywords: Computational fluid dynamics; Pulmonary artery; Geometric multiscale model; Tetralogy of Fallot; Pulmonary valve replacement; Flow repartition.

Abstract in lingua italiana

Lo scopo di questo lavoro è di fornire uno studio computazionale dell'emodinamica nell'arteria polmonare di due pazienti con una cardiopatia congenita corretta (la Tetralogia di Fallot). I due pazienti, dopo aver vissuto per anni senza la valvola polmonare, sono stati sottoposti ad un intervento di sostituzione della stessa. Adottiamo un modello 3D-0D geometrico multiscala e accoppiato della circolazione cardiaca basato sulle equazioni di Navier-Stokes per il dominio 3D dell'arteria polmonare, ricostruita grazie a delle TAC fornite dall'ospedale di Niguarda di Milano, e su delle analogie elettriche per il resto della circolazione. Proponiamo un innovativo paragone tra uno scenario sano, uno preoperatorio e uno postoperatorio per analizzare l'efficacia dell'intervento di sostituzione della valvola in un contesto image-based specifico sul paziente. Effettuiamo inoltre uno studio sulla ripartizione del flusso alla biforcazione principale dell'arteria polmonare basandoci su tre diversi approcci per l'imposizione delle condizioni al bordo del problema. Il metodo è stato implementato nella libreria C++ a elementi finiti *Life^X*.

Parole chiave: Fluidodinamica computazionale; Arteria polmonare; Modello geometrico multiscala; Tetralogia di Fallot; Sostituzione valvola polmonare; Ripartizione del flusso.

Contents

Abstract	i
Abstract in lingua italiana	iii
Contents	v
1 The medical context	1
1.1 Heart physiology and pulmonary circulation	1
1.1.1 Heart physiology	1
1.1.2 The right heart cycle	3
1.2 Pathophysiology of the right heart	5
1.2.1 Tetralogy of Fallot	6
1.2.2 The Ross procedure and its follow-up	9
1.3 A study on the follow-up of a pulmonary valve replacement	10
1.4 State of the art of numerical methods	12
1.5 Purpose of this work	14
2 Imaging and preprocessing	17
2.1 Details on the patients	17
2.2 Physical description of the prosthetic valve	17
2.3 Image acquisition	18
2.3.1 Softwares for imaging	19
2.4 Image segmentation	20
2.5 Overview on the 3D case-scenarios	22
2.6 Definition of the computational domains for the three scenarios	24
2.6.1 Pre-operative and Healthy scenarios	24
2.6.2 Post-operative scenario	27
2.7 Mesh generation	29

3	Mathematical and Numerical models	33
3.1	Blood modeling	33
3.2	3D model: Incompressible Navier-Stokes equations	34
3.2.1	Time discretization of the problem	36
3.2.2	Variational formulation of the problem	36
3.2.3	Backflow stabilization	37
3.2.4	Finite Elements method	38
3.2.5	Algebraic 3D problem	40
3.3	0D model	41
3.3.1	Model derivation: Step 1	42
3.3.2	Model derivation: Step 2	43
3.3.3	Model derivation: Step 3	45
3.3.4	Model definition	47
3.3.5	Time discretization of the 0D model	52
3.4	The 3D-0D geometric multiscale approach	52
3.4.1	Coupling of the models	52
3.4.2	Time discretization of the coupled problem	54
3.4.3	Completing the 3D interface conditions	55
3.4.4	The partitioned algorithm	57
3.4.5	The wall shear stress	58
3.5	Differentiating the 0D outlets	59
3.5.1	Model definition	59
3.5.2	On the choice of the outlet resistances	62
4	Description of simulations and calibration procedures	67
4.1	Description of the different simulations	67
4.1.1	Simulations based on Algorithm 1	68
4.1.2	Simulations based on Algorithm 2	70
4.2	General settings of the simulations	72
4.2.1	Simulation details	72
4.2.2	Mesh-independence study and timestep tuning	72
4.2.3	Typical calibration issues	73
4.3	Calibration of the 0D model parameters	73
4.3.1	About clinical data	74
4.3.2	Initial conditions of the 0D model	75
4.3.3	Tuning of the 0D model parameters	76
4.3.4	Specific calibration on the 0D quantities of Algorithm 2	83

5	Numerical Results	87
5.1	Comparison between the <i>Healthy</i> , <i>Pre</i> and <i>Post</i> simulations	87
5.1.1	Velocity field	88
5.1.2	Pressure field	92
5.1.3	Wall Shear Stress analysis	96
5.1.4	Analysis of 0D quantities of interest	98
5.2	On the importance of differentiating the outlet boundary conditions	100
5.2.1	Study on the flow repartition in the three <i>Healthy</i> scenarios	100
5.2.2	Study on the outlet pressures in the three <i>Healthy</i> scenarios	103
5.2.3	Velocity field	105
5.2.4	Pressure field	109
5.2.5	Wall Shear Stress analysis	110
6	Final remarks, limitations and future developments	113
	Bibliography	117
	List of Figures	125
	List of Tables	129
	List of Symbols	131
	Acknowledgements	133

1 | The medical context

In this first chapter we present an overview of the heart physiology focusing on the pulmonary circulation to give a context on the mechanisms of the heart. We then focus on a specific disease since it affected the two patients we have analysed in this study. The disease is called *Tetralogy of Fallot* and in particular we describe its treatments along with the long-term effects of its repair. We then present a surgical procedure called *Ross procedure*. Finally, we present some of the existing numerical methods in the cardiovascular field and the purpose of this work.

1.1. Heart physiology and pulmonary circulation

The cardiovascular system is composed by three main compartments: the heart, which pumps the blood around the body, the systemic and pulmonary circulations, which respectively carry oxygenated blood to the body and deoxygenated blood to the lungs, and the microvasculature, which is responsible for blood–tissue exchange [42].

1.1.1. Heart physiology

The human heart is composed by four chambers: two atria and two ventricles. The left atrium and the left ventricle make up the left heart (coloured in red in Figure 1.1) which is responsible for the circulation of oxygenated blood around the body. The right heart instead (in blue in the same figure) pumps deoxygenated blood to the lungs to retrieve the oxygen needed by the body. Regarding the terms *left* and *right* referred to the heart, in medicine a common practice is to adopt the patient’s perspective. In this work we will use the medical notation which is inverted with respect to the figures. Left and right heart are separated by the interatrial and interventricular septa which prevent blood transfer between the two sides of the heart. There are two valves connecting respectively each atrium to its ventricle, which are called the atrioventricular valves: the mitral valve connects the left atrium to the left ventricle while the tricuspid valve connects the right atrium to the right ventricle. The other two valves of the heart are also symmetrical for the left and right side and are called semilunar valves. The pulmonary valve connects

the right ventricle with the lungs through the pulmonary artery while the aortic valve connects the left ventricle to the rest of the body through the aorta.

The heart wall is made by three different layers: the most external one is called the epicardium, the middle one is the myocardium and the inner one is the endocardium. The epicardium is surrounded by a membrane called pericardium that separates the heart from the nearby organs and helps its movement [42].

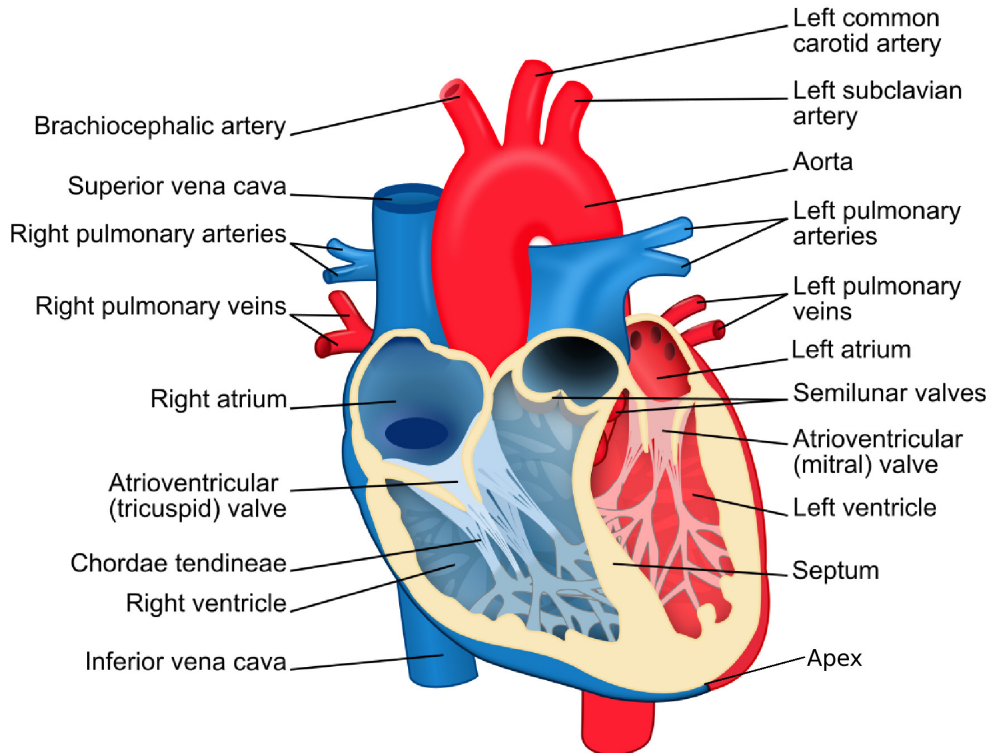


Figure 1.1: The main elements of the human heart [42].

The oxygenated blood coming from the lungs through the pulmonary veins enters the left atrium, then the left ventricle through the mitral valve and finally exits the left heart through the aortic valve which leads to the aorta and to the systemic circulation. The deoxygenated blood, instead, is brought from the body to the right atrium through the superior and inferior vena cava. It then enters the right ventricle through the tricuspid valve and finally exits the right heart through the pulmonary valve which leads to the pulmonary artery and to the lungs.

The heart valves open and close respectively due to two different reasons. They open when the upstream pressure is higher than the downstream one, they close not when the pressure gradient inverts itself, but when the blood flow rate starts to change direction and becomes negative. This way the blood is only allowed to flow in one direction.

The main cause of the blood ejection from the heart to the circulatory system is the ven-

tricular contraction [42]. In fact, in the heart there are cells called cardiomyocytes which have the ability to produce a variation in the membrane voltage if they are stimulated above a certain threshold. In particular these cells have a fast depolarization, a plateau period and then a repolarization phase. There is a short period of time called refractory period in which any further stimulus is inhibited. The action potential is generated in the sinoatrial node, which is located in the right atrium, and is defined as the natural pacemaker of the heart since it imposes its rhythm. This action potential is generated by the opening and closing of ion channels that produce electrical currents through the cell membranes. The cardiomyocytes have a cylindrical shape and are connected through gap junctions that allow the stimulation of a cell to propagate to its neighbouring cells. The signal propagates first through the atria and then through the ventricles, thanks to the atrioventricular node that delays the signal allowing the atria to finish their contraction before the beginning of the ventricular one. The ventricle contraction consists in a longitudinal shortening, a wall thickening and a torsion around the longitudinal axis due to the fibre orientation [42].

We refer to *ventricle systole* as the phase when the ventricles contract and pump the blood out, while to *ventricle diastole* as the phase of relaxation after the systole. The two ventricles contract at the same time and the ventricle diastole lasts about 0.1 seconds while the systole about 0.3 seconds. The relaxation period instead, in which the ventricles stay relaxed after the diastole, lasts about 0.4 seconds making the total time of a heartbeat around 0.8 seconds for a healthy heart [26].

1.1.2. The right heart cycle

The flow of blood during each heartbeat can be seen as a cycle of four main steps [42] and it is equivalent in the left and in the right heart, so we will focus on the right one, since it is our context of interest. We consider an initial configuration in which deoxygenated blood is contained in the right atrium, the tricuspid valve is closed and the right ventricle is contracted, which is point 1. if we refer to Figure 1.2.

- **Ventricular filling** As the deoxygenated blood keeps filling the atrium coming from the superior and inferior vena cava and the coronary sinus (points 10. and 1. in Figure 1.2), at a certain point the pressure of the atrium exceeds the ventricular one, causing the tricuspid valve to open and the blood to enter the ventricle (point 2. in Figure 1.2). The ventricle relaxes as the blood flows in it, first passively, for about 0.15 seconds, due to the atria-ventricular pressure difference, and then actively, for about 0.25 seconds, due to the heart contraction. In this phase we have the systole of the atrium.

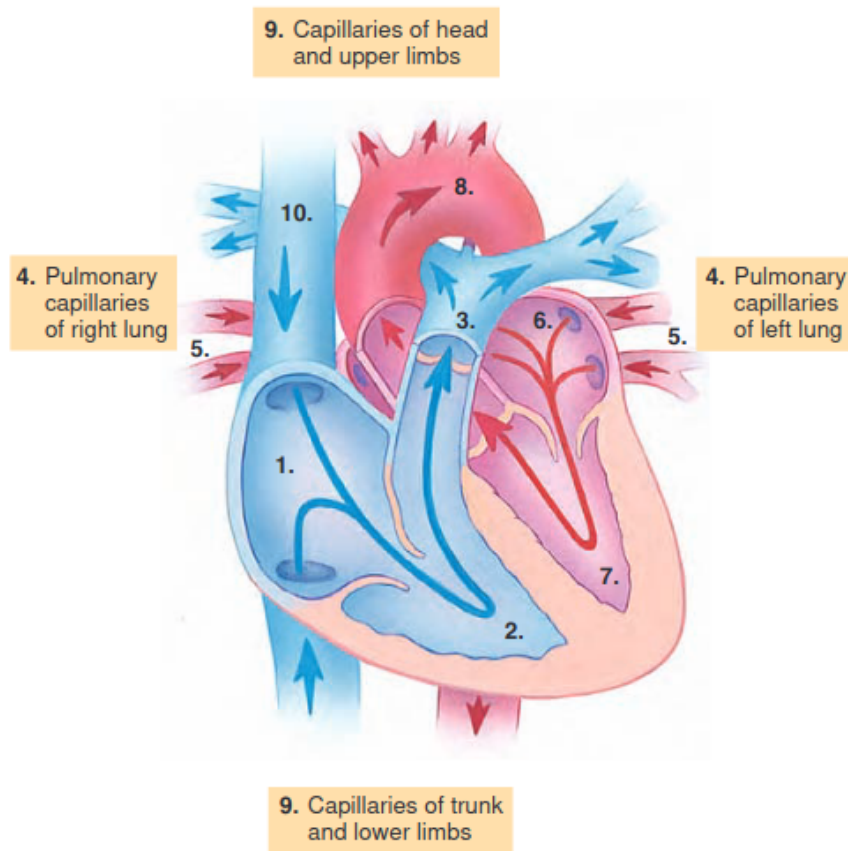


Figure 1.2: A schematic image of blood circulation in the heart [15].

- **Isovolumic contraction** As said, after the contraction of the atrium, the ventricle starts to contract too. Its pressure increases causing a backflow of the blood. The tricuspid valve therefore closes to avoid this and, until the ventricular pressure reaches the one of the pulmonary artery, the ventricle keeps contracting.
- **Ventricular ejection** When the pressure of the right ventricle reaches the pulmonary artery one (around 10mmHg [42]), the pulmonary valve opens and the blood flows to the lungs through the pulmonary artery (points 3. and 4. in Figure 1.2).
- **Isovolumic relaxation** Finally, when the pulmonary valve closes, the ventricle relaxes as the blood reaches the lungs to be oxygenated and later returned to the left part of the heart, in order to be sent to the rest of the body.

As said, the same process occurs in the left heart at the same time, transporting the oxygenated blood coming from the pulmonary veins (point 5. in Figure 1.2) to the atrium (point 6.) and from there through the mitral valve to the ventricle (point 7.) and to the

rest of the body through the aortic valve (points 8. and 9.).

During this process, the pressure of the right heart varies according to Figure 1.3. The pressure of the right ventricle varies in three different ways during its diastolic phase: first it decreases quite rapidly due to the blood filling it, then more slowly and finally due to the systole of the atrium. In particular, time 0 represents the ventricle filling which initially occurs thanks to the pressure gradient between atrium and ventricle. The point labelled as *a* represents instead the atrial systole, which is the active phase of contraction of the atrium that causes the rest of the blood to enter the ventricle. After that, in point *c* the ventricle contracts and reaches the pulmonary artery pressure, leading to the opening of the pulmonary valve. The ventricle then relaxes, while in point *v* the atrium starts contracting again due to the blood flowing in from the lungs. A similar pattern is followed by the left heart, however the values of pressure are much higher since the left heart has to pump the blood around the whole body and not just to the lungs, so its myocardium is thicker in order to exceed higher resistances [42].

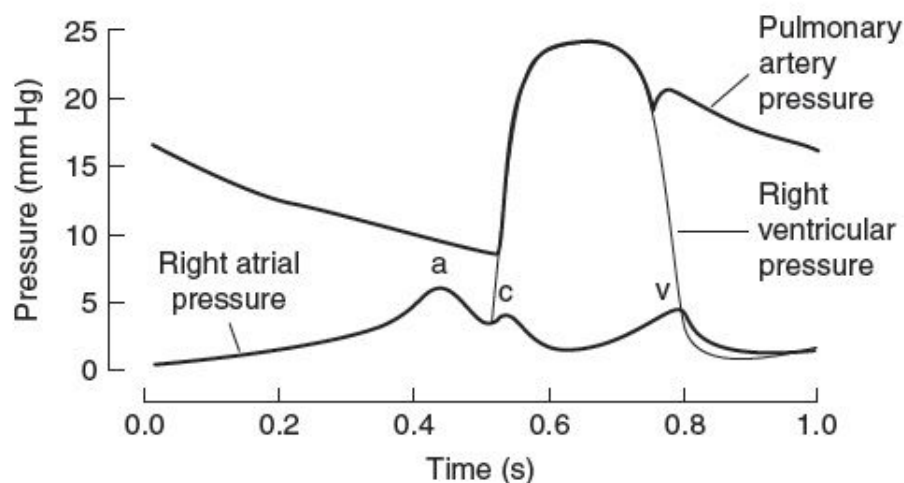


Figure 1.3: Pressure variation of the right side of the heart during a heartbeat [32].

1.2. Pathophysiology of the right heart

Cardiovascular diseases are one of the major causes of death in the world, representing more than 30% of the global deaths per year [21]; in particular, in Europe they are responsible for almost half of the deaths of each year [42]. Some cardiovascular diseases are Congenital Heart Diseases (CHD), which means that they develop during the embryonic growth of a baby. These diseases can cause abnormalities in both the heart structure and its rhythm and therefore affect the blood flow through the heart and to the rest of the body and the development of the organs [17]. In this work we are interested in the

pulmonary circulation, thus in what follows we briefly review some pathologies related to the right heart and the pulmonary artery which affected the two patients under study.

1.2.1. Tetralogy of Fallot

In our work we focused on two patients which were both affected by a congenital heart disease called *Tetralogy of Fallot*. Tetralogy of Fallot (TOF) is one of the most common cyanotic congenital heart diseases; it is indeed estimated that it occurs every one out of three thousand live births [8]. It was first described in 1672 by Dane Niels Stensen and later in 1888 by Étienne-Louis Arthur Fallot (1850 - 1911) after whom it was named. Fallot in his paper called it the "maladie bleue", or "blue disease", which, as the medical term now used of "cyanotic disease", refers to the color blue. The reason is that a characteristic of the babies born with this disease is to have a change in the color of their skin tissue, which becomes slightly blue due to a low level of oxygen in the blood. TOF consists of four features, the first of which is a non restrictive ventricular septal defect (VSD), which means the presence of an opening between the left and right heart. This opening allows the blood to flow freely between the two sides of the heart therefore causing a mixing of the oxygenated blood from the left heart with the deoxygenated one from the right heart. This process can be seen in Figure 1.4 where the situation in *A*, on the left, represents a normal heart, while the one in *B*, on the right, is a heart with Tetralogy of Fallot. In picture *B* the red flow of the oxygenated blood mixes with the blue flow of the deoxygenated blood forming the purple one of poorly oxygenated blood which is sent around the body. The second feature of this disease is linked to the first one and is called an overriding aorta: the aorta is in fact positioned directly over the VSD, instead of over the left ventricle, and therefore the blood entering it isn't just the red one as in a normal heart, but also some of the blue one, causing an increase in the outflow of the aorta. The third feature of TOF is the hypertrophy of the right ventricle (RVH), whose muscle is thicker than in a healthy heart. Finally the fourth feature is a right ventricle outflow tract obstruction (RVOTO) which can be associated to a branch pulmonary artery stenosis, or narrowing [4].

The repair of the Tetralogy of Fallot (rTOF) has evolved over the years. Sometimes an initial palliation can be done at a neonatal age (before the first month of age), especially if the patient has other complications or presents symptoms. We cite the shunt operations which are a group of operations that consist in adding a small synthetic tube between two vessels. In particular, the modified Blalock-Taussig (mBT) shunt can be applied between the innominate artery of the aorta and the right pulmonary artery, as shown in Figure 1.5, on the left, in order to provide a better blood flow to the lungs, reduce hypoxemia (which

is a below-normal level of oxygen in the blood) and allow pulmonary artery (PA) growth [50]. Another initial palliation is the right ventricle outflow tract (RVOT) stenting, which is a procedure that consists in inserting a tiny tube in the RVOT to keep it open.

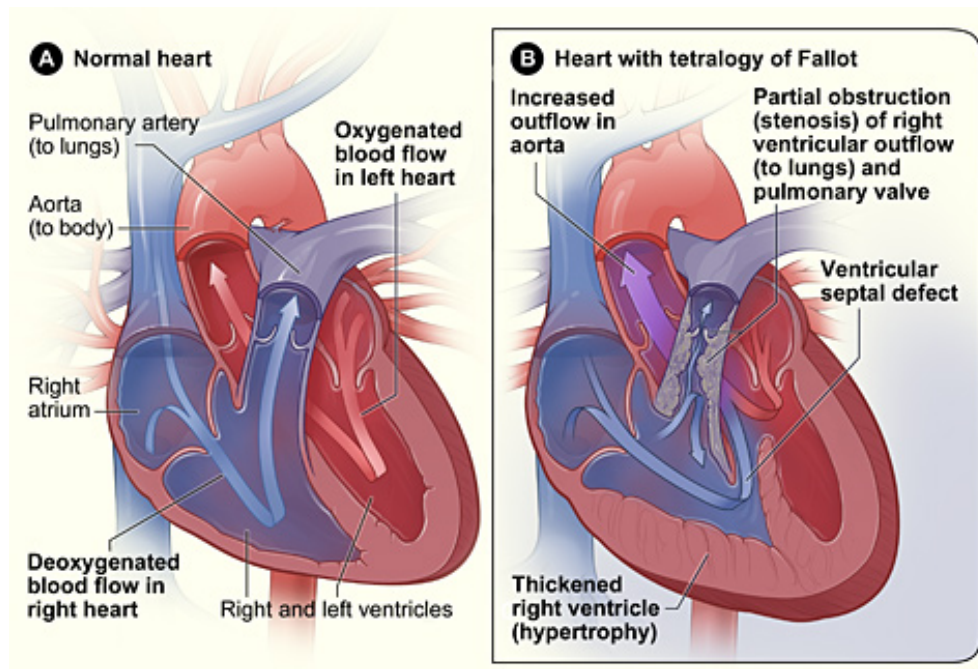


Figure 1.4: Difference between a normal heart (left) and a heart with Tetralogy of Fallot (right) [31].

The complete repair usually takes place in the first couple of years of life in order to limit the pressure load on the right ventricle (RV), reduce the oxygen saturation and preserve the functions of both the cardiovascular system and the brain. However, the exact timing of the procedure is still a matter of discussion among the medical community [9]. The main operations performed in this procedure are shown in Figure 1.5, on the right. The surgeon inserts a patch to close the ventricular septal defect, while, regarding the RVOT there may be the need to remove some muscle below the pulmonary valve or enlarge the pulmonary artery. Moreover, the pulmonary valve may have to be dilatated or reconstructed. [1]. Although the surgical procedures to repair the TOF have improved in time, there is a high risk of complications for patients who have undergone these surgeries, especially as they grow up. A common complication of repaired TOF (rTOF) patients is pulmonary regurgitation (PR), which is a condition where a portion of the blood that should go through the pulmonary artery leaks back to the right ventricle because of a closing defect of the pulmonary valve. While moderate PR can be tolerated for years, if the PR is severe there can be damaging long-term effects like symptomatic RV dilatation and dysfunction [4]. A severe PR means $PR \geq 35\%MR$: the pulmonary regurgitation is more than 35%

of the mitral valve regurgitation [27]. These effects can be enhanced by the presence of distal PA stenosis (i.e. narrowing) or pulmonary artery hypertrophy (PAH).

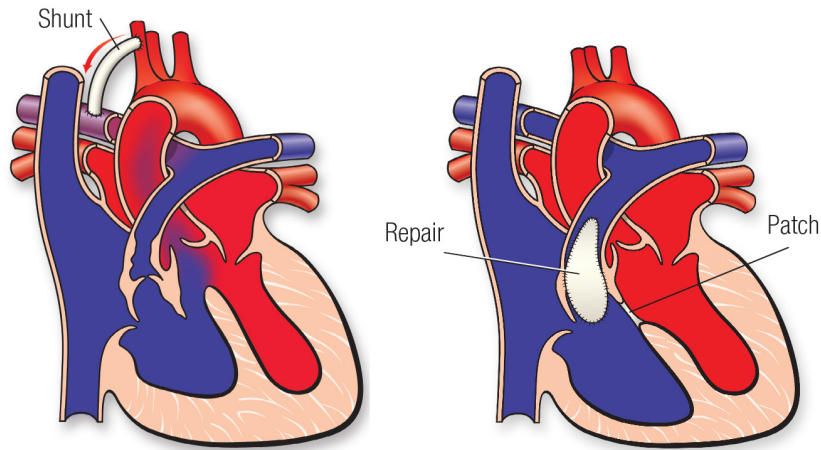


Figure 1.5: Initial palliation (left) and complete repair (right) of TOF [1].

In Figure 1.6 typical rTOF long-term complications are presented. We also cite aortic dilatation and regurgitation, tricuspid regurgitation (TR), residual RVOTO and right and left ventricle dysfunction. In particular, the RV may dilate due to PR and/or RVOTO and this may bring to TR [4].

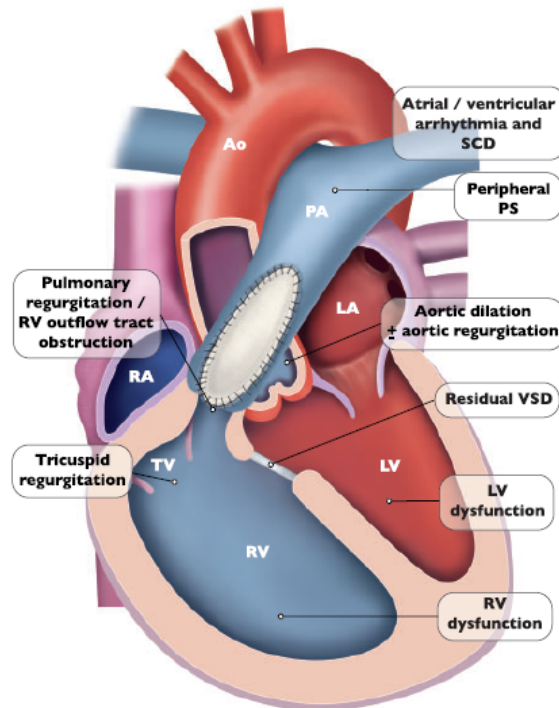


Figure 1.6: Longterm complications of rTOF [4].

1.2.2. The Ross procedure and its follow-up

A specific procedure used to treat some of the patients with CHDs is the *Ross procedure*. Both the patients under analysis have undergone this procedure as infants. This method, also known as switch procedure, pulmonary autograft procedure or two-valve operation, was first described by Donald Ross in 1967 [55] and it consists in the replacement of a diseased aortic valve with the patient's own pulmonary one. This process is shown in Figure 1.7 on the left.

When the aortic valve has to be replaced, inserting a prosthetic valve may not be a good solution: first of all because there are no small-sized aortic valves and this is a problem if the patient is a baby, as it often occurs with CHDs. Moreover, the pulmonary valve, belonging to the patient himself, will grow together with him preventing typical complications that regard prosthetic valves and growth, such as left ventricular outflow tract obstruction [10].

In time, the Ross procedure has been modified iteratively and, after an initial enthusiasm up to the '90s, its usage has decreased due to two main reasons. The first one is that this procedure is very complex since it requires a thorough knowledge of both the pulmonary and aortic anatomy. The second reason is the question of long-term durability [3]. However, in the last ten years, as the technique has evolved, many studies on this procedure have been made and excellent long-term outcomes have been proven [55].

Nowadays it is the only operation of valve replacement with a living valve and it can ensure long-term survival after aortic valve replacement (AVR) with an excellent quality of life and few valve-related complications [10] [55].

The follow-up of this procedure regards the replacement of the removed pulmonary valve with a pulmonary allograft (taken from a donor) or xenograft (animal-derived), as shown in Figure 1.7, on the right. Other options are the implantation of a mechanical valve and the choice between a traditional approach or a percutaneous replacement of the pulmonary valve, which means an operation done without surgery but through a catheter [27].

Indeed, after a Ross procedure, a patient is completely missing the pulmonary valve and must therefore be monitored to establish the best time of intervention for pulmonary valve replacement (PVR). In Milan's Hospital of Niguarda, different factors are taken into account to establish the right moment for the surgery [27]. The monitoring regards, first of all, the presence of symptoms and of a severe pulmonary valve regurgitation (PR), as defined in section 1.2.1. It also assesses the dilatation of the RV: an indication for surgery is if the right ventricle telediastolic volume (which is the volume of the RV at the end of the diastole) is greater than $140\text{ml}/\text{m}^2$, or of its ratio with the systolic one is greater or

equal to either 1.4 with symptoms or to 2.0 without them. Another indicator regards the systolic pressure of the RV which should be either below two thirds of the systemic one with symptoms or below three fourths of it without symptoms. Finally, another indicator is the failure to thrive, which means an insufficient physical growth in the child [27]. Usually, due to PR, 25% of the patients with rTOF need re-operation in 15-20 years [27].

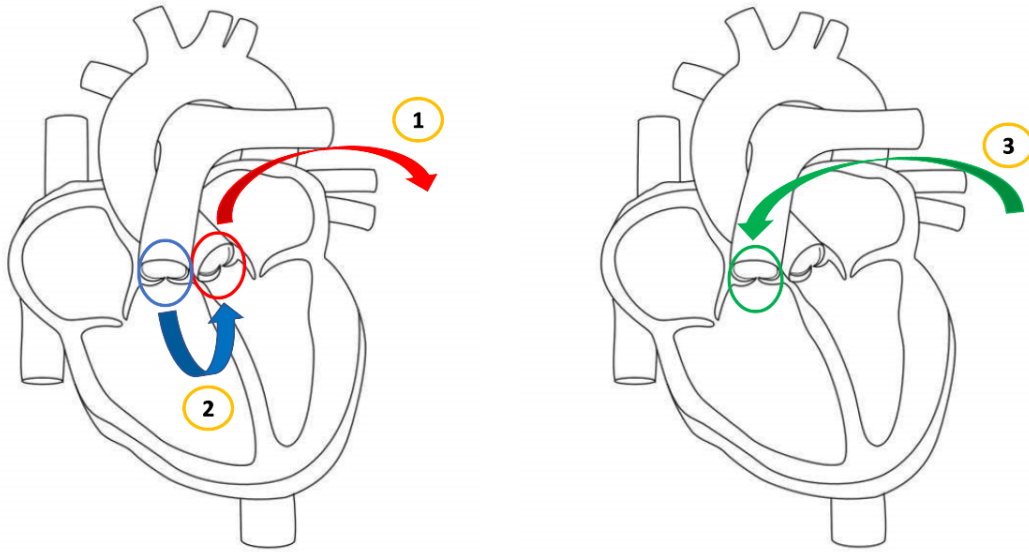


Figure 1.7: The Ross procedure: substitution of the aortic valve with the pulmonary valve (left) and pulmonary valve replacement (right).

1.3. A study on the follow-up of a pulmonary valve replacement

In 2020 a group of cardiac surgeons from the Niguarda Hospital of Milan analysed the mid-to long-term follow-up of a pulmonary valve replacement operation and, in particular, the results of this procedure with the use of the *No – React*[®] Injectable *BioPulmonic*[™] Prosthesis (Bio Integral Surgical, Inc., Mississauga, ON, Canada) [16]. A picture of the prosthetic valve can be seen in Figure 1.8. This prosthesis consists in a porcine pulmonary valve covered with a *No – React*[®]-treated bovine pericardium sleeve and mounted on a self-expandable Nitinol stent, which is a very small tube that helps keeping the pulmonary artery open [16]. The diameter of the prosthesis may vary from 15 to 31mm and it is fully MRI-compatible which means that the valve stent can be seen through the medical exams. The stent corresponds to the triangular-shaped wire which can be seen on the prosthesis in Figure 1.8. This prosthesis has the European Conformity mark certification,

which means that it can be freely implanted in Europe and its main contraindication is endocarditis, which means an inflammation of the endocardium.

Among the surgeons who performed these operations, we cite MD Stefano Marianeschi, the head of the pediatric cardiac surgery division in the Niguarda hospital of Milan, who requested this study and with whom this thesis is in collaboration.



Figure 1.8: The *No – React*[®] Injectable *BioPulmonic*TM Prosthesis (Bio Integral Surgical, Inc., Mississauga, ON, Canada) used in [16].

The study presented in [16] regards 85 symptomatic patients who underwent a pulmonary valve replacement operation from 2007 to 2019. 69.4% of the patients had previously had a repair of the TOF and all of them had echocardiographic scans during the follow-up period. As said, PR causes a long-term volume overload on the right ventricle which can bring the right ventricle to dilatate and fail. There is agreement on the fact that pulmonary valve replacement (PVR) should be adopted in patients with symptoms, however the matter is still controversial for asymptomatic patients [16]. The procedure described in [16] aims at minimizing the invasiveness of the operation while at the same time benefiting of the advantages of a PVR operation with a valve that is available in different sizes, has no risk of coronary artery compression, doesn't have a suture ring therefore avoiding a RVOTO and permits other valve-in-valve procedures if needed. Moreover, this operation doesn't necessary require the use of a cardiopulmonary bypass and the valve is injected in the main pulmonary artery after being folded. Its stent self-expands after the release becoming more rigid due to the heat of the body thanks to the properties of a substance called Nitidol. The valve is then kept into place both by the stent hooks and by four stitches made by the surgeon. This prosthetic valve is a hybrid of the conventional surgical technique, which

is highly invasive, requires a cardiopulmonary bypass and has a higher inside gradient, and the percutaneous PVR, which has as drawbacks the size limitations and the risk of coronary compression. The statistical results of this study showed that this operation is effective to treat chronic PR after the repair of TOF or pulmonary stenosis and the results on durability are so far encouraging [16].

1.4. State of the art of numerical methods

Numerical modeling of the cardiovascular system is a very challenging field for multiple reasons. First of all, the geometrical complexity of the system: the cardiovascular system is in fact composed not just by the heart, which alone is very complex, but also by an intricate network of blood vessels that propagates in all the body. Moreover, there are two different mechanisms that regulate the cardiovascular system: an electrical mechanism and a mechanical one. The cardiovascular system is also characterized by a multiphysics nature. There are solid structures like the vessel walls, which deform and exert forces, and there is the blood, which on the other hand is a fluid that interacts with the vessel walls while flowing. Another characteristic of this system is its multiscale nature, since its different parts can have very different sizes making it hard to model everything together [42]. Due to these reasons, a typical way used to simulate the cardiovascular system is to identify a specific zone of interest, which is modelled more accurately, and couple it into an integrated model which describes the rest of the system.

A very big challenge when dealing with the modeling of the cardiovascular system is the lack of data; clinical data is indeed essential for different purposes. To be able to construct the computational domains, clinical radiological images, like computed tomography (CT) and magnetic resonance imaging (MRI), are needed. These images can however sometimes not be accurate enough for the mathematical tools to be able to work properly in identifying the anatomy of the zone of interest. Another important set of data is the one regarding the boundary conditions. Indeed, when using the approach of dividing the model into compartments, even if this simplifies the modeling process, a new challenge arises too. In fact, the boundary conditions needed for the compartment of interest are not just the ones on the physical boundaries, but also the ones on the computational boundary where the zone of interest is truncated. However, often these quantities are not available from normal medical exams and should have to be acquired with invasive measurements. Finally, an important challenge is patient-specificity since blood vessels, like all body parts, vary from person to person and this greatly affects the different mechanisms of the system [42].

In spite of these challenges, there are many cardiovascular models in literature that have

been applied to both simulate healthy states, in order to understand them better, and to study pathological conditions.

Regarding multidomain coupled models, we cite [40] where, for the first time, a 0D model is not just introduced for the calculation of the boundary conditions of the higher order model, but a genuinely heterogeneous multiscale approach is adopted by coupling the two models at a mathematical and numerical level. Regarding 3D-0D models, in [41] the authors deeply analyse the geometric multiscale approach for blood flow problems focusing both on the stand-alone problems (3D, 1D and 0D) and on their coupling (3D-1D and 3D-0D). This work also describes the “defective problems” that arise because of the interface coupling of heterogeneous models and proposes different mathematical techniques to overcome them. In [42] a complete list all the steps of mathematical modeling of the cardiovascular system is presented. The authors describe the basic physical principles behind cardiac physiology and detail the main difficulties and different techniques both of image acquisition and of computational modeling. Finally, we cite [45] which contains the description of an electromechanical model of the human heart that focuses on the left ventricle. The employed lumped parameters model for closed-loop blood circulation is the one we have adopted in this study, although we have focused on the pulmonary artery instead.

Regarding the pulmonary circulation and right side of the heart, until recently there existed very few studies. However, there has been an increased interest in this topic in the last decade, particularly in the last couple of years, since the COVID virus, which, affecting the lungs, can subsequently affect this part of the heart. In [24] an FSI model is presented for a healthy patient-specific pulmonary arterial tree using a variational multiscale approach. In particular, this paper adopts a formula to calculate the resistances at the outlets of the patient-specific domain in the coupled algorithm, which is described in [56] and adopted in our work. The work in [48] studies instead the hemodynamics in the pulmonary arteries both under resting and exercise conditions. It adopts a rigid wall assumption and reports the results of the flow split between the right and left pulmonary arteries of the six patients under analysis.

Among the studies on the diseases of the pulmonary circulation, we cite [22], where patient specific data is applied to a three-element windkessel model in order to quantify the right ventricular afterload in patients with and without pulmonary hypertension. The work in [49] focuses instead on the Wall Shear Stress (WSS), employing a combined MRI and computational fluid dynamics (CFD) approach to study whether the WSS is reduced in the proximal pulmonary arteries of PAH patients. The proposed idea is that reduced shear stress may contribute to pulmonary endothelial cell dysfunction and, as a result, to PAH progression. Regarding the main disease relevant to this work, [9] simulates the

blood flow in the pulmonary bifurcation for adult patients with rTOF. The authors underline the importance of studying the pulmonary bifurcation for patients affected by this disease and compare the different results of imposing averaged boundary conditions and patient-specific ones. It considers a rigid-wall assumption, in accordance with [11], claiming that the results, since they regard a large artery as the pulmonary one, would not differ significantly from those predicted when dynamic arterial compliance is taken into account [9]. This last work is the continuum of a previous one, [8], where a 2D model is instead adopted and two different ways to study the flow repartition at the pulmonary bifurcation are considered: in particular, Murray's law and a "splitting law" proposed by [12]. The work in [17] adopts instead a reduced model to decrease the complexity of patient-specific simulations for seventeen TOF patients.

Regarding the pulmonary valve, we cite [59], which is a medical paper that evaluates the feasibility of the implantation of a self-expandable valved stent. Finally, [34] addresses the issue of right ventricle dilatation after pulmonary valve replacement (PVR) in patients with rTOF and assesses whether the preprocedural estimates on post PVR RV volume should be used as an indicator for the timing of the surgery.

1.5. Purpose of this work

The purpose of this work was to provide a computational study of the hemodynamics in the pulmonary artery of two specific patients who lived for years without a pulmonary valve after a Ross procedure and underwent the pulmonary valve replacement (PVR) operation described in section 1.3, with the implantation of a prosthetic valve. In particular, we propose here a novel comparison among a healthy, a pre-operative and a post-operative scenario in order to assess the efficacy of the valve replacement. The patient-specific 3D geometries of the pulmonary arteries of the patients were reconstructed from post-operative medical images provided by the Niguarda Hospital of Milan and used as computational domains for the blood flow simulations. In particular, our zone of interest was the one of the pulmonary artery, from the valve stent to the region after the first bifurcation.

We adopted a 3D-0D geometric multiscale coupled fluid dynamic model of the heart circulation based on the Navier-Stokes equations for the 3D domain of the pulmonary artery and on RLC circuit analogies for the rest of the circulation.

The main novelties of this work are:

- The application of an image-based patient-specific 3D-0D model of the cardiovascular system for fluid dynamics simulations on patients with a repaired congenital heart disease (Tetralogy of Fallot) and in particular after a Ross procedure.

- The analysis of three different scenarios: a *Healthy* one, adopted as reference, and two scenarios following the history of the two patients of interest in their pre-operative (*Pre*) and post-operative (*Post*) conditions with respect to the PVR operation.

This thesis is structured as follows.

Chapter 2 concerns the imaging and preprocessing techniques that were applied in order to obtain, from the CT scans of the patients, the final 3D meshes of their pulmonary arteries for the CFD simulations in the three scenarios.

In Chapter 3 we present and detail the adopted 3D-0D numerical method which is implemented in the Finite Element C++ library *Life^X* [23].

In Chapter 4, we detail the simulation settings and describe the calibration procedure of the model. Finally, in Chapter 5 the results of our study for all the scenarios are presented and discussed. Multiple heartbeats are simulated and the outcomes are presented through 3D visualizations obtained at different instants of important hemodynamics quantities and through 2D plots of mean values of interest. In section 5.1 we analyse and compare the results for each scenario obtained with a model in which the two branches of the pulmonary artery are subject to the same boundary conditions. In section 5.2, instead, we investigate the influence of differentiating the two outlet boundary conditions of the artery, focusing on the flow repartition at the main pulmonary bifurcation.

2 | Imaging and preprocessing

In this chapter we describe the adopted process to segment the medical images into 3D geometries of the pulmonary arteries of the two patients. The aim was to use the obtained patient-specific 3D geometries to computationally simulate the flow of the blood in the three scenarios of interest: *Healthy*, *Pre* and *Post* pulmonary valve replacement (PVR) operation. We then describe the preprocessing techniques that were employed in order to obtain the final 3D meshes.

2.1. Details on the patients

Our goal was to analyse two different patients. The first one, which we will refer to as Patient 1, was a man with rTOF who had undergone a Ross procedure as an infant. He then lived for many years without a pulmonary valve, until, in April 2007, he underwent the pulmonary valve replacement (PVR) procedure described in section 1.3 at the Niguarda Hospital of Milan, with the implantation of the *No – React*[®] Injectable *BioPulmonic*TM Prosthesis (Bio Integral Surgical, Inc., Mississauga, ON, Canada). The CT scans at our disposal for this patient were from 2019, twelve years after the surgery of interest, when the patient was sixty six years old.

The second patient (which we will refer to as Patient 2 from here on) was also a man born with TOF who underwent a Ross procedure as an infant and had a subsequent pulmonary valve replacement operation with the same prosthetic valve. The CT scans that we analysed for this patient were from 2017 when he was forty two years of age.

2.2. Physical description of the prosthetic valve

Since the CT scans were taken after the PVR operation, at the moment of the scans both patients had the prosthetic valve implanted. The shape of the prosthetic stent is similar to a hexagonal prism and both the six vertices of its lower base and the six ones of its top base are visible through the medical exams. Contrary to the stent, the valve leaflets,

which give to the valve the open and closed configuration, are not detectable through the medical exams. To overcome this problem, we adopted for the simulation of the leaflets an electrical diode, belonging to a 0D model which simulates the rest of the circulation with a lower spatial resolution compared to the one in the 3D pulmonary artery reconstruction. More details about the 0D model are presented in section 3.3.

Thanks to the detection of the stent's base points from the CT scans, it was possible to deduce the shape and orientation of the valve and see how it altered the domain where the blood flowed by channeling the blood from the right ventricle into the pulmonary artery through a more regular geometry. This phenomenon is schematically shown in Figure 2.1, where on the left there is a diagram showing the blood entering the pulmonary artery when no prosthetic valve is implanted. On the right, instead, we can see the modified and narrowed inflow of the artery caused by the prosthetic stent.

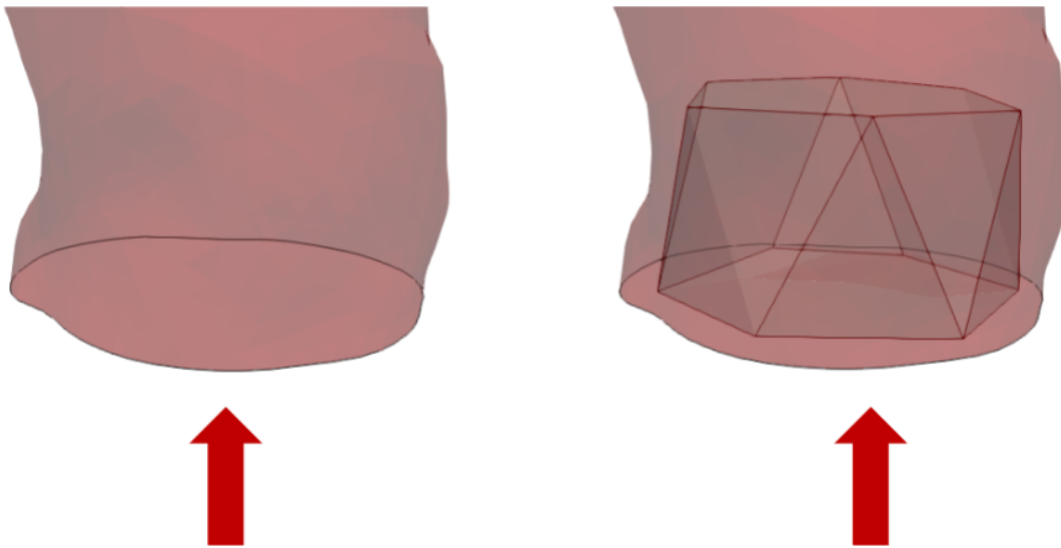


Figure 2.1: Left: Natural inflow of the pulmonary artery. Right: Post PVR inflow with the valve stent.

2.3. Image acquisition

The medical images at our disposal were provided by the Niguarda Hospital of Milan and in particular by the head of the pediatric cardiac surgery division: MD Stefano Marianeschi. The medical data consisted in Computed Tomographies (CTs), taken as regular follow-up exams of the PVR operation.

Reconstructing the walls of arteries and veins is a very challenging process, indeed these

vessels may be very irregular and present many bifurcations. Moreover, in case of patients with pathologies, the variability may be even larger [42]. There are different imaging techniques in the medical field. We cite the volume CT since it is the one used by the Hospital of Niguarda for these patients' follow-up exams. This technique makes use of a radio-opaque dye which is injected in the arteries in order to make their lumen (i.e. their inside space) brighter and therefore more distinguishable. Two-dimensional X-ray sources are rotated around the patient's body and the beams they create are projected onto some screens. The different absorption properties of the various body structures produce different contrasts on the screens allowing to create 3D images with high spatial resolution [18]. While conventional CT makes use of row detectors and produces many 1D images, which are then put together to form a 2D image, with this technique multiple two-dimensional images are obtained directly through area detectors. These images are then stored in matrices whose components are the grey-scale intensities of the acquisition points.

The images may have to be enhanced by performing techniques such as *resampling* (suitably changing the resolution of an image in some directions) or by applying *smoothing filters*, being careful to avoid the blurring of boundaries of interest. These processes are sometimes necessary because the images may contain some noise.

The CT scans of the two patients were initially in the standard Digital Imaging and COmmunications in Medicine (DICOM) format and were then converted in the MetaImage MetaHeader (mhd) format using *mitk*, which is a free open-source software for the development of interactive medical images [29]. The mhd format allows the visualization of the medical image on three different planes at the same time. The planes can be tilted and translated in order to better identify the zone of interest. Figure 2.2 shows an example of a possible visualization of Patient 1's scans in mhd format. The pulmonary artery and part of its stent are clearly visible.

2.3.1. Softwares for imaging

Most of the operations on the images were carried on with *The Vascular Modeling Toolkit* (VMTK) [51]: a collection of tools for the 3D reconstruction, mesh generation and surface data analysis for image-based modeling of blood vessels. This library makes use of other two open source libraries: The Visualization Toolkit (VTK) [52] and The Insight Toolkit (ITK) [19]. In particular, VMTK was first adopted for the process of mesh construction and then for the different preprocessing operations. Some of the adopted methods belong to an extension of the VMTK code which is described in [14] and available in a fork of VMTK [13].

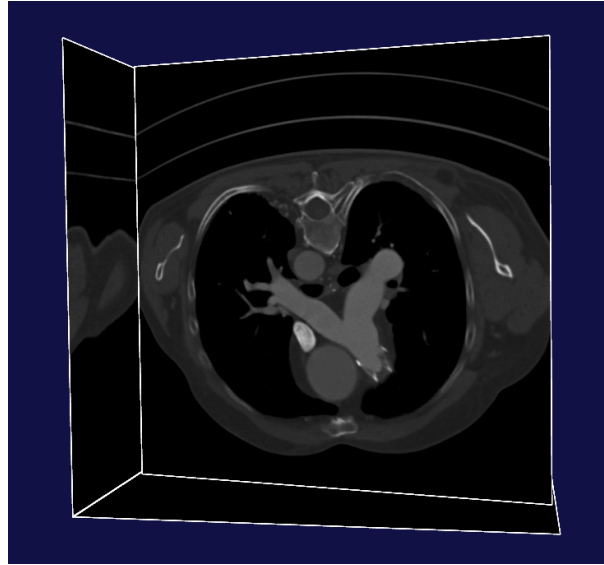


Figure 2.2: Patient 1. Example of a CT scan in mhd format.

Along with this software, another platform that we have used is Paraview. Paraview is an open-source, multi-platform data analysis and visualization application [33]. This platform was both useful for the preprocessing of the mesh alongside VMTK and for the 3D visualization of the results.

Finally, we cite Matlab [28] which is a programming and numeric computing platform that was used in a specific operation of the mesh generation described in section 2.7.

2.4. Image segmentation

Starting from the images in mhd form, the segmentation procedure was performed in collaboration with [37]. Image segmentation consists in the reconstruction of an image by identifying its borders. Regarding the pulmonary artery of a patient, this means detecting some points which belong to the lumen and which will make up the superficial mesh and the border of the domain of the 3D artery where the simulated blood will flow.

The first step of the segmentation process is to set the artificial boundaries of the vessel under analysis. Indeed, while the physical boundary of the lumen, which is the artery wall, is defined by the geometry itself, the artificial boundaries have to be set by the user. Considering that the blood only flows in one direction, one can define as *inlet* the boundary where the blood enters the domain of interest and as *outlets* the boundaries from which it exits. These labels are shown in Figure 2.3.

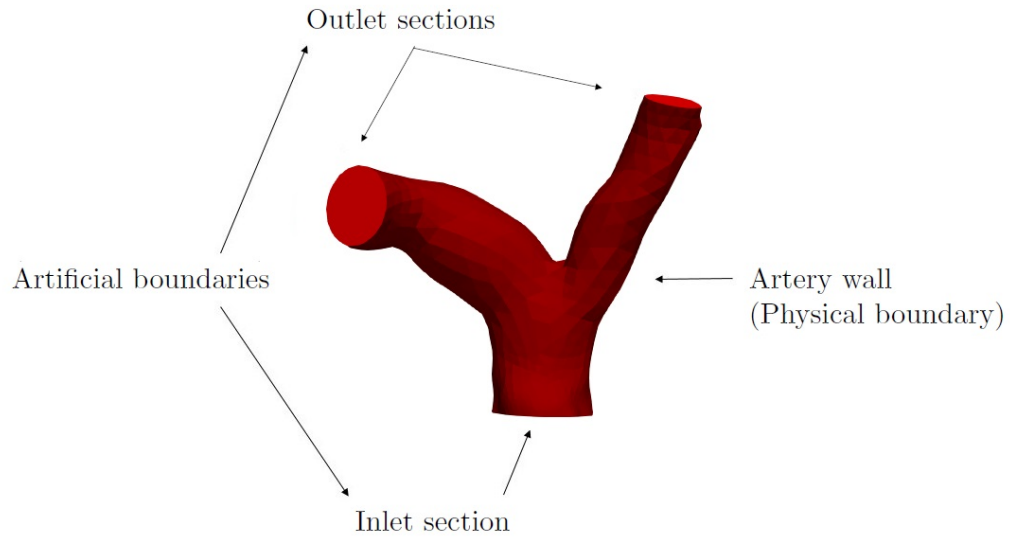


Figure 2.3: Example of physical and artificial boundaries of a pulmonary artery.

To define the inflows, one must manually set one or more seeds per each of them, while, for each outflow, one or more targets. An example of this process can be seen in Figure 2.4, where, on the left two seeds (in red) are being positioned at the artery inflow, while on the right two seeds are set for each of the two outflows.

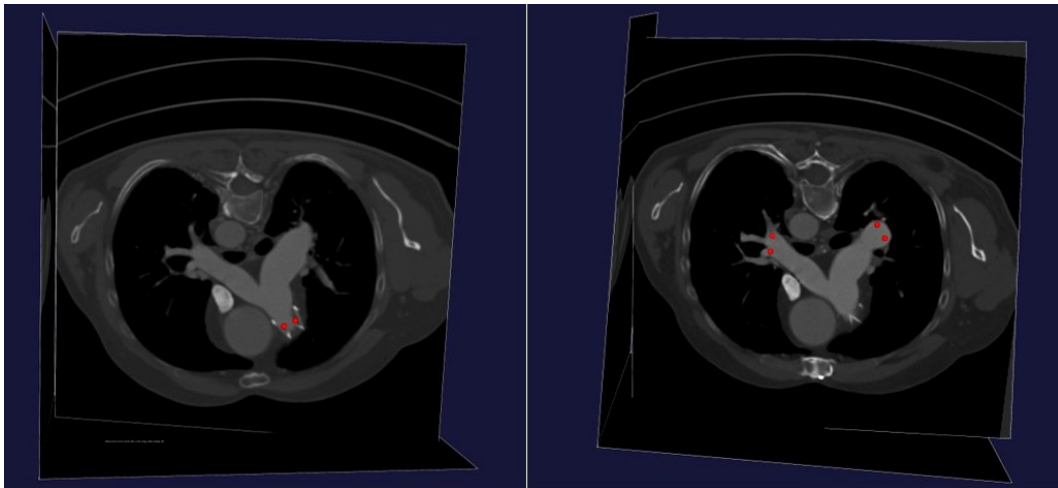


Figure 2.4: Example of placement of the seeds at the inflow (on the right) and at the outflows (on the left) with VMTK.

The images of the two patients under study were initially segmented using the *thresholding* method, which consists in defining a threshold k such that all the image points with grey-scale intensity greater than k will belong to the reconstructed wall. The idea is that this threshold separates different anatomical structures and, in particular, the artery wall

from the inside of the lumen. Once chosen the best value for k , the *front propagation* technique has been employed. This technique consists in generating waves from each seed and making them travel to the targets. In particular, the wave slows down in the regions where the grey-scale intensity changes rapidly, while it propagates fastly in regions where the intensity changes are more gradual [42].

It was then necessary to reconstruct for both patients the part of the artery containing the valve stent, since the initial reconstructions were very irregular in this zone. This was due to the fact that vessel walls have different grey-scale values with respect to the valve stent and for this reason they may not be properly reconstructed. The reconstructing process consisted in creating with Paraview a more regular surface to be adapted into the wall of the artery and in the removal of the points of the wall that had not been properly segmented [37].

The results of the described operations, which were adopted as initial reconstructions of the pulmonary arteries of the two patients, are shown in Figure 2.5. On the left the reconstructed artery of Patient 1, on the right the one of Patient 2.

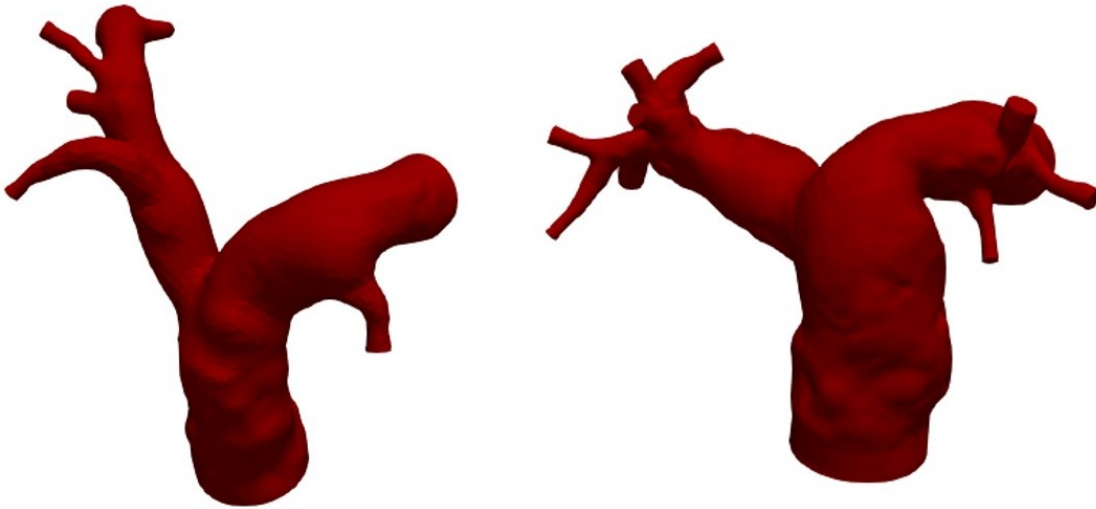


Figure 2.5: Reconstructed geometries of the pulmonary arteries from the CT scans of Patient 1 (left) and Patient 2 (right).

2.5. Overview on the 3D case-scenarios

After these steps, performed in collaboration with [37], we introduced novel elaborations of the reconstructed images and proceeded by modifying the obtained geometries in order to simulate three different scenarios:

- A *Healthy* scenario with a functioning and natural pulmonary valve,
- A Pre-operative (in what follows *Pre*) scenario corresponding to the situation before the PVR operation, therefore in absence of the pulmonary valve,
- A Post-operative (in what follows *Post*) scenario corresponding to the situation after the PVR operation, with the prosthetic valve implanted.

The only medical exams at our disposal, however, were the ones of the patients in their post-operative condition. We therefore assumed some hypothesis to recreate the geometrical shapes for the other two scenarios. The main difference between the *Healthy* and the *Pre* scenarios consists in the presence or absence of the natural pulmonary valve, which was taken into account through the addition or removal of a diode in the 0D model. From the 3D point of view, we decided to consider, in the *Healthy* and in the *Pre* scenarios, the native geometries of the pulmonary arteries of the two patients, taken from the post-operative medical exams, while disregarding the valve stents. The underlying hypothesis was that the prosthetic valve does not modify significantly the artery of the patient, so the lumen shape after the operation is similar to the one the patient had before the operation and also to the one of a healthy person. In reality, while it is quite true that the prosthesis does not modify significantly the walls of the artery, so this assumption is well justified for the *Pre* scenario, the native shapes of the patients' arteries, may differ from the ones of completely healthy conditions. Therefore, in our simulations for the *Healthy* scenario, we aimed at obtaining the best possible results for a patient having a functioning natural valve but that specific and possibly pathological shape of the artery.

Regarding the *Post* scenario, instead, we considered the geometry of the artery taking into account this time of the stent of the implanted prosthetic valve.

In Figure 2.6 we schematically present the three scenarios. On the left we show how we modelled the *Healthy* scenario, by considering the natural wall of the patient's artery and coupling the 3D geometry with a 0D model that contained a diode representing the natural pulmonary valve with its opening and closing leaflets. At the center of the same figure there is instead the representation of the *Pre* condition of the patients. The geometry is, as said, the same one as the one adopted for the *Healthy* scenario, but the diode representing the pulmonary valve in the 0D model is no longer present because of the absence of the pulmonary valve in the patient. Finally, on the right, we can see the configuration for the *Post* condition of the patients, composed by a functioning valve (diode) as in the healthy case, imitating this time the prosthetic leaflets, but with a different geometry of the inflow lumen, given by the stent of the prosthesis.

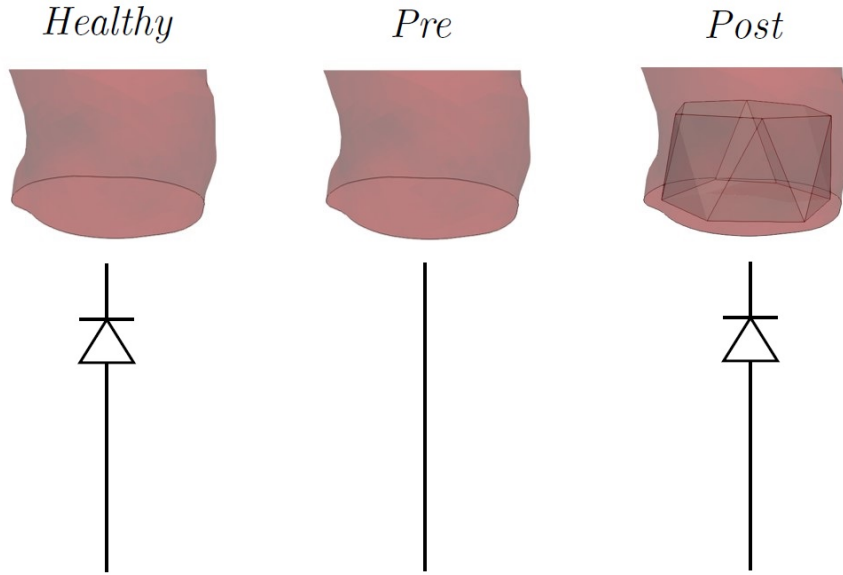


Figure 2.6: Diagram of the modeling of the three scenarios: *Healthy* (native geometry + diode), *Pre* (native geometry, no diode) and *Post* (stent geometry + diode).

2.6. Definition of the computational domains for the three scenarios

Considering the three listed scenarios, we had to construct two different 3D domains for each patient: one representing both the *Healthy* configuration and the *Pre* one, without the prosthetic valve, and one simulating instead the *Post* condition with the implanted prosthesis. The rest of the chapter will be dedicated to the description of the construction of these two geometries.

2.6.1. Pre-operative and Healthy scenarios

In the reconstruction we had performed of the pulmonary arteries of the two patients, we had eight and twelve outlets for Patient 1 and Patient 2, respectively, see Figure 2.5. Both geometries were composed by the pulmonary trunk, the two main outflow tracts, corresponding to the two main branches of the pulmonary artery (left and right) and some other smaller outflows that spread out from the main branches. For our analysis, however, the zone of interest consisted mainly in the pulmonary valve zone and in the first bifurcation. Indeed, the proper functioning of the pulmonary valve mostly influences, from a fluid dynamic point of view, the main trunk of the artery and the two main branches, while the effects on the smaller ones are much less evident. We therefore decided to cut

out the smaller outlets, leaving just the two main ones. This process can be seen in Figure 2.7. In configuration A) we can see the arteries with all the outlets, at the top for Patient 1 and at the bottom for Patient 2. In configuration B), instead, we can see the new geometries with just two outlets for both patients. These geometries were obtained with the command *clip* of Paraview for the cutting followed by VMTK's *vmtksurfacecapper* to close up the holes in the walls.

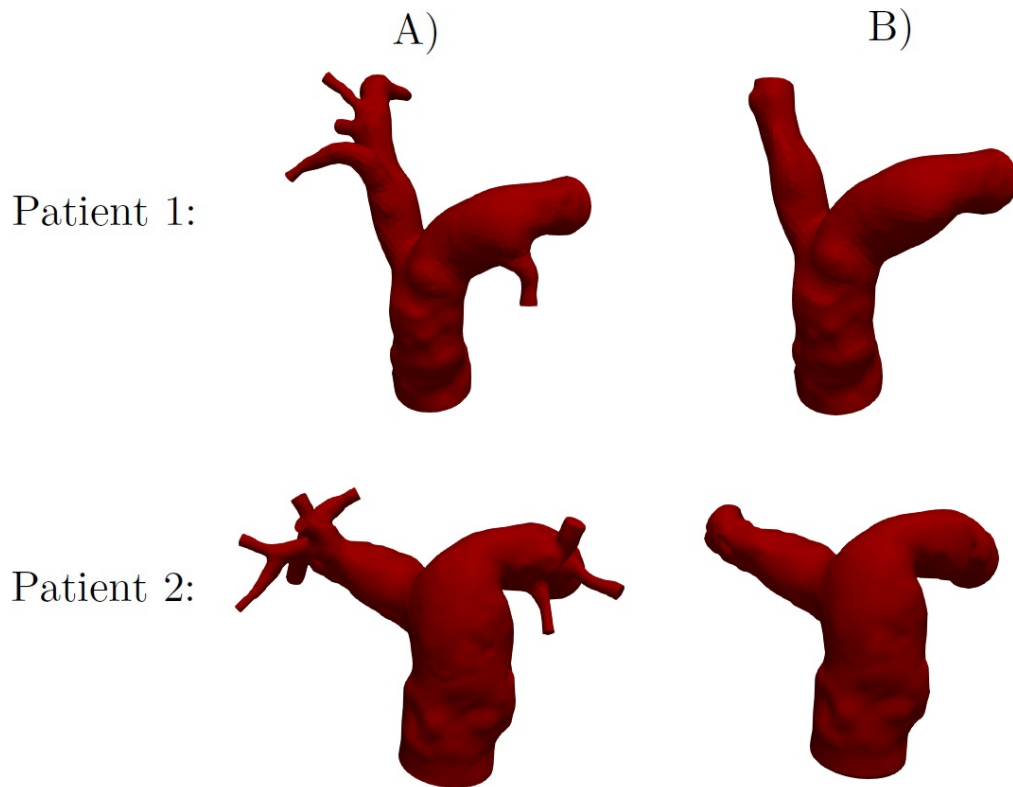


Figure 2.7: A) The pulmonary arteries with all the outlets for Patient 1 (top) and Patient 2 (bottom). B) The pulmonary arteries with just the two main outlets for Patient 1 (top) and Patient 2 (bottom).

Moreover, we performed a cut of a part of the domain's inflow. The reason is that we wanted the artery domain to have as inflow zone the one that in the *Post* scenario corresponded to the prosthetic valve zone, in order to have two geometries (*Healthy/Pre* and *Post*) of the the same length. Moreover, since the valve leaflets were simulated in the 0D model, it was fundamental to define as inlet for the pulmonary arteries of both patients the section which coincided with the beginning of the stent.

First of all, we identified the stent from the medical images. In Figure 2.8 we can see the detection of the six stent's base points performed with VMTK through the command *vmtkimageseeder*, by placing some red dots.

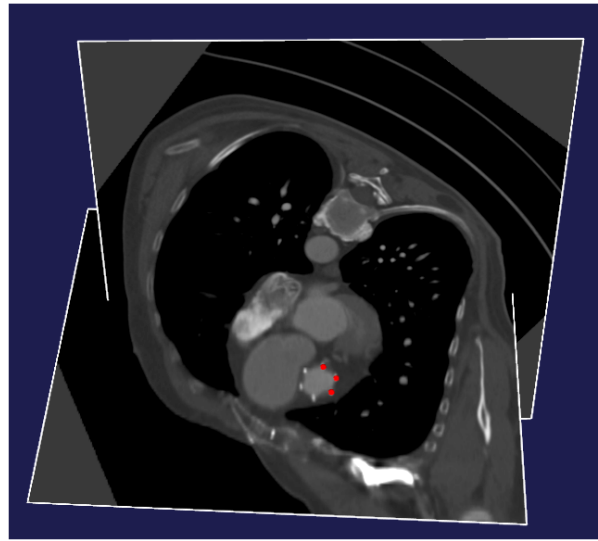


Figure 2.8: Identification of the stent points from Patient 1's CT scans.

The base points were then saved and opened with Paraview together with the artery geometry, as shown in case A) of Figure 2.9, where the geometry of the stent has been recreated for both patients. Finally, on the right of the same figure, in case B), there is the result of the geometrical cut at the level of the stent, at the top for Patient 1 and at the bottom for Patient 2.

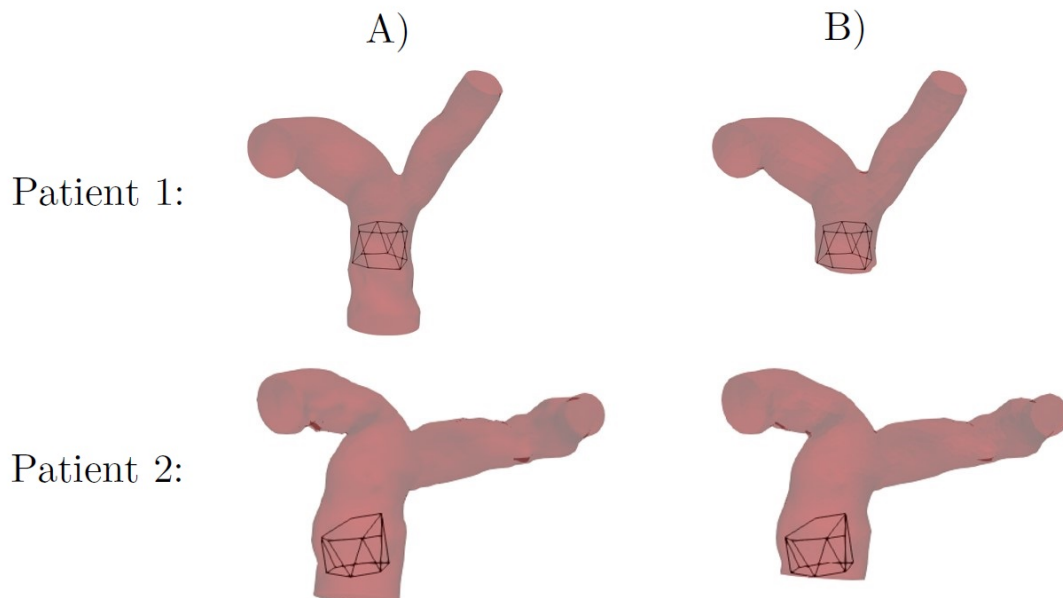


Figure 2.9: A) The arteries of Patient 1 (top) and Patient 2 (bottom) before the cutting operation at the level of the beginning of the valve zone. B) The arteries of the two patients after the cutting operation.

To perform the cutting operation we had to make sure that the inlet was flat in order to correctly apply the boundary conditions during the CFD simulations (see section 3.4.3). We tested two different approaches. The first one employed the VMTK command *vmtkrenderer* which allows to visualize the 3D image and see the exact coordinates of every point. One can identify the coordinates of a point of the stent and use Paraview to create a plane that passes through that point. The next step is to impose the plane's normal in order to cut the artery and obtain a flat inlet. This can be performed with the command *vmtkcenterlines* which constructs a line following the barycenter of the domain surface. Another approach to obtain the same perpendicular cut at the inlet is to use the command *vmtkimageseeder* to select three points of the stent of the prosthetic valve and cut the inlet along the plane they form.

For Patient 1 both ways gave satisfying results. Patient 2, however, was more complex to handle, since, as shown in Figure 2.9, the stent's base was not perpendicular to the artery wall. Therefore, the first approach was adopted for this patient and in particular the most upstream point of the stent was selected for the cut.

We then reclosed the geometries with the already cited *vmtksurfacecapper* and proceeded by renumbering the surfaces in order to correctly identify the inlet, the wall and the two outlets. In particular, we assigned label 1 to the physical boundary, label 2 and 3 respectively to the right and left pulmonary branches and label 4 to the inlet. These labels were necessary in order to apply different boundary conditions at the borders during the simulations.

With this last operation we obtained the final geometries for the simulations in the *Healthy* and *Pre* scenarios of both patients.

2.6.2. Post-operative scenario

Regarding the simulations of the *Post* scenario of the patients, with the prosthetic valve implanted, it was necessary to construct for each patient a geometry with an inflow zone coherent with the valve's geometry and therefore more regular with respect to the natural tract given by the artery wall.

Even though the valve stent has a shape that presents distinct angles, the actual lumen, where the blood flows when the valve leaflets are open, is more rounded. Therefore, we decided to model the prosthetic stent with a cylinder. We made use of the software Paraview to construct a cylinder that was adapted into replicating the valve stent as accurately as possible. The first step was to generate a generic cylinder with open bases that had a number of points on the borders of its bases comparable to the number of points of the inlet's border of the domain. We then proceeded by setting the cylinder's height (20mm)

and diameter (29mm) as the ones of the actual valves implanted in the two patients. The stent points were obtained as before with VMTK and, by using Paraview, the geometry was cut in order to exclude the valve zone completely. This is shown in case A) of Figure 2.10, on the left for Patient 1 and on the right for Patient 2. Case B) of the same Figure shows instead the result of the VMTK command *vmtkicpregristration* that first translates and then iteratively rotates the cylinder in order to adapt it as much as possible to the stent points. In particular, setting for this command the value 0 as number of iterations implies to just translate the cylinder so that its barycenter coincides with the one of the stent. A greater number of iterations, instead, also produces a rotation. We decided to perform 100 iterations in order to properly adapt the cylinder to the stent. Case B) of Figure 2.10 shows the translated and rotated cylinder which is now placed where the valve stent should be.

Finally, in case C) we present the final geometries of the two patients in the *Post* configuration with the stent. These geometries were obtained, starting from the results just described, by applying the command *vmtksurfaceharmonicconnect*, which constructs a continuous surface by deforming the boundary of an input surface (the artery) into the boundary of the reference one (the cylinder), and extends the deformation through a harmonic map [14].

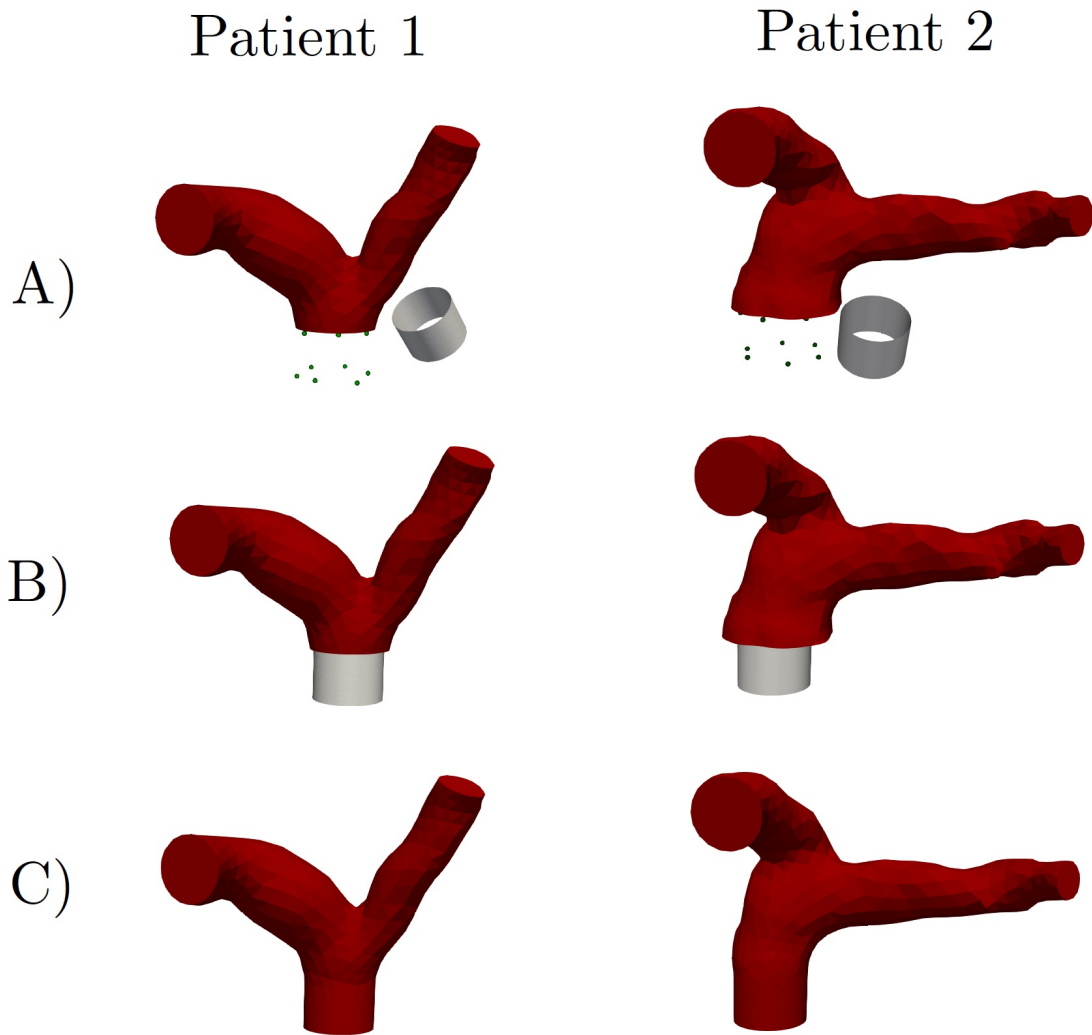


Figure 2.10: Generation of the *Post* meshes for Patient 1 (left) and Patient 2 (right).

A) Cutting of the artery and construction of a stent of the correct size.

B) Positioning of the stent. C) Attachment of the stent to the artery.

2.7. Mesh generation

After the definition and construction of the geometries for the three scenarios, the next step is the creation of the superficial meshes for the lumen of the two (*Healthy/Pre* and *Post*) pulmonary artery configurations of the two patients. In order to better capture the specific zones of interest (the inlet or valve zone and the outlets), we decided to not employ an isotropic mesh but to give the edges of the mesh elements a varying size according to the zone. In particular, we made use of the VMTK command `vmtksurfaceharmonicsolver`, which resolves an equation based on the Laplace-Beltrami operator on a given surface.

We applied this procedure on the mesh surface, imposing the value 0 for the solution Φ at the mesh inlet and the value 1 for Φ at the outlets. The solution of the equation can be seen in Figure 2.11, on the left. We then employed the software Matlab [28] and in particular the command *polyfit* in order to interpolate a third degree polynomial in Φ , which represented the edgelenhth of the mesh and assumed user-defined values in some specific points of the surface. This way it was possible to obtain a curve as the one shown in Figure 2.11, on the right, where the points identified by the X s are the ones to be interpolated. The dark blue cross is the inlet, the light blue one is just before the artery bifurcation, the green one is half way through the surface and the red one is the outlet. According to the level of interest of a zone, we gave it a more ore less fine edgelenhth, so for example, the inlet zone is the finest one.

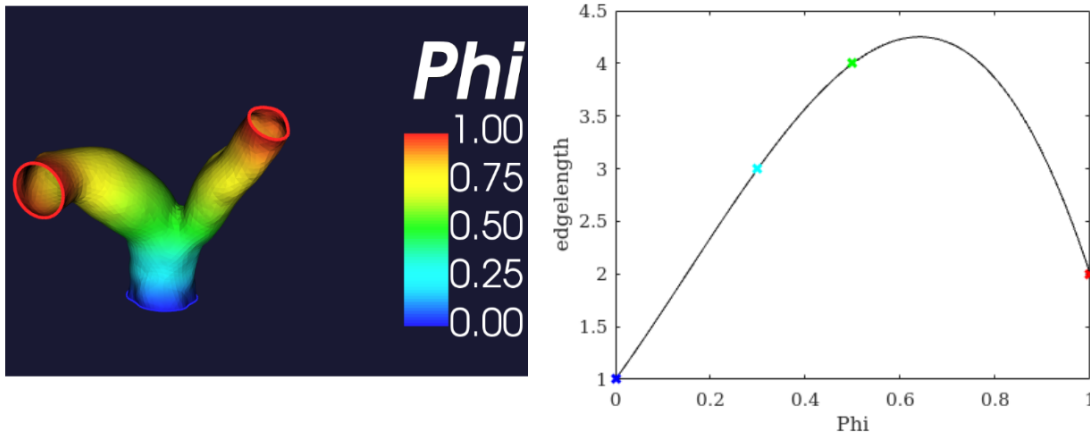


Figure 2.11: On the left the function Φ describing the geometry of Patient 1, on the right the edgelenhth chosen for the meshes with respect to Φ .

We then used the VMTK command *vmtksurfaceremeshing* to obtain a triangular surface mesh with the calculated edgelenhth. The superficial mesh was then transformed into a volumetric one of tetrahedrons through the command *vmtkmeshgenerator* which makes use of an algorithm called *Tetgen* to fill the mesh volume with tetrahedrons. The size of these 3D mesh elements is controlled by a parameter that represents the proportionality constant between the local surface edgelenhth and the element volume. Finally, each tetrahedron was divided into four hexahedrals since the *Life^X* library used for the simulations required hexahedral meshes.

The final meshes obtained for all the scenarios are shown in Figure 2.12. On the left there are, respectively, the mesh for the *Healthy/Pre* scenario on top and the mesh for the *Post* scenario at the bottom, for Patient 1. On the right instead there are the meshes of Patient 2: The *Healthy/Pre* one on top and the *Post* one at the bottom.

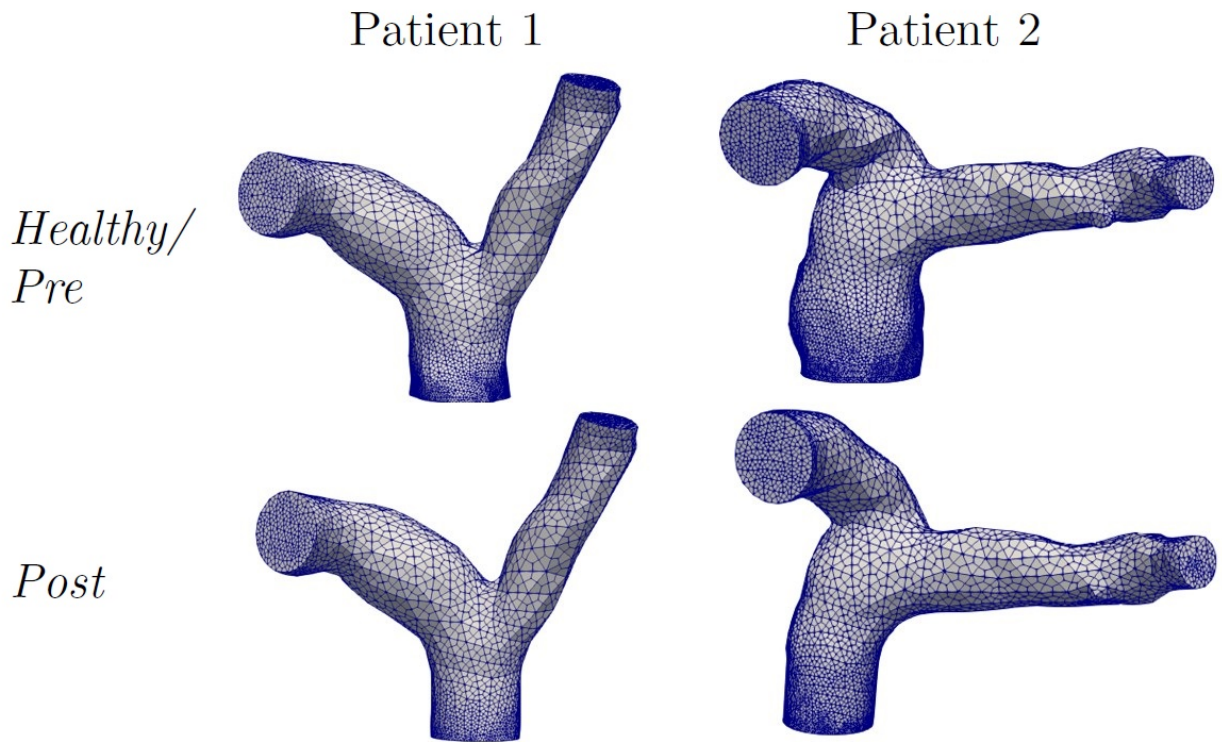


Figure 2.12: Final meshes in the *Healthy/Pre* (top left and right respectively for Patient 1 and 2) and *Post* (bottom left and right respectively for Patient 1 and 2) scenarios.

The main information on the two *Healthy/Pre* meshes is reported in Table 2.1, while the details on the *Post* meshes are shown in Table 2.2.

Healthy/Pre	Patient 1	Patient 2
Number of elements	56,564	113,678
Number of DOFs	227,676	464,676
Maximum cell diameter [m]	0.0074	0.0076
Minimum cell diameter [m]	0.0007	0.0007
Average cell diameter [m]	0.0025	0.0022

Table 2.1: Information on the final hexahedral meshes of the two patients for the *Healthy/Pre* configuration.

Post	Patient 1	Patient 2
Number of elements	46,188	53,960
Number of DOFs	185,092	216,796
Maximum cell diameter [m]	0.0075	0.0076
Minimum cell diameter [m]	0.0007	0.0007
Average cell diameter [m]	0.0025	0.0027

Table 2.2: Information on the final hexahedral meshes of the two patients for the *Post* configuration.

3 | Mathematical and Numerical models

In order to perform the CFD simulations of the blood flowing in the two patients' pulmonary arteries, we adopted a geometric multiscale model composed by two main compartments which had a different level of accuracy. The first compartment was a 3D model of the artery obtained from the 3D reconstructions described in the previous chapter in which we modelled the blood flow with incompressible Navier-Stokes equations. Regarding the second compartment, this consisted in a 0D or lumped model of the rest of the circulation, which was coupled with the 3D model in order to assign physiological conditions at the artificial boundaries of the 3D domain.

In this chapter we describe both the 3D and the 0D models from a mathematical point of view and we present the coupling algorithm adopted for our study. In section 3.5 we present a variant of the 0D part of the model which we implemented in order to analyse the effect of differentiating the outlet boundary conditions of the 3D model on the flow repartition at the main pulmonary bifurcation.

3.1. Blood modeling

A fluid can be modeled as *Newtonian* if it satisfies Newton's law of viscosity: $\tau = \mu \frac{du}{dy}$, where τ is the shear stress, μ is the viscosity and $\frac{du}{dy}$ is the shear rate. Blood plasma, which is composed by 93% of water, can be considered Newtonian, however blood in general cannot. Indeed, plasma constitutes only the 55% of blood, while the rest of it is made up of formed elements such as red and white blood cells and platelets [42]. If the lumen size is comparable to the particles' size, as it happens at the microcirculation level, these formed elements cannot be neglected and blood needs to be considered as a suspension. However, in the case of big arteries such as the pulmonary one, blood can be modelled as a homogeneous and Newtonian fluid [7]. Moreover, blood can be considered incompressible since a change in its pressure causes a variation of the density that is negligible, in comparison [5].

3.2. 3D model: Incompressible Navier-Stokes equations

For the 3D part of our model, we adopted a computational fluid dynamics (CFD) model based on the incompressible Navier-Stokes equations in a fixed domain, which was given by the reconstructed pulmonary arteries of the patients. Indeed, although blood vessels are not rigid and a Fluid Structure Interaction (FSI) model would be more natural to adopt, since we are in the context of a large artery, neglecting the wall compliance, i.e. the property of undergoing elastic deformation, can be an acceptable approximation for the pulmonary artery, where the pressures are lower than the aortic case [11]. In [24] it is noticed that in the pulmonary artery a rigid-wall assumption tends to slightly overestimate some hemodynamic quantities and, in particular, [11] underlines an overestimate regarding the wall-related ones like the wall shear stress. However, the obtained patterns of flow distribution have been proven to be comparable [11] and, since the cost of an FSI simulation would be much higher and the FSI is partly taken into account through the 0D model (more details about this are in section 3.3), we have decided to adopt a rigid-wall hypothesis.

We consider a domain $\Omega \subset \mathbb{R}^3$, as shown in Figure 3.1, which represents the pulmonary artery. The boundary of Ω is composed first of all by Γ_{IN} , which represents the inlet section of the artery where the pulmonary valve is positioned, at the outflow of the right ventricle. The Γ_{OUTj} are instead the two outlet sections: one for the right pulmonary artery (Γ_{OUT1}) and one for the left one (Γ_{OUT2}). Finally, Γ_{WALL} is the artery wall.

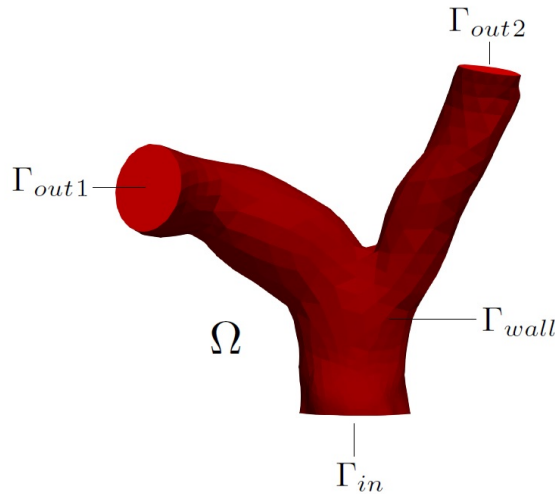


Figure 3.1: 3D domain of the model.

We call $\mathbf{u}(\mathbf{x}, t) : \Omega \times \mathbb{R}^+ \rightarrow \mathbb{R}^3$ the velocity profile of the blood in space and time and $p(\mathbf{x}, t) : \Omega \times \mathbb{R}^+ \rightarrow \mathbb{R}$ the pressure of the blood in space and time. The differential form of the incompressible Navier-Stokes equations in 3D for a Newtonian fluid is the following.

For each $t \in T$ find $\mathbf{u}(\mathbf{x}, t)$ and $p(\mathbf{x}, t)$ such that:

$$\begin{cases} \rho \frac{\partial \mathbf{u}}{\partial t} + \rho(\mathbf{u} \cdot \nabla) \mathbf{u} + \nabla p - \mu \nabla \cdot (\nabla \mathbf{u} + \nabla \mathbf{u}^T) = \mathbf{0} \text{ in } \Omega, \\ \nabla \cdot \mathbf{u} = \mathbf{0} \text{ in } \Omega, \\ \mathbf{u}(\mathbf{x}, t) = \mathbf{0} \text{ on } \Gamma_{WALL}, \\ \mathbf{u}(\mathbf{x}, 0) = \mathbf{0} \text{ in } \Omega. \end{cases} \quad (3.1)$$

The first equation of system (3.1) is the conservation of momentum. The first term of this equation is the variation of the velocity in time, since we are considering a time-dependent problem, and ρ is the constant blood density. The forcing term is 0 since we are in the context of an artery, while μ is the constant flow viscosity. The incompressibility constraint is instead taken into account by imposing the second equation, which is the conservation of mass. The third and fourth equations are, respectively, the initial condition for the velocity and the wall boundary condition of no-slip. The initial condition assumes the beginning of the simulation to be in the diastolic phase, when the pulmonary valve is closed and the velocity of the blood entering the artery is 0. The imposition of this condition will be discussed in more detail in the next chapter (section 4.3.2). The no-slip condition instead assumes a zero velocity close to the artery wall.

To solve the system in (3.1), appropriate boundary conditions have to be assigned also at the artificial boundaries Γ_{IN} and Γ_{OUTj} . We decided to fix a Dirichlet boundary condition at the inlet and a Neumann boundary condition at the outlets for the 3D problem (see section 3.4.4):

$$\begin{aligned} \mathbf{u}(\mathbf{x}, t) &= \mathbf{g} \text{ on } \Gamma_{IN}, \\ T_F(\mathbf{u}, p)\mathbf{n} &= \boldsymbol{\psi} \text{ on } \Gamma_{OUTj}, \end{aligned} \quad (3.2)$$

where $T_F(\mathbf{u}, p)\mathbf{n} = \mu(\nabla \mathbf{u} + \nabla \mathbf{u}^T) - p\mathbf{I}$. These conditions will be provided by the 0D model in the final coupled algorithm, as we will see in section 3.4. In particular, the same function $\boldsymbol{\psi}$ will be assigned at the two outlets.

A more compact form of system (3.1) is:

$$\begin{cases} P_{3D}(\mathbf{u}, p) = \mathbf{0} \text{ in } \Omega, \\ \mathbf{u}(\mathbf{x}, 0) = \mathbf{0} \text{ in } \Omega, \end{cases} \quad (3.3)$$

where P_{3D} represents the Navier-Stokes equations and the no-slip boundary condition on the artery wall.

3.2.1. Time discretization of the problem

The adopted algorithm needs to solve the 3D model many times, imposing each time different boundary conditions according to the outputs of the 0D model. Therefore, the model has to be discretized in time in order to be solved and a time interval T must be defined by the user performing the simulation. The typical choice is a multiple of the heartbeat period, which we have set equal to 0.8s. Another parameter that has to be set is in how many time intervals Δt to subdivide T . If we call N the number of timesteps, we can define $\Delta t = \frac{T}{N}$.

To perform the time discretization we have adopted the *semi-implicit Euler* method. We approximated $\mathbf{u}(t^{n+1}, \mathbf{x})$ with $\mathbf{u}^{n+1}(\mathbf{x})$ and $p(t^{n+1}, \mathbf{x})$ with $p^{n+1}(\mathbf{x})$ and employed a Backward Euler method. The non linear term was linearized by means of a semi-implicit approach where an extrapolation from previous time steps is used:

$$\rho(\mathbf{u}(t^{n+1}) \cdot \nabla) \mathbf{u}(t^{n+1}) \simeq \rho(\mathbf{u}^n \cdot \nabla) \mathbf{u}^{n+1}. \quad (3.4)$$

With this extrapolation, the stability condition for Δt is of type $\Delta t \lesssim h$, where h is the mesh discretization step. This condition on the choice of the timestep is not very restrictive in the hemodynamic setting, indeed a small timestep needs to be adopted in any case because of the pulsatility of the blood flow, in order to capture the rapidity of the systole [42].

The time discretization of the 3D problem in (3.1) takes the following form:

$$\left\{ \begin{array}{l} \rho \frac{\mathbf{u}^{n+1} - \mathbf{u}^n}{\Delta t} + \rho(\mathbf{u}^n \cdot \nabla) \mathbf{u}^{n+1} + \nabla p^{n+1} - \mu \nabla \cdot \left(\nabla \mathbf{u}^{n+1} + (\nabla \mathbf{u}^{n+1})^T \right) \\ = \mathbf{0} \text{ in } \Omega, \\ \nabla \cdot \mathbf{u}^{n+1} = \mathbf{0} \text{ in } \Omega, \\ \mathbf{u}^0 = \mathbf{0} \text{ in } \Omega, \\ \mathbf{u}^{n+1} = \mathbf{0} \text{ on } \Gamma_{WALL}. \end{array} \right. \quad (3.5)$$

3.2.2. Variational formulation of the problem

To solve the 3D system in (3.5) one must introduce three new function spaces. We recall the definition of $L^2(\Omega) = \{\mathbf{u} : \Omega \rightarrow \mathbb{R}^3 \text{ s.t. } \int_{\Omega} \mathbf{u}^2 < \infty\}$ and of the Sobolev space

$$H^1(\Omega) = \{\mathbf{u} : \Omega \rightarrow \mathbb{R}^3 \text{ s.t. } \int_{\Omega} \mathbf{u}^2 < \infty \text{ and } \int_{\Omega} \nabla \mathbf{u}^2 < \infty\}.$$

The first two new spaces are defined as:

$$V_0 = \left\{ \mathbf{v} \in [H^1(\Omega)]^3 \text{ s.t. } \mathbf{v}|_{\Gamma_{IN}} = \mathbf{0} \text{ and } \mathbf{v}|_{\Gamma_{WALL}} = \mathbf{0} \right\},$$

$$V = \left\{ \mathbf{v} \in [H^1(\Omega)]^3 \text{ s.t. } \mathbf{v}|_{\Gamma_{IN}} = \mathbf{g} \text{ and } \mathbf{v}|_{\Gamma_{WALL}} = \mathbf{0} \right\}.$$

V_0 is a space of 3D vectors on the domain that have a zero value both at the inlet and on the artery wall. V is instead characterized by a prescribed velocity at the inlet.

We define the third space as $Q = L^2(\Omega)$ and introduce two variables $\mathbf{v} \in V_0$ and $q \in Q$. The spaces V and V_0 will be the spaces where the velocity is defined while the space Q will be the one of the pressure.

We now proceed by multiplying the first equation of (3.5) by \mathbf{v} and the second one by q and integrating by parts the first equation. Substituting the Neumann boundary condition defined in (3.2), we obtain the following system:

Suppose ψ^{n+1} known. For each $n = 0, 1, \dots, N-1$ find $\mathbf{u}^{n+1} \in (\mathbb{R}^+, V)$ and $p^{n+1} \in (\mathbb{R}^+, Q)$ such that:

$$\left\{ \begin{array}{l} \int_{\Omega} \left[\rho \left(\frac{\mathbf{u}^{n+1} - \mathbf{u}^n}{\Delta t} \right) \cdot \mathbf{v} + \rho ((\mathbf{u}^n \cdot \nabla) \mathbf{u}^{n+1}) \cdot \mathbf{v} - p^{n+1} \nabla \cdot \mathbf{v} \right. \\ \left. + \mu \left(\nabla \mathbf{u}^{n+1} + (\nabla \mathbf{u}^{n+1})^T \right) \nabla \mathbf{v} \right] d\Omega = - \int_{\Gamma_{out,j}} \psi^{n+1} \mathbf{n} \cdot \mathbf{v} d\gamma \quad \forall \mathbf{v} \in V_0, \\ \int_{\Omega} (\nabla \cdot \mathbf{u}^{n+1}) q = 0 \quad \forall q \in Q, \\ \mathbf{u}^0 = \mathbf{0} \text{ in } \Omega. \end{array} \right. \quad (3.6)$$

3.2.3. Backflow stabilization

During the diastolic phase of 3D hemodynamic simulations, it is very typical to see some instabilities at the artificial boundaries and in particular where the Neumann condition are assigned. These instabilities are caused by the artificial cut of the domain and by the fact that the advection term of the Navier-Stokes equations unstabilizes the energy balance when the normal to a boundary (which is outward) and the velocity have opposite signs [6]. An example of this phenomenon can be seen in Figure 3.2, where, on the left, a moment of the systole is represented and the flow is only exiting the domain without generating instabilities. The two images on the right, on the other hand, show how the presence of a backflow during the diastole unstabilizes the solution.

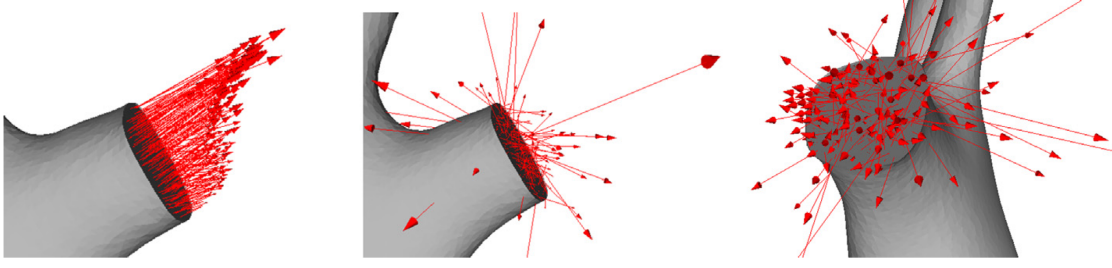


Figure 3.2: Example of backflow instability: the velocity vectors at the time of peak flow (left) and when the backflow begins during the diastole (center and right) [6].

To avoid the instabilities caused by the backflow at the Neumann boundaries it is possible to add a stabilization term of the form:

$$S = \beta \frac{\rho}{2} (\mathbf{u} \cdot \mathbf{n})_- \mathbf{u}, \quad (3.7)$$

where β is a constant and:

$$(\mathbf{u} \cdot \mathbf{n})_- = \begin{cases} -\mathbf{u} \cdot \mathbf{n} & \text{if } \mathbf{u} \cdot \mathbf{n} < 0, \\ 0 & \text{if } \mathbf{u} \cdot \mathbf{n} \geq 0. \end{cases}$$

The Neumann boundary condition in (3.2) is subsequently modified whenever a backflow is present and becomes:

$$T_F(\mathbf{u}, p)\mathbf{n} = \boldsymbol{\psi} + S, \quad (3.8)$$

where S is the term in (3.7). This way, the reversed flow caused by the vortexes close to the outlets is penalized.

The time discretization of the stabilization term is obtained coherently with the one of the convective term described in equation (3.4) [6] and can be written as:

$$(-\beta \frac{\rho}{2} (\mathbf{u}^n \cdot \mathbf{n})_- \mathbf{u}^{n+1}, \mathbf{v})_{\Gamma_{OUT,j}}.$$

3.2.4. Finite Elements method

The next step to solve the 3D problem is to subdivide the domain Ω in hexahedrals K .

$$\Omega \subset \Omega_h = \bigcup_{k \in H_k}^n K.$$

Regarding the spaces V , V_0 and Q , they must be substituted with finite-dimensional spaces. We assume $V^h \subset V$, $V_0^h \subset V_0$ and $Q^h \subset Q$ and define M_h as the dimension of Q_h and N_h

as the dimension of V^h and V_0^h . The total degrees of freedom of the finite element space in which the solution $(\mathbf{u}^{n+1}, p^{n+1})$ lives is $3N_h + M_h$, since the velocity has three components and each of them has dimension N_h , while the pressure is scalar and has dimension M_h . The problem can be rewritten in a simpler notation in this new setting of approximated spaces, where (\cdot, \cdot) denotes the scalar product.

The obtained formulation is called *Galerkin problem* and it takes the following form:

For each $n = 0, 1, \dots, N-1$ find $\mathbf{u}_h^{n+1} \in V_h$ and $p_h^{n+1} \in Q_h$ such that:

$$\left\{ \begin{array}{l} (\rho \frac{\mathbf{u}_h^{n+1} - \mathbf{u}_h^n}{\Delta t}, \mathbf{v}_h) + (\rho(\mathbf{u}_h^n \cdot \nabla)\mathbf{u}_h^{n+1}, \mathbf{v}_h) + \mu(\nabla\mathbf{u}_h^{n+1} + (\nabla\mathbf{u}_h^{n+1})^T, \nabla\mathbf{v}_h) \\ - (p_h^{n+1}, \nabla \cdot \mathbf{v}_h) = -(\psi^{n+1}\mathbf{n}, \mathbf{v}_h)_{\Gamma_{OUT,j}} - (\beta \frac{\rho}{2}(\mathbf{u}_h^n \cdot \mathbf{n})_-\mathbf{u}_h^{n+1}, \mathbf{v}_h)_{\Gamma_{OUT,j}} \quad \forall \mathbf{v}_h \in V_0^h, \\ (\nabla \cdot \mathbf{u}_h^{n+1}, q_h) = 0 \quad \forall q_h \in Q^h, \\ \mathbf{u}_h^0 = \mathbf{0} \text{ in } \Omega_h, \\ \mathbf{u}_h^{n+1} = \mathbf{0} \text{ on } \Gamma_{WALL}, \\ \mathbf{u}_h^{n+1} = \mathbf{g}^{n+1} \text{ on } \Gamma_{IN}. \end{array} \right. \quad (3.9)$$

We introduce the basis functions of the space V^h using vectorial lagrangian basis functions for the velocity $\{\phi_j, j = 1, 2, \dots, 3N_h\}$ and we write the velocity unknown as linear combinations of the basis functions:

$$u_h^n(\mathbf{x}) = \sum_{j=1}^{3N_h} u_j^n \phi_j(\mathbf{x}),$$

where:

$$\phi_j(\mathbf{x}_i) = \delta_{ij} = \begin{cases} 0 & \text{if } i \neq j, \\ 1 & \text{if } i = j, \end{cases} \quad i, j = 1, \dots, 3N_h,$$

are the lagrangian basis functions. The terms u_j^n are instead the values of the flow velocity on the vertices of the mesh.

Regarding the space Q^h , we proceeded in the same way defining the basis functions for the pressure space as $\{\psi_j, j = 1, 2, \dots, M_h\}$ and setting as $p_h^n(\mathbf{x}) = \sum_{j=1}^{M_h} p_j^n \psi_j(\mathbf{x})$.

The finite elements chosen to solve this problem were $\mathbb{P}_1 - \mathbb{P}_1$ elements, therefore we can introduce the \mathbb{P}_1 finite element space of piece-wise linear polynomial functions:

$$X_1^h = \{\mathbf{v}_h^{n+1} \in C^0(\Omega) \text{ s.t. } \mathbf{v}_h^{n+1}|_K \in P_1, \forall K \in \mathcal{K}\}.$$

We can define the discretized spaces as $V^h = V \cap [X_1^h]^3$, $V^h = V \cap [X_1^h]^3$ and $Q^h = Q \cap X_1^h$.

An important issue regarding the chosen spaces is the uniqueness and stability of the solution. Indeed, $\mathbb{P}_1 - \mathbb{P}_1$ elements do not satisfy Brezzi's theorem and in particular the inf-sup stability condition:

$$\forall q_h \in Q^h, \mathbf{v}_h \in V^h \text{ s.t. } (\nabla \cdot \mathbf{v}_h, q_h) \geq \alpha \|\mathbf{v}_h\|_{H^1(\Omega)} \|q_h\|_{L^2(\Omega)}.$$

Brezzi's theorem guarantees uniqueness and existence of the solution of the Galerkin problem in (3.9) [39]. However, although the other hypothesis of the theorem (continuity and coercivity), are satisfied, the inf-sup condition requires the velocity space to be richer than the pressure one, which doesn't happen in this case since the two spaces are the same. On the other hand, this choice of spaces is more convenient than for example $\mathbb{P}_2 - \mathbb{P}_1$ spaces, since the latter, even if stable, are much more of an expensive choice computationally. Another issue of the 3D problem regards the instabilities that can be generated by the presence of a high Reynolds number. The *Reynolds* number is an adimensional quantity defined as $Re = \frac{|\mathbf{U}|L}{\nu}$, where L is a representative of the length of the domain, \mathbf{U} is a representative of the fluid velocity and ν is the viscosity. This number measures how much the convection term dominates over the diffusive term [39]. If the Reynolds number is high, there may be problems regarding for example the stability of the solutions and the transition to a turbulent regime [39].

In this model both the cited instabilities (inf-sup and Reynolds) were resolved by means of the Streamline Upwind Petrov Galerkin - Pressure Stabilizing Petrov Galerkin (SUPG-PSPG) stabilization method. This method adds some terms to the system (3.9) and, in particular, a stiffness matrix for the pressure that adds some artificial compressibility, making Brezzi's inf-sup condition true, and some penalization terms that stabilize the high Reynolds. The added terms go to 0 with h , since the method is strongly consistent [39].

3.2.5. Algebraic 3D problem

To solve the problem in (3.9) we can now redefine it as an algebraic linear system of the form $\mathbf{Ax} = \mathbf{b}$ by rewriting every term of the system in an algebraic form.

First of all we introduce $\mathbf{U}^{n+1} = [U^{n+1}]_j$ with $j = 1, 2, \dots, 3N_h$ and $\mathbf{P}^{n+1} = [P^{n+1}]_i$ with $i = 1, 2, \dots, M_h$. The vector \mathbf{x} can be seen as $[\mathbf{U}^{n+1}, \mathbf{P}^{n+1}]^T$.

We then define some matrices and vectors in order to rewrite each term of the problem in algebraic form:

- $(\rho \frac{\mathbf{u}_h^{n+1}}{\Delta t}, \mathbf{v}_h) \rightarrow M\mathbf{U}^{n+1}$, where $M \in \mathbb{R}^{3N_h \times 3N_h}$ and $M_{lj} = \frac{\rho}{\Delta t} (\phi_j, \phi_l)$,

- $(p_h^{n+1}, \nabla \cdot \mathbf{v}_h) \rightarrow B^T \mathbf{P}^{n+1}$, where $B^T \in \mathbb{R}^{3N_h \times M_h}$ and $B_{li}^T = (\psi_i, \nabla \cdot \phi_l)$,
- $(\nabla \cdot \mathbf{u}_h^{n+1}, q_h) \rightarrow B \mathbf{U}^{n+1}$, where $B \in \mathbb{R}^{M_h \times 3N_h}$ and $B_{mj} = (\nabla \cdot \phi_j, \psi_m)$,
- $(\mu(\nabla \mathbf{u}_h^{n+1} + (\nabla \mathbf{u}_h^{n+1})^T), \nabla \mathbf{v}_h) \rightarrow D \mathbf{U}^{n+1}$, where $D \in \mathbb{R}^{3N_h \times 3N_h}$ and $D_{lj} = (\mu(\nabla \phi_j + \nabla \phi_j^T), \phi_l)$,
- $(\rho(\mathbf{u}_h^n \cdot \nabla) \mathbf{u}_h^{n+1}, \mathbf{v}_h) \rightarrow N(\mathbf{U}^n) \mathbf{U}^{n+1}$, where $N(\mathbf{U}^n) \in \mathbb{R}^{3N_h \times 3N_h}$ and $N(\mathbf{U}^n)_{lj} = (\rho(\mathbf{U}^n \cdot \nabla) \phi_j, \phi_l)$,
- $-(P_{OUT}^n \mathbf{n}, \mathbf{v}_h)_{\Gamma_{OUT,j}} \rightarrow H$,
- $-\beta(\frac{\rho}{2}(\mathbf{u}_h^n \cdot \mathbf{n})_{-} \mathbf{u}_h^{n+1}, \mathbf{v}_h)_{\Gamma_{N,i}} \rightarrow E_i(\mathbf{U}^n) \cdot \mathbf{U}$, where $E(\mathbf{U}^n) \in \mathbb{R}^{3N_h \times 3N_h}$ and $E_i(\mathbf{U}^n)_{lj} = -\beta(\frac{\rho}{2}(\mathbf{u}_h^n \cdot \mathbf{n})_{-} \phi_j, \phi_l)_{\Gamma_{N,i}}$.

If we call $F(\mathbf{U}^n) = H + M(\mathbf{U}^n)$ and define $K(\mathbf{U}^n) = D + M + N(\mathbf{U}^n) + E(\mathbf{U}^n)$, the following system is obtained:

$$\begin{bmatrix} K(\mathbf{U}^n) & B^T \\ B & 0 \end{bmatrix} \begin{bmatrix} \mathbf{U}^{n+1} \\ \mathbf{P}^{n+1} \end{bmatrix} = \begin{bmatrix} F(\mathbf{U}^n) \\ 0 \end{bmatrix}. \quad (3.10)$$

This system was solved using the Generalized Minimal RESidual (GMRES) method, which is an iterative Krylov method for nonsymmetric systems of linear equations [39]. As preconditioner, a Semi-Implicit Method for Pressure Linked Equations (SIMPLE) preconditioner was adopted. This preconditioner is obtained as a variant of the LU factorization that makes use of triangular matrices [39].

3.3. 0D model

Concerning the 0D part of the model, it consisted in an electrical analogy of the cardiovascular system. In particular, in this model we considered the blood flow rate as a current and its pressure as a voltage. Circuit elements such as capacitors, resistors, inductors and diodes were also adopted to simulate the different behaviours of the circulatory system. The capacitances model the wall compliance which can be seen as the interaction between the blood flow and the walls. The resistances correspond to the blood viscosity effect and the inductances represent instead the inertial effects of the blood flow [45]. Diodes are positioned in place of the four heart valves since a diode is an electrical component which allows the current to flow in only one direction. In particular, a diode lets the current pass through the circuit when the downstream voltage is higher than the upstream one,

it instead opposes a strong resistance when the current sign inverts itself [36]. This mechanism is comparable to the one of the heart valves described in the first chapter. The valves, in fact, only let the blood flow in one direction by closing when a backflow starts to form.

3.3.1. Model derivation: Step 1

In order to take into account of the compliance of the heart and vessel walls, the 0D model equations must be derived not from a rigid-wall model but from an FSI model of the blood flow. Therefore, in this context we have to consider three different subproblems: a Navier-Stokes problem for the blood, this time however in the context of a moving domain, a finite elasticity problem, describing the movement of the boundary walls, and finally some physical interface conditions in addition to the artificial boundary ones already seen. The adopted model employs a lagrangian-eulerian (ALE) approach, where the structure is considered in a lagrangian framework while the fluid in an eulerian one. We consider a domain $\Omega_F^t \subset \mathbb{R}^3$ which is the now time-dependent pulmonary artery lumen; $\hat{\Omega}_S \subset \mathbb{R}^3$ is instead the reference configuration of the artery wall. We define $\mathbf{d} : \hat{\Omega}_S \times \mathbb{R}^+ \rightarrow \mathbb{R}^3$ as the displacement of the structure and \mathbf{d}_F as the fictitious displacement of the fluid domain.

The 3D FSI problem takes the following form:

For each $t \in T$ find $\mathbf{u}(\mathbf{x}, t) : (\Omega_F \times \mathbb{R}^+) \rightarrow \mathbb{R}^3$, $p(\mathbf{x}, t) : (\Omega_F \times \mathbb{R}^+) \rightarrow \mathbb{R}$, \mathbf{d}_F and \mathbf{d} such that:

$$\left\{ \begin{array}{l} -\Delta \hat{\mathbf{d}}_F = \mathbf{0} \text{ in } \hat{\Omega}_F, \\ \hat{\mathbf{d}}_F = \hat{\mathbf{d}} \text{ in } \hat{\Sigma}, \\ \rho_F \frac{\delta \mathbf{u}}{\delta t} + \rho_F (\mathbf{u} - \mathbf{u}_F) \nabla \mathbf{u} - \nabla \cdot T_F(\mathbf{u}, p) = \mathbf{0} \text{ in } \Omega_F^t, \\ \nabla \cdot \mathbf{u} = \mathbf{0} \text{ in } \Omega_F^t, \\ \mathbf{u} = \frac{\partial \mathbf{d}}{\partial t} \text{ on } \Sigma^t, \\ T_F(\mathbf{u}, p) \mathbf{n} = T_S(\mathbf{d}) \mathbf{n} \text{ on } \Sigma^t, \\ \frac{\partial^2 \hat{\mathbf{d}}}{\partial t^2} - \nabla \cdot \hat{T}_s(\hat{\mathbf{d}}) = \mathbf{0} \text{ in } \hat{\Omega}_S. \end{array} \right. \quad (3.11)$$

The first two equations of this system are the harmonic extension equations, which represent the movement of the fluid domain in time with the constraint that on the interface with the structure the displacement is the same as the one of the structure. The second

couple of equations are the Navier-Stokes equations in a moving domain. In particular the derivative in time is considered not in an eulerian framework but in a lagrangian one where the observer moves with the domain and the tensor $T_F(\mathbf{u}, p)$ is the fluid Cauchy stress tensor, defined as: $T_F(\mathbf{u}, p) = -p\mathbf{I} + \mu_f(\nabla\mathbf{u} + (\nabla\mathbf{u})^T)$, for a Newtonian fluid. The fifth equation is the kinematic condition which imposes a no-slip condition at the interface, i.e. the continuity of the velocities. The sixth equation is instead a dynamic condition that represents Newton's third law, i.e. the continuity of the tractions. Finally the last equation is the structure's elasto-dynamic equation. In particular $\hat{T}_s(\hat{\mathbf{d}})$ is the first Piola-Kirchoff tensor and $T_s(\mathbf{d})$ is the structure Cauchy stress tensor. These two are related according to the formula $\hat{T}_s = JT_sF^{-T}$ where $F = \nabla\mathbf{x}$ is the deformation tensor and $J = \det(F)$ represents the variation of the volume of the current configuration Ω_s with respect to the initial configuration $\hat{\Omega}_s$.

3.3.2. Model derivation: Step 2

The next step is to reduce the dimension of the FSI model by defining a 1D model. The idea behind the 1D model is in fact to consider, from the spatial point of view, only one direction of movement of the blood: the axial coordinate, which is direction z if we refer to Figure 3.3. As the figure shows, the domain in which the blood flows can be approximated by a cylinder of section $S(t, z)$.

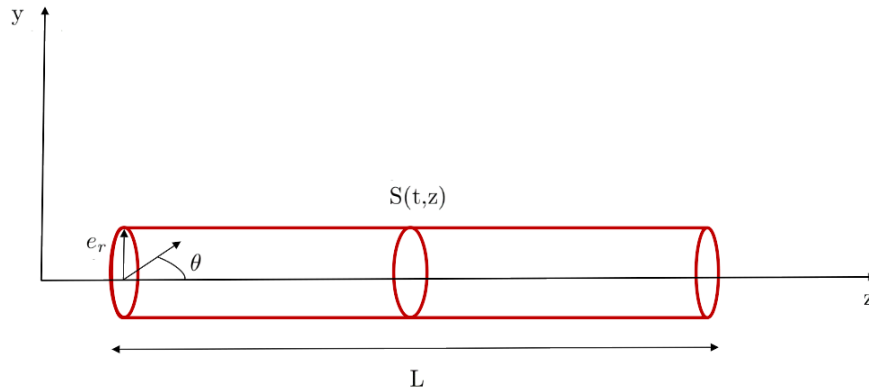


Figure 3.3: Representation of the artery in 1D.

In order to derive this model we have to assume some hypotheses:

- An axi-symmetrical flux with respect to z ;
- A circular section of the vessel;
- A 1D boundary wall;

- A movement of the boundary wall that only occurs in the radial direction (e_r);
- A fixed z axis;
- A constant pressure on each section;
- A flow velocity only in direction z .

New quantities, which will become the new unknowns, must then be introduced. In particular, the area, the flow rate and the mean pressure.

These quantities take the following form:

- $A(t, z) = \int_{S(t,z)} dS;$
- $Q(t, z) = \int_{S(t,z)} u_z(t, z) = A(t, z)\bar{u}(t, z)dS;$
- $p(t, z) = \frac{1}{A(t, z)} \int_{S(t,z)} pdS.$

From the system in (3.11) we obtain the following new set of equations, which take the name of *1D model*:

$$\begin{cases} \frac{\partial Q}{\partial t} + \frac{\alpha \partial}{\partial z} \left(\frac{Q^2}{A} \right) + \frac{A \partial p}{\rho_F \partial z} + k_r \frac{Q}{A} = 0 \quad \forall z \text{ in } (0, L), \quad \forall t < T, \\ \frac{\partial A}{\partial t} + \frac{\partial Q}{\partial z} = 0 \quad \forall z \text{ in } (0, L), \quad \forall t < T, \end{cases} \quad (3.12)$$

where the first equation is derived from the fluid momentum equation in z -direction in a compliant domain. The second equation comes instead from the mass conservation equation in (3.11).

This system isn't however closed and another equation must be added in order to solve three equations in three unknowns. Usually a *Vessel law* is assigned, which is an equation of the form:

$$p(t, z) - p_{ext} = \Phi(A(t, z), A_0(z), \boldsymbol{\beta}(z)),$$

where the term on the left is the pressure jump with the outside of the vessel of interest, $A(t, z)$ is the area of the section, $A_0(z)$ is its initial area and $\boldsymbol{\beta}(z)$ is a parameter that depends on the wall's elastic and geometric properties.

3.3.3. Model derivation: Step 3

The 0D model implies, as its name suggests, a further reduction in dimension with respect to the 1D model. In particular it consists in an integration in the domain $[0 - L]$ of the cylinder of Figure 3.3. This way the spatial information is lost and the resulting system is of ordinary differential equations (ODEs).

To derive the 0D model three further hypothesis are needed:

- The convective or non linear term is negligible,
- The area of the section is constant: $A = A_0$,
- The vessel law is algebraic.

We then introduce two new variables:

- $\tilde{Q}(t) = \frac{1}{L} \int_0^L Q(z, t)$, which is the *flow rate*,
- $\tilde{p}(t) = \frac{1}{L} \int_0^L p(z, t)$, which is the *mean pressure*.

Integrating between 0 and L the 1D system in (3.12) we get:

$$\begin{cases} K_1 L \frac{\partial \tilde{P}}{\partial t} + Q_2 - Q_1 = 0, \\ L \frac{\partial \tilde{Q}}{\partial t} + \frac{A_0}{\rho_F} (p_2 - p_1) + \frac{k_r}{A_0} \tilde{Q} = 0. \end{cases} \quad (3.13)$$

Finally three new quantities must be introduced:

$$R = \frac{8\mu L}{\pi R_0^4}, \quad I = \frac{\rho_F L}{\pi R_0^2}, \quad C = \frac{3\pi R_0^3 L}{H_s E}. \quad (3.14)$$

These quantities are respectively the resistance, the inertial parameter and the mass storage parameter. The first one takes into account the resistive or viscous effects, the second one considers the mass and the third one represents the compliance effect. Substituting these terms in (3.13) gives rise to the following system:

$$\begin{cases} C \frac{d\tilde{P}}{dt} + Q_2 - Q_1 = 0, \\ I \frac{d\tilde{Q}}{dt} + R\tilde{Q} + P_2 - P_1 = 0. \end{cases} \quad (3.15)$$

This system is the system of 0D equations and it has six unknowns: $Q_1, Q_2, P_1, P_2, \tilde{Q}$ and \tilde{P} . To be able to solve it two variables among P_1, P_2, Q_1 and Q_2 have to be assigned by

the boundary conditions. The other two are "confused" with \tilde{P} and \tilde{Q} . This way a 2 by 2 system of equations is obtained.

First of all an electrical analogy can be introduced. The variable R can be considered as an electrical resistance which follows the equation $P = RQ$ that recalls the relation $\Delta V = RI_{current}$. The variable I instead can be considered as an inductance which follows the relation $P = I\dot{Q}$ that is similar to $\Delta V = I\dot{I}_{current}$. Finally C can be considered as a capacity that follows the rule $Q = C\dot{P}$, which is comparable to $I_{current} = C\Delta\dot{V}$. This way, if we consider the voltage ΔV as a pressure P and the current $I_{current}$ as a flow rate Q , we can refer to the system (3.15) as the one needed to solve an RLC circuit.

Depending on what variables among P_1, P_2, Q_1 and Q_2 are assumed as BCs, there are four possible 0D models, which are shown in Figure 3.4. In particular the configuration at the top left is called L network, the one below it is the L-inverted network. The top right one is the π network and the one below it the T network.

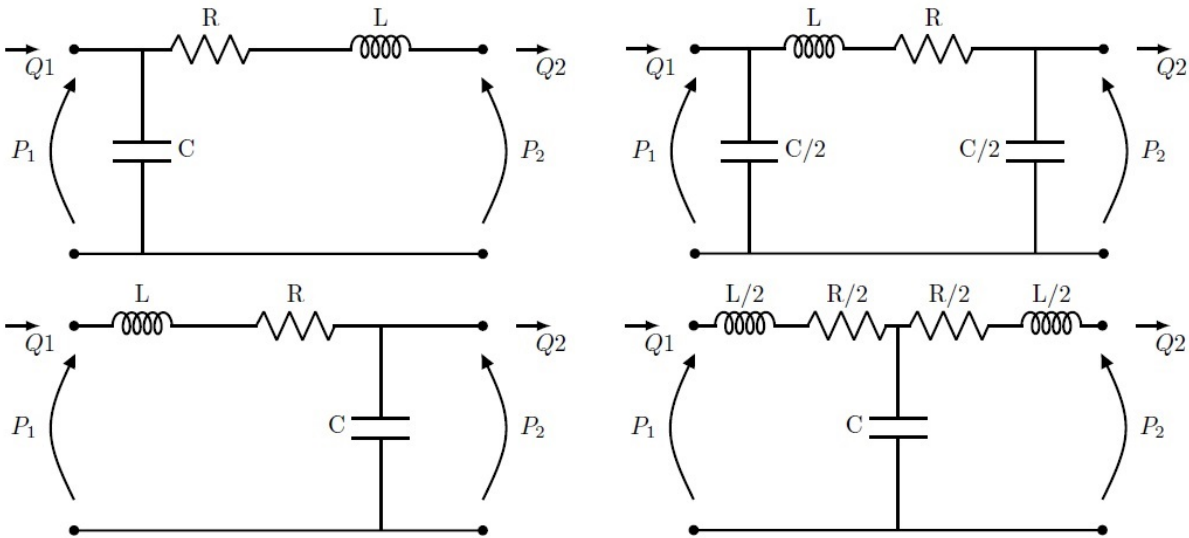


Figure 3.4: Top left: L network. Bottom left: L-inverted network. Top right: π network. Bottom right: T network.

Considering for example the L network we can see the first equation of (3.15) as the balancing of the currents at the node where Q_1 enters. The second equation can instead be seen as the voltage balance for the loop.

The choice of the unknowns in (3.15) is not free. In fact if a network has a capacity on a side it means that the pressure on that side must be known for that circuit, so an appropriate boundary condition must supply it. When coupling an L network with a 3D model, as we will see, this condition will be supplied by the 3D model. On the other hand the 3D model will consequently need a flow condition assigned at the interface, which

is a Dirichlet condition. This way the 3D model is solved using the Dirichlet boundary condition given by the 0D model whereas the 0D model is solved thanks to the pressure boundary condition give by the 3D model. So the L network is compatible with a 3D model which has a Neumann condition at the inlet and a Dirichlet condition on the outlet. The L-inverted network is compatible with the opposite configuration, while the π and the T models are respectively compatible with Dirichlet-Dirichlet and Neumann-Neumann conditions.

Since for our simulations we wanted to impose on the 3D domain a Dirichlet condition at inlet and a Neumann one at the outlets (see section 3.4.4), we made use of two of these configurations together: an L network at the inlet and an L-inverted network at the outlets. However, to describe more accurately the circulatory system, the adopted 0D model does not just consist of RLC circuits but it is composed by many 0D compartments representing the different parts of the circulation.

3.3.4. Model definition

A view of the 0D model adopted in this work (without 3D pulmonary artery) can be seen in Figure 3.5. In particular the top part of the circuit represents the pulmonary circulation, the central part is the cardiac circulation and the bottom part is the systemic circulation. The pulmonary and systemic circulations are represented through RLC circuits while the heart chambers as couplings of capacitors and diodes.

All these compartments follow precise rules. The four heart valves are, as said, modelled as diodes and in particular as non ideal ones. The resistance of the valves is also time-dependent and in particular it is very low when the valves are open ($R_{min} = 0.0075 \frac{mmHg \cdot s}{ml}$) and very high when they are closed ($R_{max} = 75006.2 \frac{mmHg \cdot s}{ml}$).

The valve resistance varies between these two values according to the following equation:

$R = 10^c$, where

$$c = \log_{10} R_{min} + (\log_{10} R_{max} - \log_{10} R_{min}) \cdot \left[\frac{1}{2} + \frac{1}{\pi} \arctan \left(\frac{k\pi}{2} (P2 - P1) \right) \right].$$

The trend of the valves' resistances can be seen in Figure 3.6, on the left, where it is clear how it assumes very high values as soon as the pressure gradient's sign becomes positive.

The four heart chambers are instead modeled by a system of differential-algebraic equations where the compliance, and so the elastance E , which is its reciprocal, is time-

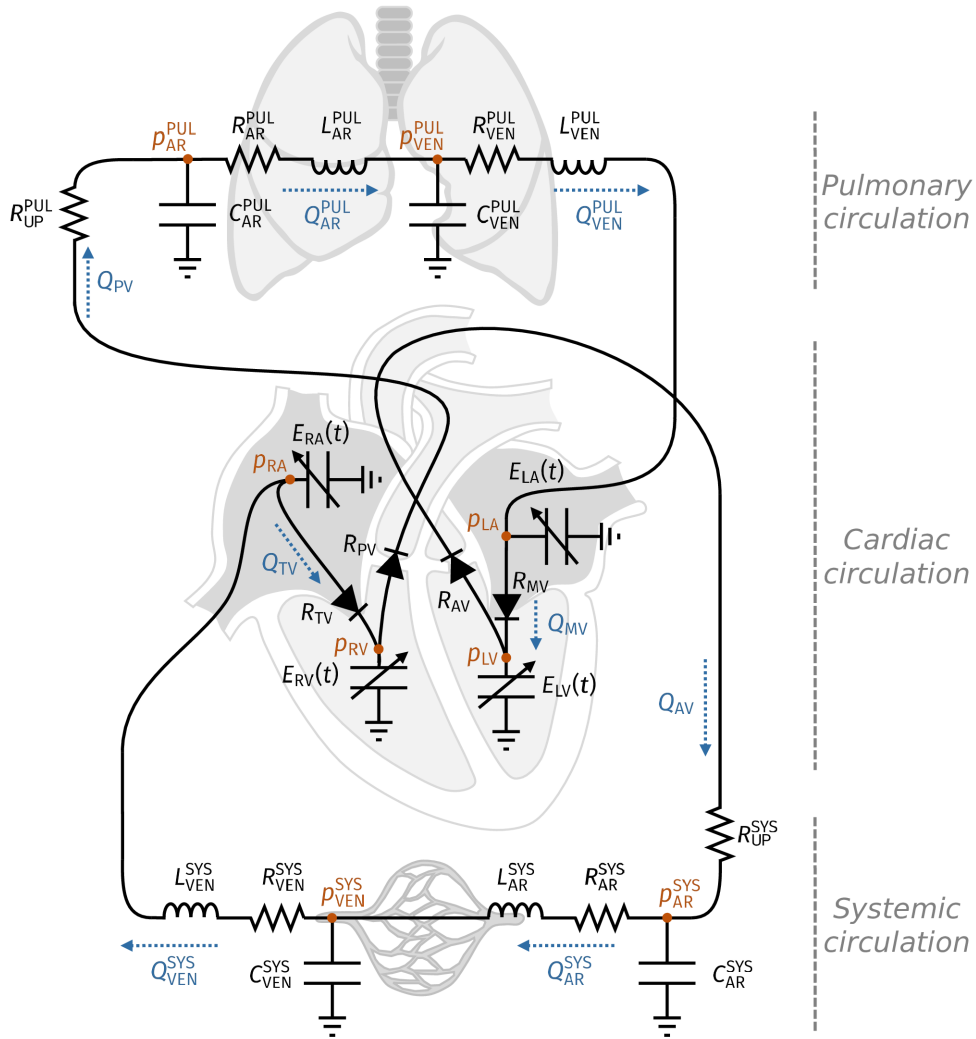


Figure 3.5: 0D circulation model [23]

dependent:

$$\begin{cases} \frac{dV(t)}{dt} + Q_1 - Q_2 = 0, \\ P(t) = p_{ext} + E(t)(V(t) - V_0). \end{cases} \quad (3.16)$$

In this system, V is the volume of the chamber, P is its pressure, Q_1 and Q_2 are respectively the entering and exiting flow.

The time-varying elastance for the heart chambers follows the rule: $E = E_a * y(t) + E_b$, where $y(t)$ is an adimensional term that takes the following form:

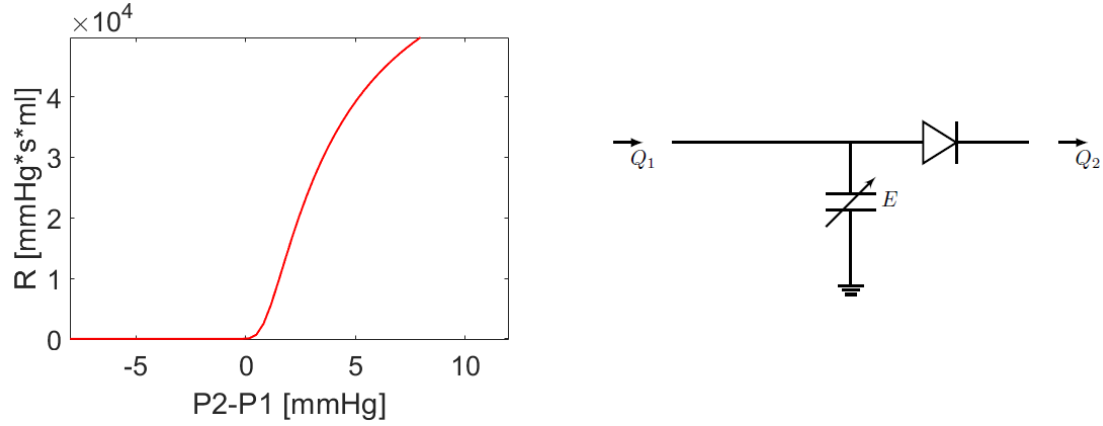


Figure 3.6: Left: Graph of the time-dependent resistance of the 0D heart valves. Right: Heart chamber coupled with its valve (diode).

$$y(t) = \begin{cases} \frac{1}{2} \left(1 - \cos \frac{\pi t}{\Delta t_{contr}}\right), & \text{if } t \leq \Delta t_{contr}, \\ \frac{1}{2} \left(1 + \cos \frac{\pi t}{\Delta t_{contr}}\right), & \text{if } t > \Delta t_{contr}. \end{cases}$$

The heart chambers are coupled in the model directly with the cardiac valves (diodes), as shown in Figure 3.6 on the right.

We now report all the equations of the compartments of the adopted 0D model [45].

The **pulmonary veins** are associated to an RLC circuit:

$$C_{VEN}^{PUL} \frac{dP_{VEN}^{PUL}}{dt} = Q_{AR}^{PUL} - Q_{VEN}^{PUL},$$

$$L_{VEN}^{PUL} \frac{dQ_{VEN}^{PUL}}{dt} = -R_{VEN}^{PUL} Q_{VEN}^{PUL} - (P_{LA} - P_{VEN}^{PUL}).$$

The **left heart** is described by the equations of the two chambers (which are the first two for the atrium and the fourth and fifth for the ventricle, respectively, of the following

list) and the ones of the two valves (third and last equations).

$$\begin{aligned}
 P_{LA} &= P_{ext} + E_{LA}(V_{LA} - V_{LA,0}), \\
 \frac{dV_{LA}}{dt} &= Q_{VEN}^{PUL} - Q_{MV}, \\
 Q_{MV} &= \frac{P_{LA} - P_{LV}}{R_{MV}(P_{LA}, P_{LV})}, \\
 P_{LV} &= P_{ext} + E_{LV}(V_{LV} - V_{LV,0}), \\
 \frac{dV_{LV}}{dt} &= Q_{MV} - Q_{AV}, \\
 Q_{AV} &= \frac{P_{LV} - P_{AR}^{SYS}}{R_{AV}(P_{LV}, P_{AR}^{SYS})}.
 \end{aligned}$$

The **systemic arterial circulation** is modelled as an RLC circuit.

$$\begin{aligned}
 C_{AR}^{SYS} \frac{dP_{AR}^{SYS}}{dt} &= Q_{AV} - Q_{AR}^{SYS}, \\
 L_{AR}^{SYS} \frac{dQ_{AR}^{SYS}}{dt} &= -R_{VEN}^{SYS} Q_{AR}^{SYS} - (P_{VEN}^{SYS} - P_{AR}^{SYS}),
 \end{aligned}$$

The **systemic venous circulation** is modelled as an RLC circuit.

$$\begin{aligned}
 C_{VEN}^{SYS} \frac{dP_{VEN}^{SYS}}{dt} &= Q_{AR}^{SYS} - Q_{VEN}^{SYS}, \\
 L_{VEN}^{SYS} \frac{dQ_{VEN}^{SYS}}{dt} &= -R_{VEN}^{SYS} Q_{VEN}^{SYS} - (P_{RA} - P_{VEN}^{SYS}).
 \end{aligned}$$

The **right heart** is modelled specularly to the left one.

$$\begin{aligned}
P_{RA} &= P_{ext} + E_{RA}(V_{RA} - V_{RA,0}), \\
\frac{dV_{RA}}{dt} &= Q_{VEN}^{SYS} - Q_{TV}, \\
Q_{TV} &= \frac{P_{RA} - P_{RV}}{R_{TV}(P_{RA}, P_{RV})}, \\
P_{RV} &= P_{ext} + E_{RV}(V_{RV} - V_{RV,0}), \\
\frac{dV_{RV}}{dt} &= Q_{TV} - Q_{PV}, \\
Q_{PV} &= \frac{P_{RV} - P_{TRK}}{R_{PV}(P_{TRK}, P_{IN})}.
\end{aligned}$$

The **inlet zone** is modelled as an RLC circuit.

$$\begin{aligned}
C_{IN} \frac{dP_{TRK}}{dt} &= Q_{PV} - Q_{IN}, \\
L_{IN} \frac{dQ_{IN}}{dt} &= -R_{IN}Q_{IN} - (P_{IN} - P_{TRK}).
\end{aligned}$$

The **outlet zone** is modelled as an RLC circuit.

$$\begin{aligned}
C_{OUT} \frac{dP_{OUT}}{dt} &= Q_{OUT} - Q_{AR}^{PUL}, \\
L_{OUT} \frac{dQ_{AR}^{PUL}}{dt} &= -R_{OUT}Q_{AR}^{PUL} - (P_{VEN}^{PUL} - P_{OUT}).
\end{aligned} \tag{3.17}$$

In all these equations the Q s refer to flow rates, the P s to pressures and the V s to chamber volumes. The apices and pedices instead refer to the considered compartment among:

- left and right atrium (LA and RA),
- left and right ventricle (LV and RV),
- mitral, aortic, pulmonary and tricuspid valve (MV, AV, TV and PV),
- pulmonary and arterial venous system (PUL-SYS and VEN-SYS).

Q_{IN} and P_{OUT} are the quantities that will be prescribed at the interface with the 3D model in the final coupled algorithm (see section 3.4.4). Finally P_{TRK} is the pulmonary trunk pressure.

All the listed equations can be rewritten in a more compact form as:

$$\begin{cases} \frac{d}{dt}\mathbf{y} = f_1(t, \mathbf{y}, \mathbf{z}, P_{IN}, Q_{OUT}), \\ \mathbf{y}(0) = \mathbf{y}_0, \\ \mathbf{z} = f_2(t, \mathbf{y}), \end{cases} \quad (3.18)$$

where:

$$\mathbf{y} = [Q_{IN}, P_{OUT}, V_{LA}, V_{RA}, V_{LV}, V_{RV}, P_{VEN}^{PUL}, P_{AR}^{PUL}, P_{VEN}^{SYS}, P_{AR}^{SYS}, Q_{VEN}^{PUL}, Q_{AR}^{PUL}, Q_{VEN}^{SYS}, Q_{AR}^{SYS}]$$

and

$$\mathbf{z} = [Q_{MV}, Q_{AV}, Q_{TV}, Q_{PV}, P_{LV}, P_{RV}, P_{LA}, P_{RA}].$$

We have highlighted the quantities P_{IN} and Q_{OUT} which are forcing terms of the 0D model in our context.

3.3.5. Time discretization of the 0D model

The 0D model, as the 3D one, has to be discretized in time in order to be solved iteratively in the final coupled algorithm. We adopt the *fourth order explicit Runge-Kutta* scheme: a one-step method that requires many evaluations of the right-hand side term at each timestep. More details about this method can be found in [43].

The resulting formulation is the following:

$$\begin{cases} \mathbf{y}^{n+1} = f_1(t^n; \mathbf{y}^n, \mathbf{z}^{n+1}, P_{IN}^{n+1}, Q_{OUT}^{n+1}), \\ \mathbf{y}^0 = \mathbf{y}_0, \\ \mathbf{z}^{n+1} = f_2(\mathbf{y}^n). \end{cases} \quad (3.19)$$

3.4. The 3D-0D geometric multiscale approach

Having presented the two models, with their different levels of accuracy in modeling the different zones, the key issue now regards their coupling. In fact, as said, the two models need to exchange information and appropriate boundary conditions must be applied to both of them. A geometric multiscale model is adopted [41] [26].

3.4.1. Coupling of the models

The 3D-0D multiscale coupled problem is composed by three sets of equations: the ones of the 3D model, the ones referred to the 0D model and the corresponding set of interface

coupling conditions.

Recalling the compact forms of the two strong problems (equations (3.3) and (3.18)), the strong formulation of the coupled 3D-0D model is the following:

For each $t \in T$ find \mathbf{u} , p , \mathbf{y} and \mathbf{z} such that:

3D model

$$\begin{cases} P_{3D}(\mathbf{u}, p) = \mathbf{0} \text{ in } \Omega, \\ \mathbf{u}(\mathbf{x}, 0) = \mathbf{0} \text{ in } \Omega; \end{cases} \quad (3.20)$$

Interface conditions

$$Q_{IN} = \int_{\Gamma_{IN}} \mathbf{u} \cdot \mathbf{n} \, d\gamma, \quad (3.21)$$

$$P_{IN} = -\frac{1}{|\Gamma_{IN}|} \int_{\Gamma_{IN}} T_F \mathbf{n} \cdot \mathbf{n} \, d\gamma, \quad (3.22)$$

$$Q_{OUT} = \sum_{j=1}^2 \int_{\Gamma_{OUT,j}} \mathbf{u} \cdot \mathbf{n} \, d\gamma, \text{ with } j = 1, 2, \quad (3.23)$$

$$P_{OUT} = -\frac{1}{|\Gamma_{OUT,j}|} \int_{\Gamma_{OUT,j}} T_F \mathbf{n} \cdot \mathbf{n} \, d\gamma, \text{ with } j = 1, 2; \quad (3.24)$$

0D model

$$\begin{cases} \frac{d}{dt} \mathbf{y}(t) = f_1(t, \mathbf{y}, \mathbf{z}, P_{IN}, Q_{OUT}), \\ \mathbf{y}(0) = \mathbf{y}_0, \\ \mathbf{z} = f_2(t, \mathbf{y}). \end{cases} \quad (3.25)$$

In the previous coupled problem, we have four interface conditions at the artificial sections $\Gamma_{IN}, \Gamma_{OUT,1}, \Gamma_{OUT,2}$. (3.21) and (3.23) represent the continuity of mass in terms of flow rates. (3.22) and the (3.24) represent the balance of interface forces, in terms of (average-in-space) normal traction for the fluid side [41] and of the pressure for the 0D side.

A picture of the coupled model can be seen in Figure 3.7, where the different compartments (both the 0D ones and the 3D one) are underlined by different colors.

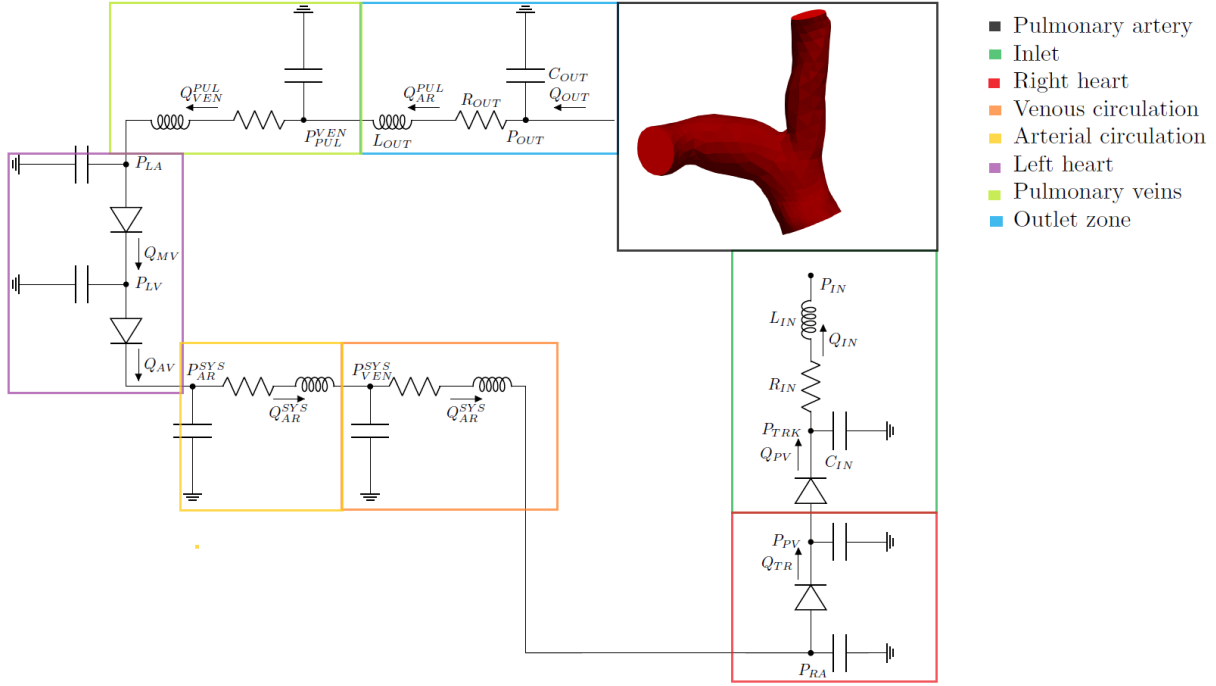


Figure 3.7: Geometric multiscale 3D-0D coupled model

3.4.2. Time discretization of the coupled problem

In order to discretize in time the coupled problem (3.20)-(3.25), we consider the discretization procedures described in sections 3.2.1 and 3.3.5 for the 3D and 0D subproblems, respectively. The same timestep has been adopted for both the 3D part and the 0D part of the model.

We obtain the following time discretization of the coupled problem:

For every $n = 0, 1, \dots, N - 1$ find \mathbf{u}^{n+1} , p^{n+1} , \mathbf{y}^{n+1} and \mathbf{z}^{n+1} such that:

3D model

$$\begin{cases} \rho \frac{\mathbf{u}^{n+1} - \mathbf{u}^n}{\Delta t} + \rho(\mathbf{u}^n \cdot \nabla) \mathbf{u}^{n+1} + \nabla p^{n+1} - \mu \Delta \mathbf{u}^{n+1} = \mathbf{0} \text{ in } \Omega, \\ \nabla \cdot \mathbf{u}^{n+1} = 0 \text{ in } \Omega, \\ \mathbf{u}^0 = \mathbf{0} \text{ in } \Omega, \\ \mathbf{u}^{n+1} = \mathbf{0} \text{ on } \Gamma_{WALL}; \end{cases} \quad (3.26)$$

Interface conditions

$$Q_{IN}^{n+1} = \int_{\Gamma_{IN}} \mathbf{u}^{n+1} \cdot \mathbf{n} \, d\gamma, \quad (3.27)$$

$$P_{IN}^{n+1} = -\frac{1}{|\Gamma_{IN}|} \int_{\Gamma_{IN}} T_F(\mathbf{u}^{n+1}, p^{n+1}) \mathbf{n} \cdot \mathbf{n} \, d\gamma, \quad (3.28)$$

$$Q_{OUT}^{n+1} = \sum_{j=1}^2 \int_{\Gamma_{OUT,j}} \mathbf{u}^{n+1} \cdot \mathbf{n} \, d\gamma, \text{ with } j = 1, 2; \quad (3.29)$$

$$P_{OUT}^{n+1} = -\frac{1}{|\Gamma_{OUT,j}|} \int_{\Gamma_{OUT,j}} T_F(\mathbf{u}^{n+1}, p^{n+1}) \mathbf{n} \cdot \mathbf{n} \, d\gamma, \text{ with } j = 1, 2; \quad (3.30)$$

0D model

$$\begin{cases} \mathbf{y}^{n+1} = f_1(t^n; \mathbf{y}^n, \mathbf{z}^{n+1}, P_{IN}^{n+1}, Q_{OUT}^{n+1}), \\ y^0 = \mathbf{y}_0, \\ \mathbf{z}^{n+1} = f_2(\mathbf{y}^n). \end{cases} \quad (3.31)$$

3.4.3. Completing the 3D interface conditions

Considering the problem (3.26)-(3.31), two issues arise when solving the 3D subproblem (3.26) using the boundary conditions prescribed by the 0D model. We will now detail these issues and our approach for their resolution.

3.4.3.1. Issue 1: About the tangential coupling

The 0D model only provides normal quantities, therefore no coupling condition is prescribed in tangential direction for the 3D model. To overcome this problem we assumed that on the artificial borders of the 3D domain the following Neumann condition holds:

$$T_F(\mathbf{u}, p) \mathbf{n} \cdot \boldsymbol{\tau}_j|_{\Gamma} = \mathbf{0}, \text{ with } \Gamma = \Gamma_{IN} \cup \Gamma_{OUT} \text{ and } j = 1, 2,$$

which entails the absence of tangential strains.

This boundary condition will be understood from here on and it is motivated by the fact that the boundary sections of the 3D domain are perpendicular to the vessel axis (as explained in section 2.6.1) and do not feature any shear stress.

3.4.3.2. Issue 2: Defective boundary conditions

Another problem that arises when solving (3.26)-(3.31) is that the 0D model can only provide integral quantities, which are not enough for the 3D model. These conditions are

in fact *defective* for this model and have to be appropriately completed.

Assuming that the 0D model assigns the scalar values Q and P at the interface Γ , we can refer to a couple of generic interface conditions as:

$$\int_{\Gamma} \mathbf{u} \cdot \mathbf{n} \, d\gamma = Q, \quad (3.32)$$

$$\frac{1}{|\Gamma|} \int_{\Gamma} T_F \mathbf{n} \cdot \mathbf{n} \, d\gamma = -P. \quad (3.33)$$

Regarding the flow rate interface equation (3.32), in this work we have adopted one of the possible existing strategies to overcome the *defective* problem, which is hypothesizing a velocity profile for the blood in the 3D model. Different profiles can be considered, in particular a parabolic profile, a flat profile or a pulsatile profile based on the Womersley number [38]. For the numerical solution of the final coupled model, we will impose for the 3D problem a condition on the flow rate at the inlet boundary (see section 3.4.4), which corresponds to the inflow of the pulmonary artery. The blood entering the pulmonary artery comes from the right ventricle which is a chamber that has a large volume. In such conditions, a well accepted hypothesis relies on assuming a flat velocity profile at the interface of interest [58]. To verify the correctness of this hypothesis we estimated the *Womersley* number, which is an adimensional value that quantifies the pulsatility of a flow [42]. It is defined as $W = \sqrt{\frac{2A\rho}{\mu}}$, where A is the characteristic area of the domain section, f is the time frequency of the flow rate signal and ρ and μ are respectively the density and viscosity of the fluid. If the Womersley number is large, the velocity profile can be considered relatively flat since the frequency of the pulsations is large. The estimate for this quantity gave us $W > 10$ for the two patients, therefore our hypothesis was confirmed by this result.

Regarding the condition on the balancing of the forces in (3.33), we have assumed for the 3D problem a normal constant traction on each section. This hypothesis is acceptable since the boundary sections of the 3D domain are flat and perpendicular to the vessel axis (see section 2.6.1) and the pressure changes mainly occur along the axial direction [42]. The two described hypotheses can be synthesized as follows:

$$\begin{cases} \mathbf{u} \cdot \mathbf{n}|_{\Gamma} = \frac{Q}{|\Gamma|}, \\ T_F(\mathbf{u}, p) \mathbf{n} \cdot \mathbf{n}|_{\Gamma} = -P, \end{cases} \quad (3.34)$$

where the first condition is, in fact, a Dirichlet boundary condition for the normal component of the velocity, while the second one is a Neumann boundary condition for the normal component of the strain.

3.4.4. The partitioned algorithm

Once introduced the time discretization of the problem in (3.26)-(3.31), we can define an algorithm in order to solve it in time. This consists in a partitioned procedure based on the exchange of the interface conditions. In particular, we impose at the inlet of the 3D model a Dirichlet boundary condition for the velocity by using the information on the 0D flow rate at the previous time step, while at the outlets, in an analogous way, a Neumann condition is considered. The two remaining conditions are instead prescribed as input for the 0D model.

The steps for the solution are reported in Algorithm 1: while iterating in time, the two subproblems (3D and 0D) are sequentially solved at each timestep and the interface conditions are equally split between them. The inputs of the algorithm regard first of all the imposition of the initial velocity \mathbf{u}^0 for the 3D model and of the initial unknown \mathbf{y}^0 for the 0D one. Moreover, since the first subproblem that is solved at each timestep is the 3D one, the initial conditions must also include the initial values of Q_{IN} and of P_{OUT} in order to solve the 3D problem the first time. After solving the 3D problem, the pressure at the inlet and flow rates at the outlets are computed and the 0D problem is then solved using this information. Finally, from the 0D solution it is possible to compute the flow rate at the inlet and pressure at the outlets in order to provide the new Dirichlet-Neumann conditions for the 3D problem at the following timestep.

Algorithm 1:

Let $Q_{IN}^0, P_{OUT}^0, \mathbf{u}^0, \mathbf{y}^0$ be given and set $n = 0$.

while $n < N$ **do**

Solve the 3D problem:

$$\begin{cases} P_{3D}(\mathbf{u}^{n+1}, p^{n+1}, Q_{IN}^n, P_{OUT}^n) = \mathbf{0}, \\ \mathbf{u}^{n+1} \cdot \mathbf{n}|_{\Gamma_{IN}} = \frac{Q_{IN}^n}{\Gamma_{IN}}, \\ T_F(\mathbf{u}^{n+1}, p^{n+1}) \mathbf{n} \cdot \mathbf{n}|_{\Gamma_{OUT,j}} = -P_{OUT}^n, \text{ with } j = 1, 2. \end{cases}$$

Compute the interface data to assign to the 0D model:

$$P_{IN}^{n+1} = -\frac{1}{|\Gamma_{IN}|} \int_{\Gamma_{IN}} T_F(\mathbf{u}^{n+1}, p^{n+1}) \mathbf{n} \cdot \mathbf{n} d\gamma,$$

$$Q_{OUT}^{n+1} = \sum_{j=1}^2 \int_{\Gamma_{OUT,j}} \mathbf{u}^{n+1} \cdot \mathbf{n} d\gamma, \text{ with } j = 1, 2.$$

Solve the 0D problem:

$$\begin{cases} \mathbf{y}^{n+1} = f_1(t^n; \mathbf{y}^n, \mathbf{z}^{n+1}, P_{IN}^{n+1}, Q_{OUT}^{n+1}), \\ \mathbf{z}^{n+1} = f_2(\mathbf{y}^n). \end{cases}$$

Compute the interface data to assign to the 3D model: Q_{IN}^{n+1} and P_{OUT}^{n+1} .

$n \rightarrow n + 1$

end

3.4.5. The wall shear stress

When performing simulations with this model we monitored the wall shear stress (WSS) as well as the flow rate and pressure of the blood. This quantity represents the magnitude of the tangential viscous forces that the blood exerts on the lumen of the artery [42]. It can be expressed in the following way:

$$WSS = \mu \sqrt{\sum_{j=1}^2 \left((\nabla \mathbf{v} \mathbf{n}) \cdot \boldsymbol{\tau}^{(j)} \right)^2} \text{ on } \Gamma_{WALL}, \quad (3.35)$$

where \mathbf{v} is the fluid velocity, \mathbf{n} is the outward unit normal to Γ_{WALL} and the $\boldsymbol{\tau}^{(j)}$ are the tangential unit vectors. This quantity is often monitored to verify if the chosen mesh is fine enough.

3.5. Differentiating the 0D outlets

In order to analyse more closely the flow repartition at the pulmonary bifurcation and evaluate a possible limitation of our model, we introduced a new variant of the multiscale coupled model described in section 3.4, in which the two 0D outlets, corresponding to the two pulmonary branches, were modeled by means of two different RLC circuits. Figure 3.8 schematically represents the transition from the model described in section 3.4 to this new variant. On the left, in dark blue, a single RLC circuit (L-network) represents both pulmonary branches in the 0D model and it is therefore linked to both branches of the 3D pulmonary artery. On the right, in the model variant, two parallel RLC networks are adopted in the 0D model (in light blue and green) and each one is linked to a single 3D branch.

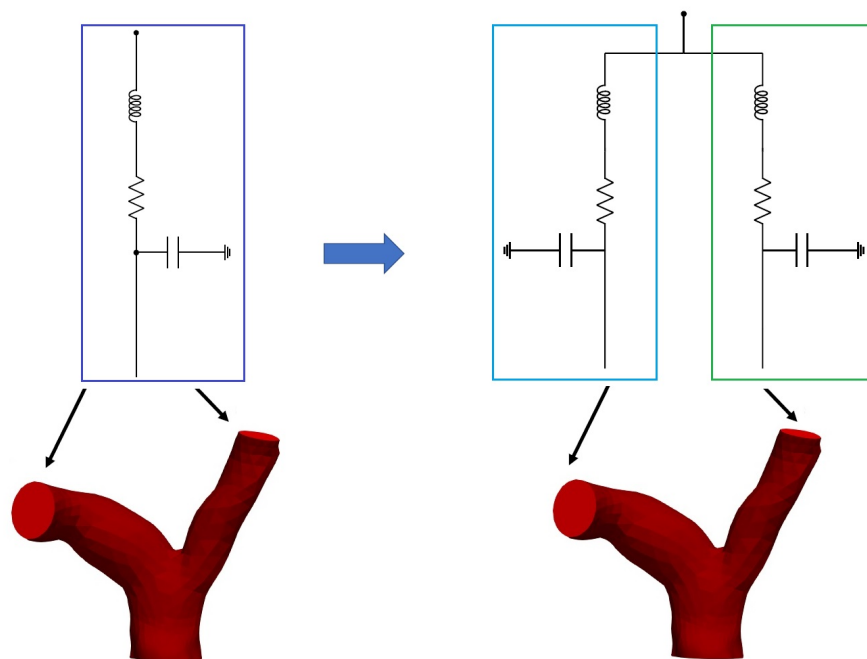


Figure 3.8: Variant of the 0D model where the two pulmonary artery branches are differentiated.

3.5.1. Model definition

The purpose of this differentiation was to be able to assign different pressure boundary conditions at the two outlets of the 3D domain. Indeed it can be expected that a higher pressure applied to a certain outlet would cause less flow to enter the corresponding branch and consequently more flow entering instead the other branch. Since the two

branches have different sections, it is quite likely for the pressure felt by the two flows to differ and therefore we decided to analyse the effect of adding this option to the model. Indeed an aim of implementing this variant was to test one of the possible limits of our model, which is the constraint of having to assign the same pressures at the outlets of the pulmonary artery. In fact we wanted to analyse whether or not significant differences could be observed on the hemodynamic quantities of the two patients in all three case scenarios when performing the simulations with this variant of the model.

To be able to perform this study we had to substitute the single variable Q_{OUT} of the 0D model with the couple of variables $Q_{OUT,Right}$ and $Q_{OUT,Left}$. The same idea was also applied to the pressure and the variable P_{OUT} was split into two variables: $P_{OUT,Right}$ and $P_{OUT,Left}$. Finally, also the resistor, capacitor and inductor had to be split into two different variables, one for the right pulmonary branch and one for the left one.

The new model is the one showed in Figure 3.9.

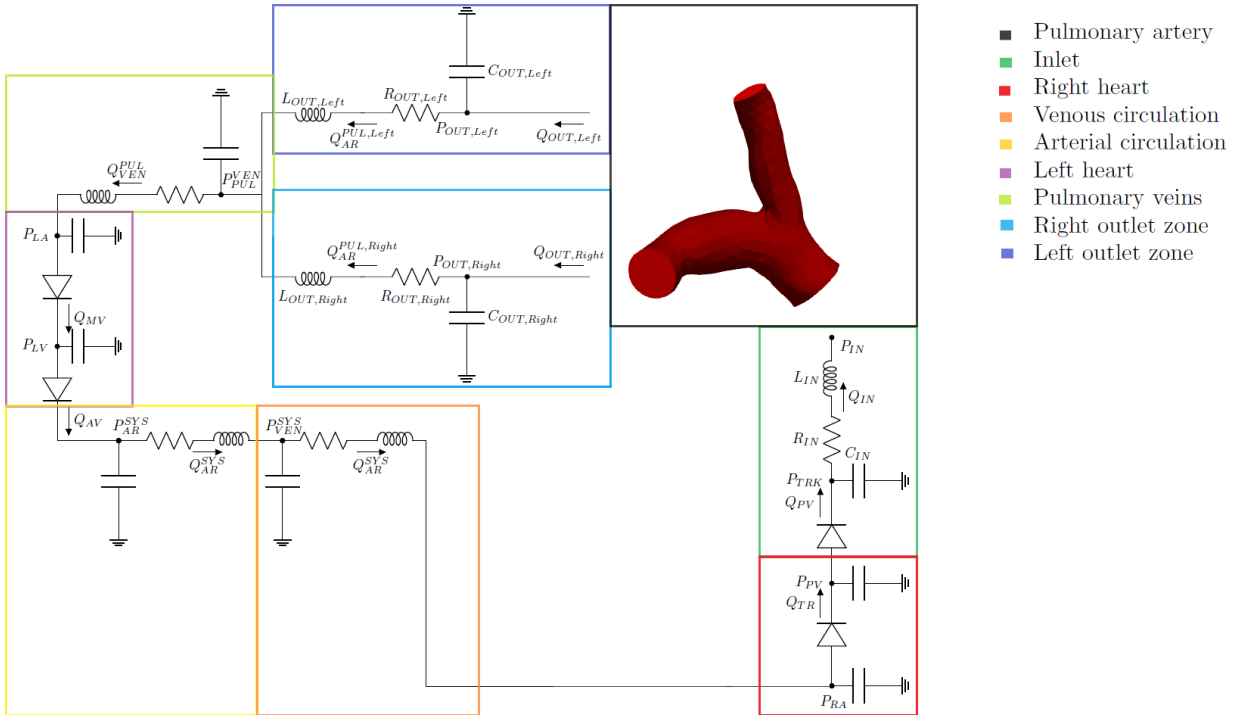


Figure 3.9: Geometric multiscale 3D-0D coupled model with two RLC circuits at the outlets of the pulmonary artery.

In this new configuration two separated sets of equations were needed for the two outlet zones in the 0D model. These were defined similarly to the case of a single outlet described by the system in (3.17).

An RLC circuit was used to model the **right outlet zone**:

$$C_{OUT,Right} \frac{dP_{OUT,Right}}{dt} = Q_{OUT,Right} - Q_{AR}^{PUL,Right}, \quad (3.36)$$

$$L_{OUT,Right} \frac{dQ_{AR}^{PUL,Right}}{dt} = -R_{OUT,Right} Q_{AR}^{PUL,Right} - (P_{VEN}^{PUL} - P_{OUT,Right}). \quad (3.37)$$

An RLC circuit was used to model the **left outlet zone**:

$$C_{OUT,Left} \frac{dP_{OUT,Left}}{dt} = Q_{OUT,Left} - Q_{AR}^{PUL,Left}, \quad (3.38)$$

$$L_{OUT,Left} \frac{dQ_{AR}^{PUL,Left}}{dt} = -R_{OUT,Left} Q_{AR}^{PUL,Left} - (P_{VEN}^{PUL} - P_{OUT,Left}). \quad (3.39)$$

The effect of this addition, however, does not only regard the 0D model, but also by the 3D one through the boundary conditions at the artificial boundaries, or interface conditions. The idea now is that each outflow of the 3D model exchanges information only with one of the two sides of the circuit bifurcation. Subsequently at each iteration of the model two boundary conditions on the pressure will be now required at the 3D outlets. At the same time when the 0D model has to be solved, it will need two flow conditions at the circuit bifurcation. The iterative steps of the model in the case of two RLC circuits at the outlets are show in Algorithm 2. In this setting, the flows exiting the two outlets of the artery are now not summed but assigned separately to the 0D model. At the same time the pressures are assigned separately by the 0D model to the two branches of the 3D one and can therefore now be different.

Algorithm 2:

Let $Q_{IN}^0, P_{OUT,Right}^0, P_{OUT,Left}^0, \mathbf{u}^0, \mathbf{y}^0$ be given and set $n = 0$.

while $n < N$ **do**

Solve the 3D problem:

$$\begin{cases} P_{3D}(\mathbf{u}^{n+1}, p^{n+1}, Q_{IN}^n, P_{OUT,Right}^n, P_{OUT,Left}^n) = \mathbf{0}, \\ \mathbf{u}^{n+1} \cdot \mathbf{n}|_{\Gamma_{IN}} = \frac{Q_{IN}^n}{\Gamma_{IN}}, \\ T_F(\mathbf{u}^{n+1}, p^{n+1}) \mathbf{n} \cdot \mathbf{n}|_{\Gamma_{OUT,Right}} = -P_{OUT,Right}^n, \\ T_F(\mathbf{u}^{n+1}, p^{n+1}) \mathbf{n} \cdot \mathbf{n}|_{\Gamma_{OUT,Left}} = -P_{OUT,Left}^n. \end{cases}$$

Compute the interface data to assign to the 0D model:

$$P_{IN}^{n+1} = -\frac{1}{|\Gamma_{IN}|} \int_{\Gamma_{IN}} T_F(\mathbf{u}^{n+1}, p^{n+1}) \mathbf{n} \cdot \mathbf{n} d\gamma,$$

$$Q_{OUT,Right}^{n+1} = \int_{\Gamma_{OUT,Right}} \mathbf{u}^{n+1} \cdot \mathbf{n} d\gamma,$$

$$Q_{OUT,Left}^{n+1} = \int_{\Gamma_{OUT,Left}} \mathbf{u}^{n+1} \cdot \mathbf{n} d\gamma.$$

Solve the 0D problem:

$$\begin{cases} \mathbf{y}^{n+1} = f_1(t^n; \mathbf{y}^n, \mathbf{z}^{n+1}, P_{IN}^{n+1}, Q_{OUT,Right}^{n+1}, Q_{OUT,Left}^{n+1}), \\ \mathbf{z}^{n+1} = f_2(\mathbf{y}^n). \end{cases}$$

Compute the interface data to assign to the 3D model:

$$Q_{IN}^{n+1}, P_{OUT,Right}^{n+1} \text{ and } P_{OUT,Left}^{n+1}.$$

$n \rightarrow n + 1$

end

3.5.2. On the choice of the outlet resistances

Another reason that brought us to define this variant of the model was that we were interested in analysing the relationship between the shape of the branches of the artery and the pressure felt by the blood flowing inside. The effect of the pressure, in fact, alters the proportion of flow entering the two branches downstream of the bifurcation and branches with different geometrical characteristics are likely to be subject to different pressures. In an RLC circuit assigning a higher value of resistance means increasing the voltage (and therefore the pressure, in our context) of that compartment. Therefore varying the resistances at the outlets of the 0D model ($R_{OUT,Right}$ and $R_{OUT,Left}$ in equations (3.36) and (3.38)) implies the imposition of different pressures on the two pulmonary branches. In the absence of patient-specific measured values for the pressures or flow rates of the

two patients under study, since they are not usually taken during standard follow-up exams, we propose three different approaches for the choice of the resistance values [8]: one based on a formula that computes these values directly, and two based on estimated flow repartitions.

3.5.2.1. Formula for the resistance values

In [56] a 3D-0D model is adopted for the study of hemodynamic forces in the pulmonary tree of pediatric patients with pulmonary artery hypertension (PAH). In this case the model is coupled not with an RLC network but with an RCR one. The adopted formula to compute the resistances closest to the outlets is the following:

$$R_i = \frac{A}{A_i} R, \quad (3.40)$$

where R_i is the resistance that must be assigned at outlet i and A_i is its area. R and A are instead respectively the total resistance and total area of all the right or left outlets. This formula was also applied by [24] in a similar context, but in the case of healthy conditions.

In this work we adopted formula 3.40 directly applied to the main pulmonary bifurcation by solving a system of two equations in two unknowns ($R_{OUT,Right}$ and $R_{OUT,Left}$), which takes the following form:

$$\begin{cases} R_{OUT,Right} = \frac{|\Gamma_{OUT,Right}| + |\Gamma_{OUT,Left}|}{|\Gamma_{OUT,Right}|} R_{eq}, \\ R_{OUT,Left} = \frac{|\Gamma_{OUT,Right}| + |\Gamma_{OUT,Left}|}{|\Gamma_{OUT,Left}|} R_{eq}, \end{cases} \quad (3.41)$$

where

$$R_{eq} = \left(\frac{1}{R_{OUT,Right}} + \frac{1}{R_{OUT,Left}} \right)^{-1}$$

is the equivalent resistance of the two parallel RLC outlet circuits. The outlet surface areas $|\Gamma_{OUT,Right}|$ and $|\Gamma_{OUT,Left}|$ were instead measured from the 3D reconstructed geometries using Paraview.

By computing the resistances at the outlets of the 3D model with this approach, since the two outlets have different areas, $R_{OUT,Right}$ and $R_{OUT,Left}$ resulted different and consequently we were able to assign different pressures at the outlets. However, this formula, while giving an indication on the values of the resistances, does not provide information on the consequent flow repartition to expect. Therefore, in order to analyse the reliability of the results given by this method in our specific context, we decided to investigate the

theories on flow repartition in blood vessels.

3.5.2.2. Resistances based on Murray's law

Cecil D. Murray was an american physiologist who in 1926 published a paper entitled *The Physiological Principle of Minimum Work, I. The Vascular System and the Cost of Blood Volume* [30]. In his work he derived a very important relation on the connection of large vessels to small ones which applies to both asymmetrical and symmetrical branching systems [46]. The law states that the cube of the radius of a parent vessel should equal the sum of the cubes of the radii of the daughter vessels. Considering that the flow rate conserves itself, this law can be restated with the following formula:

$$\frac{Q_i}{\sum_i Q_i} = \frac{D_i^3}{\sum_i D_i^3}, \quad (3.42)$$

where Q_i is the flow rate of outlet i and D_i is its diameter.

Another way to state this law is to say that in an optimum vascular system the vessels are connected in a way such that the radii cubed sum is always equal to a constant value. This law has been derived for biological systems but also has non biological applications. The main idea behind Murray's law is that physiological vascular systems, thanks to evolution through natural selection, have achieved an optimum arrangement in every segment of vessel, so that the flow circulation is maintained with the least possible biological work [46]. According to Murray's theory, the energy needed for the flow is composed by two terms: a term that represents the energy needed to overcome the viscous drag in a fluid which follows the Poiseuille law (P_f), and the energy required to involve the blood and vessel tissue in the flow (P_m). Both these terms are related to the vessel radius, though with an opposite trend, the first term of energy decreases when the radius increases while the second one increases with the radius. Thus a vessel cannot be neither too large nor too small in order to minimize the total power $P_t = P_f + P_m$. Murray's law is obtained by solving a minimization problem in the setting of a cylindrical vessel. The full derivation of the law is reported in [46].

Concerning our study, we adopted formula (3.42) to calculate the proportion of the total flow expected to enter the right branch of the pulmonary artery and then proceeded by exploiting the flow conservation principle to compute the same proportion for the left

branch. These two operations were performed by solving the following system:

$$\begin{cases} \frac{Q_{OUT,Right}}{Q_{OUT,Right} + Q_{OUT,Left}} = \frac{D_{OUT,Right}^3}{D_{OUT,Right}^3 + D_{OUT,Left}^3}, \\ \frac{Q_{OUT,Left}}{Q_{OUT,Right} + Q_{OUT,Left}} = 1 - \frac{Q_{OUT,Right}}{Q_{OUT,Right} + Q_{OUT,Left}}, \end{cases} \quad (3.43)$$

where the outlet diameters $D_{OUT,Left}$ and $D_{OUT,Right}$ were measured with Paraview. Once calculated the the proportions of the total flow entering each artery according to Murray's law, which are the left hand sides of system (3.43), no formula was adopted to compute the resistance values $R_{OUT,Right}$ and $R_{OUT,Left}$ but we instead appropriately tuned these two parameters in order to obtain the desired flow repartition.

3.5.2.3. Resistances based on the Chnafa law

In [12] an alternative to Murray's law is proposed. This law is applied at each bifurcation and it estimates the ratio of the flow rates in the two branches originated at the bifurcation in terms of the diameters of their lumen, according to the following rule:

$$\frac{Q_1}{Q_2} = \left(\frac{D_1}{D_2}\right)^2. \quad (3.44)$$

In this formula Q_1 is the flow rate of outlet 1 and D_1 is its diameter. The same holds for outlet 2. This law was proposed in the context of cerebrovascular simulations but was also applied by [8] in the specific context of the main pulmonary bifurcation for adult patients with rTOF.

Indeed, the Murray law may not apply in our specific context of interest since one its hypothesis consists in the choice of a laminar flow [46]; however, because of the complex geometries of the arteries, especially the one of Patient 2, the flow may not always be laminar around the bifurcation. Furthermore, the two powers (P_f and P_m) cited in section 3.5.2.2 for the minimization problem should in theory relate to two different radii: the radius of the lumen and the radius of the whole artery, wall included. Since in this formulation of Murray's law a unique radius is considered (that of the lumen), it is possible for it to be valid only for thin arteries [46]. Finally [46] reports some studies that showed that large vessels tend to maintain a constant total cross-sectional area which does not change significantly until the diameters reach the order of 1-2mm. So it is suggested that the main pulmonary bifurcation, together with the aortic one, may follow a $\sum_i r^2$ rule instead of a $\sum_i r^3$ one.

In our study we therefore decided to apply formula (3.44), to which we will refer as Chnafa law, in order to compare it with the results of the application of Murray's principle. We

calculated the proportion of flow entering the right branch with respect to the one entering the left one and exploited the flow conservation principle to compute the two proportions with respect to the total flow entering the artery. These operations consisted in the resolution of the following system:

$$\begin{cases} \frac{Q_{OUT,Right}}{Q_{OUT,Left}} = \left(\frac{D_{OUT,Right}}{D_{OUT,Left}} \right)^2, \\ \frac{Q_{OUT,Left}}{Q_{OUT,Right} + Q_{OUT,Left}} + \frac{Q_{OUT,Right}}{Q_{OUT,Right} + Q_{OUT,Left}} = 1. \end{cases} \quad (3.45)$$

Once calculated the flow repartition between the left and right main pulmonary branches estimated with this law, our initial idea was to proceed as for the flow repartition obtained with Murray's law in the previous section, and tune the $R_{OUT,Right}$ and $R_{OUT,Left}$ parameters. However, by solving system (3.45) we noticed that the estimated flow repartition was very close to the one we had obtained when imposing the resistance values calculated with formula (3.40) (more details on this result we be explained in section 4.3.4). Therefore, no tuning was needed in this case and the study on the splitting of the flow for each scenario was performed by comparing the simulation performed with Algorithm 1 with two simulations performed with Algorithm 2: one based on Murray's law for the flow repartition, in which the values of the resistances ($R_{OUT,Right}$ and $R_{OUT,Left}$) were appropriately tuned, and one based on the Chnafa law, in which the resistances were instead calculated by solving system (3.41).

4 | Description of simulations and calibration procedures

In this chapter we first of all detail the implementation of all the scenarios (section 4.1). We then describe the general settings of the simulations (section 4.2). Section 4.3 is instead dedicated to the calibration of the model parameters.

4.1. Description of the different simulations

Having presented the patient-specific geometries and detailed the numerical methods employed, we now proceed by delineating the settings for all the performed numerical simulations we have performed.

Keeping in mind the three scenarios of interest (*Healthy*, *Pre* and *Post*), we performed for each scenario three different simulations:

- A simulation applying Algorithm 1, and therefore the same pressure boundary condition at the two outlets. These will be simply referred to as the *Healthy*, *Pre* and *Post* simulations, respectively.
- A simulation applying Algorithm 2 in which we assigned two different pressures at the outlets aimed at obtaining the Murray flow repartition estimated by equations (3.43). We will refer to these simulations respectively as *Healthy-Murray*, *Pre-Murray* and *Post-Murray* simulations.
- A simulation applying Algorithm 2 in which we assigned the resistances at the outlet boundaries given by formula (3.40) which gave a flow repartition coherent with the Chnafa law described by (3.44). We will refer to these simulations as respectively *Healthy-Splitting*, *Pre-Splitting* and *Post-Splitting* simulations.

We now detail the exact settings for each of the nine simulations of both patients both from a 3D and a 0D point of view.

4.1.1. Simulations based on Algorithm 1

For the first set of simulations, in which we assumed the hypothesis that the normal tractions at the two outlets of the artery were the same, we made use of Algorithm 1. These simulations were conducted as follows.

- **Healthy simulation.**

In this configuration we simulated a healthy condition with the geometries obtained in the *Healthy/Pre* case (see section 2.6.1). The configuration of the 3D-0D model adopted is the one shown in Figure 4.1, at the top, which is a zoom of the model in Figure 3.7. A single RLC circuit is applied at both outlets of the 3D model (blue zone) and the pulmonary valve is present in the inlet region (green zone) replicating the natural pulmonary valve.

- **Pre simulation.**

In order to simulate the pre-operative condition of the patients (*Pre* scenario), we simulated the model without the diode that represented the pulmonary valve in the 0D model. To simulate the absence of the valve we assigned the resistance of the corresponding diode to be equal to its minimum value during the whole heartbeat. Referring to the values cited in section 3.3.3, we fixed $R_{max} = R_{min} = 0.0075 \frac{mmHg \cdot s}{ml}$ for the pulmonary valve. This corresponded to simulating the valve as always opposing a minimum resistance to the flow, and therefore as always open. The resistance assigned by the valve when open was very small but not zero since the diode was non ideal. However, approximately, we decided to consider the configuration with a fixed open diode as equivalent to the absence of a pulmonary valve. The resulting configuration was the one in Figure 4.1, at the bottom, which is the same as the one at the top, but without the diode in the inlet zone (in green), which is substituted by a piece of circuit with a constant resistance equal to the minimum resistance of the diode. Also for this simulation, we adopted the two *Healthy/Pre* meshes of the patients (see section 2.6.1).

- **Post simulation**

To simulate the post-operative condition (*Post*) of the patients, we included the pulmonary diode in the 0D model and we adopted the *Post* meshes described in section 2.6.2 in order to take into account of the stent of the prosthetic valve that alters the geometry of the artery's inflow. Regarding the 0D model, we considered once again the configuration at the top of Figure 4.1, with the diode acting this time as the leaflets of the prosthetic valve.

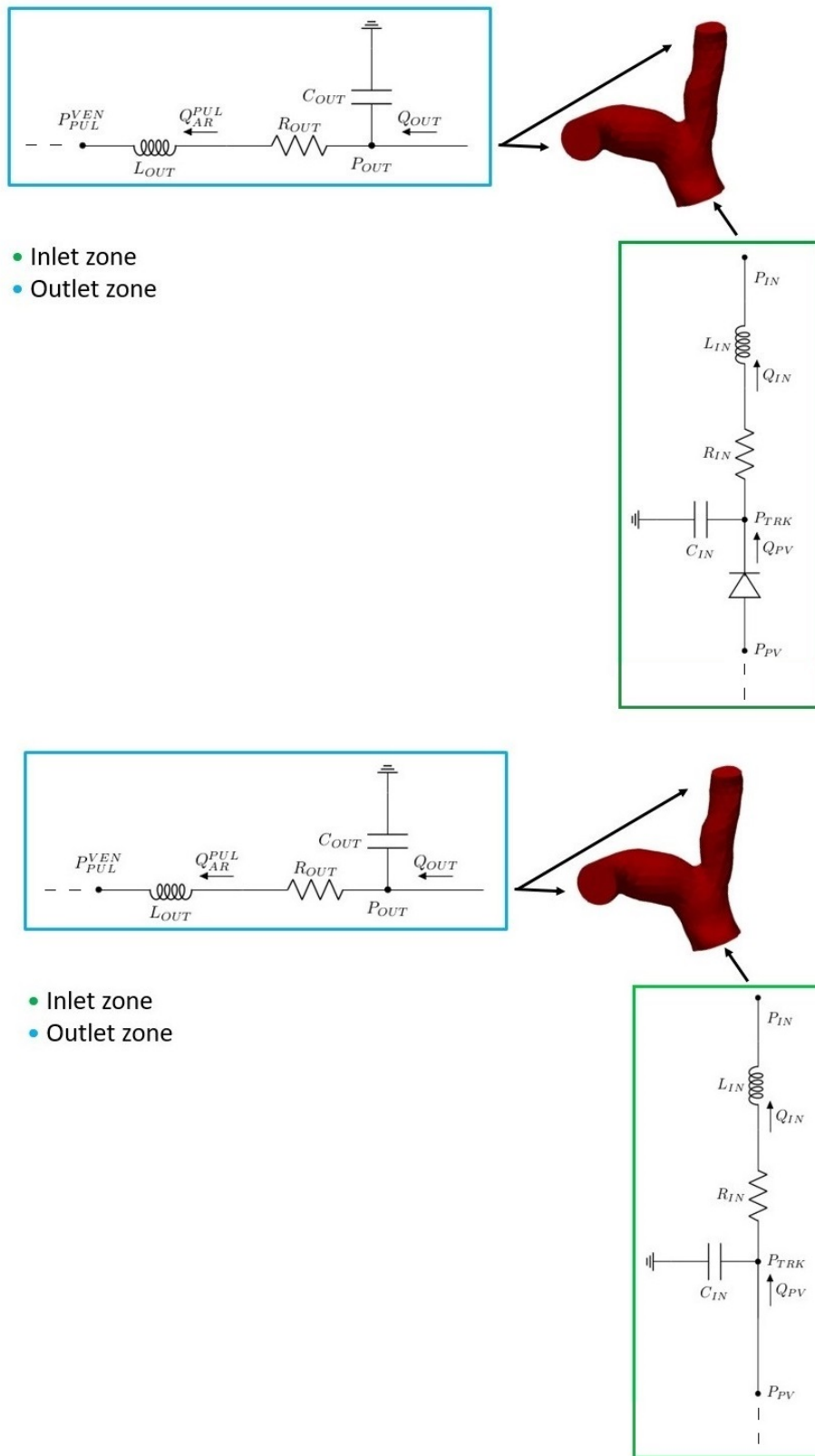


Figure 4.1: Algorithm 1. Top: *Healthy* and *Post* scenarios, zoom of the zones of interest in Figure 3.7. Bottom: *Pre* scenario: zoom of the zone of interest in Figure 3.7 after the removal of the diode representing the pulmonary valve.

4.1.2. Simulations based on Algorithm 2

We then performed the simulations for the same scenarios adopting Algorithm 2 and therefore differentiating the two outlet boundary conditions. The settings were defined as follows.

- **Healthy-Murray simulation.**

To perform the *Healthy-Murray* simulation we adopted the configuration with two separate RLC circuits for the two outlets, as shown in Figure 4.2, on the top, which is a zoom of the zone of interest in Figure 3.9. We applied as resistances at the outlets ($R_{OUT,Right}$ and $R_{OUT,Left}$) the ones that gave us the desired flow repartition predicted by Murray's law and simulated the circulation with the *Healthy/Pre* mesh.

- **Pre-Murray simulation.**

In order to perform the *Pre-Murray* simulation we adopted the configuration shown in Figure 4.2, at the bottom, with two 0D outlets but no pulmonary valve at the inlet, setting the resistance values in order to obtain the Murray flow repartition. Regarding the mesh we adopted the *Healthy/Pre* one.

- **Post-Murray simulation.**

Regarding the *Post-Murray* simulation, we considered the configuration shown at the top of Figure 4.2 but employing the *Post* meshes. We set the outlet resistance values in order to obtain the flow repartition expected by the law of Murray.

- **Healthy-Splitting simulation.**

To perform the *Healthy-Splitting* simulation we adopted the same configuration as the Healthy-Murray one, but assigned different resistances at the two pulmonary outlets, in particular the ones calculated with formula (3.41). We adopted the *Healthy/Pre* mesh.

- **Pre-Splitting simulation.**

For the *Pre-splitting* simulation we adopted the same configuration of the *Pre-Murray* one, changing the resistance values according to formula (3.41).

- **Post-Splitting simulation.**

Finally for the *Post-Splitting* simulation we considered the same situation as the Post-Murray simulation changing the values of the resistances according to the formula.

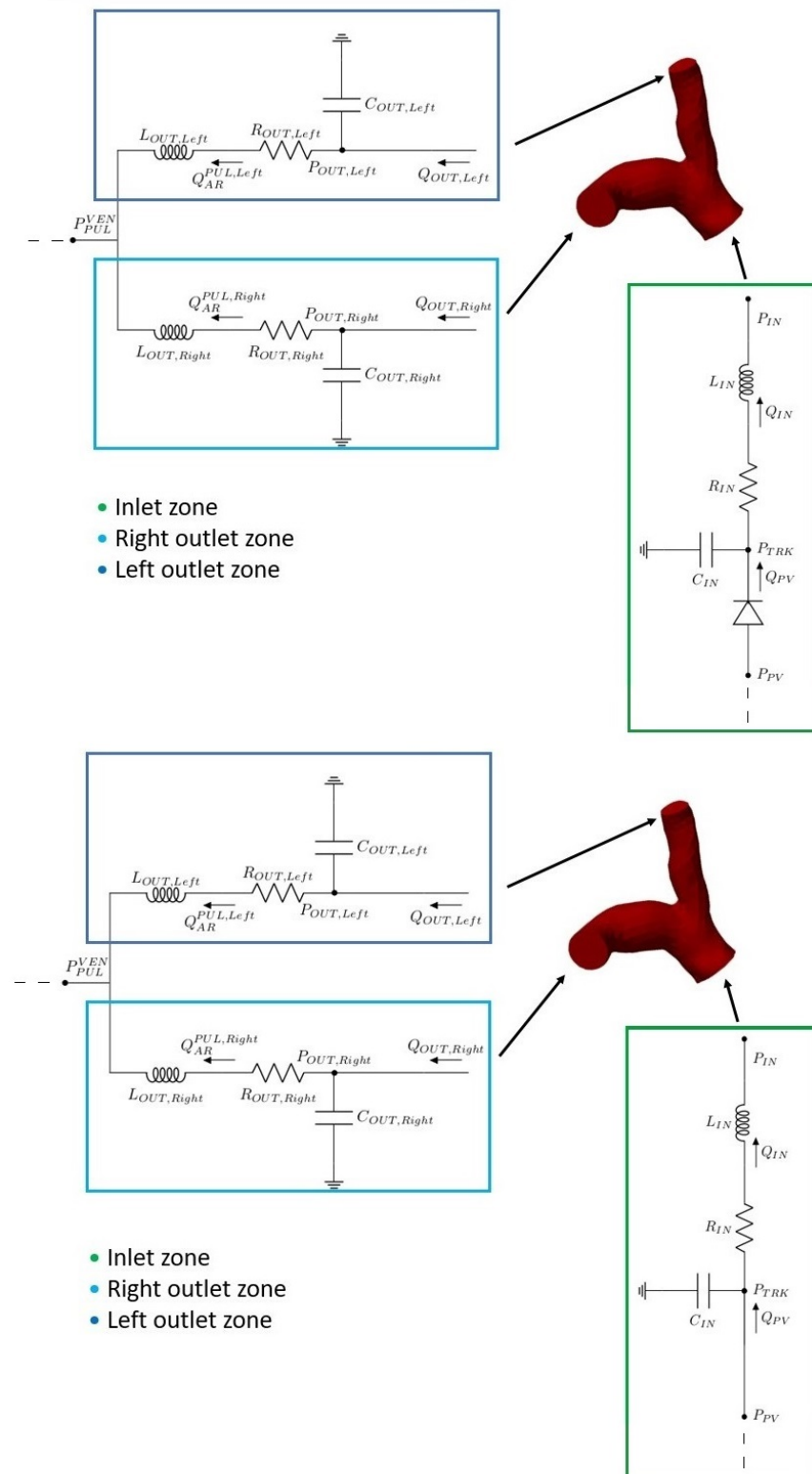


Figure 4.2: Algorithm 2. Top: *Healthy-Murray* and *Healthy-Splitting*, *Post-Murray* and *Post-Splitting* simulations: zoom of the zone of interest in Figure 3.9. Bottom: Algorithm 2. *Pre-Murray* and *Pre-splitting* simulations: Zoom of the zone of interest in Figure 3.9 but without the pulmonary valve (diode).

4.2. General settings of the simulations

To perform all the simulations, we made use of the *Life^x* [23] library, which is a high-performance Finite Element library that focuses on the modeling of cardiac applications. This library was developed by the MOX department of the university Politecnico di Milano, which is a laboratory for modeling and scientific computing in science and engineering. It is written in C++ and based on a deal.II finite element core.

4.2.1. Simulation details

All the results have been obtained by launching the simulations with the High Performance Computing (HPC) supercomputers of the MOX department of Politecnico di Milano. In particular, for Patient 1 a Xeon E5-2640 v4 processor with 20 cores and a RAM of 20GB has been used. For Patient 2, since the meshes had a larger number of elements, a Xeon E5-4610 v2 processor with 32 cores and 252G of RAM was employed.

We chose \mathbb{P}_1 Finite Elements for both the velocity and the pressure spaces, while the employed stabilization technique was the SUPG-PSPG method (see section 3.2.4). The backflow stabilization technique described in section 3.2.3 was applied to both outlets. To solve the linear 3D problem we adopted the GMRES method fixing to 1000 the maximum number of iterations, a tolerance of $1e-10$ and employing a SIMPLE preconditioner [39]. The blood density and viscosity were respectively assumed equal to $1.06e3 \frac{kg}{m^3}$ and $3.5e-3$ [42]. Finally, we set to 0.8s the length in time of each heartbeat, as it is a normal length in healthy conditions [26].

4.2.2. Mesh-independence study and timestep tuning

We started from a *mesh-independence* study of the solution in order to verify that the obtained results did not depend on the chosen mesh. Indeed, the meshes presented in Chapter 2 and in particular the choice of the edgelengths, were the final ones obtained after this study. To perform this analysis, we tried to refine the meshes more than once, increasing the number of elements. For the *Healthy/Pre* mesh of Patient 1 (see section 2.7) we tested a mesh with 70,876 elements and an average cell diameter of 0.0021m. Regarding Patient 2, we considered a mesh of 130,510 elements and an average cell diameter of 0.0019mm. We then performed some simulations adopting Algorithm 1 and verified whether important quantities, such as the WSS or the velocity and pressure profiles, varied of more than 5%. The chosen meshes were the coarser ones that gave acceptable results according to this criterion.

An analogous study was adopted to tune the timestep Δt . We considered the timesteps $0.00001s$, $0.0005s$ and 0.0001 and ended up setting the value $\Delta t = 0.0005s$ since it was the biggest timestep that gave us results that stabilized after few heartbeats and did not differ significantly from the ones obtained with smaller timesteps.

4.2.3. Typical calibration issues

After the mesh and timestep definition, a very important task was the one of calibration of the 0D parameters. Indeed, simulating the model with incorrect parameters led to two typical types of problems in the solutions. Both are shown in Figure 4.3. On the left we can see a case in which the the 0D variable Q_{IN} , belonging to the inlet compartment of the 0D model, at the interface with the 3D one (green box of Figure 3.7) oscillates very much and with increasing magnitude. This causes the GMRES algorithm used to solve the linear system to not converge in the given 1000 maximum iterations set. This behaviour was observed for example when we reduced too much the inductance L or capacitance C of the inlet RLC circuit. On the right of the same Figure, we show instead another typical phenomenon we observed during the simulations that regards the trend of the same variable Q_{IN} . The graph shows a case where the inlet flow keeps growing without reaching a regime value and this phenomenon was particularly noticeable when we varied too much the elastances of the 0D right ventricle E_a and E_b (in the red box of Figure 3.7).

For all the simulations, we decided to set a total of six heartbeats in order to obtain results as stable as possible. Since each heartbeat was set to last $0.8s$, this meant fixing the time interval $T = 4.6s$.

4.3. Calibration of the 0D model parameters

In order to avoid the cited issues, we had to appropriately tune our model. The idea was to calibrate the 0D parameters in order to both obtain physiological results compared to the ones we found in literature for an average healthy person and to match some patient-specific measures coming from clinicians. In particular, regarding Patient 1, we had at our disposal, thanks to the Niguarda Hospital of Milan, some medical follow-up exams in addition to the CT scans already cited for the mesh reconstruction. We therefore focused on the clinical values of this patient, reported in the exams, in order to obtain coherent enough results with his specific conditions. For the model calibration procedure, we focused on the *Healthy* scenario of Patient 1. The idea behind this scenario was in fact to

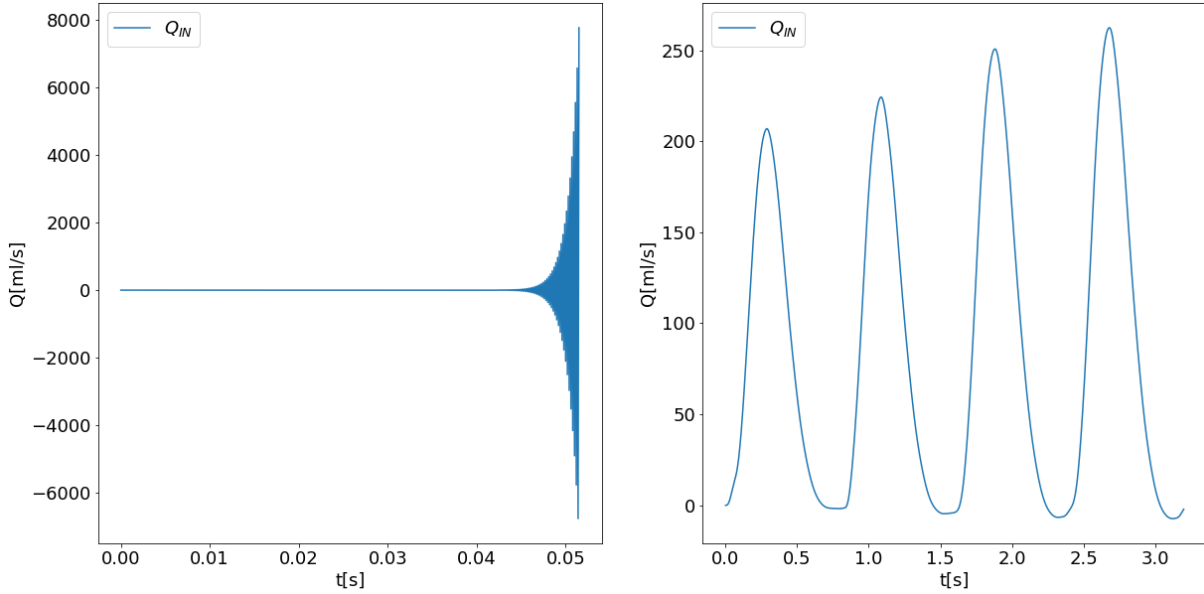


Figure 4.3: Example of two types of incorrect calibration. Left: Oscillations and non convergence of the linear solver. Right: Increasing flow rate at each heartbeat.

simulate the blood flow of a person which had the specific pulmonary artery of Patient 1, but no pathological conditions. However, because of the clinical values reported in the medical exam of this patient, we had to take into account of the fact that possibly not all the hemodynamic quantities would belong to the normal ranges.

Regarding Patient 2, we adopted the same parameters, since, in absence of further information, having the two patients a similar medical history, we considered this approximation to be acceptable.

4.3.1. About clinical data

The clinical exam at our disposal for Patient 1 dated back to 2016 and contained information on the volume of the patient's ventricles. The value of the telediastolic volume of the right ventricle, or *Right Ventricle End Diastolic Volume* (RVEDV) was reported as equal to 110ml, while the right ventricle telesystolic volume, or *Right Ventricle End Systolic Volume* (RVESV) was equal to 58ml. These two values correspond respectively to the volume of the right ventricle at the end of the systole, when it is completely contracted and at the end of the diastole, when it is relaxed. Another information contained in this exam was the *Right Ventricle Ejection Fraction* (RVEF) which is defined as $\frac{RVEDV - RVESV}{RVEDV} * 100$, and was reported equal to 47%. The RVEF represents the percentage of blood in the ventricle that is pumped out during the systole. The numerator of this expression, which is the difference between the RVEDV and the RVESV, is instead defined as *Stroke Volume*.

The same information was available also for the left ventricle of the patient and all these quantities are reported in Table 4.1.

	Clinical measures(2016)
RVEDS	110 ml
RVESV	58 ml
RVEF	47%
LVEDS	110 ml
LVESV	55 ml
LVEF	50%

Table 4.1: Clinical measures, corresponding to the ventricle parameters of Patient 1, used to calibrate the 0D model parameters.

4.3.2. Initial conditions of the 0D model

Since our simulations began with the ventricles' diastole, we assigned the values of the RVEDV and the LVEDV of the medical exams as initial conditions for the two 0D ventricles. The 0D initial conditions for the simulations with both Algorithms 1 and 2 are reported in Table 4.2. In particular, we assigned an initial pressure at the outlets of 14.90mmHg , which is a normal mean pulmonary artery pressure [54], and an initial flow rate of 0ml/s at the inlet, since, during the diastole, with a functioning valve, the flow is not present.

Parameters	Values
P_{OUT}	14.90 mmHg
$P_{OUT,Right}, P_{OUT,Left}$	14.90 mmHg
Q_{IN}	0 ml/s
RV volume	110 ml
LV volume	110 ml
RA volume	50 ml
LA volume	64.5 ml

Table 4.2: Calibrated initial conditions for the 0D model. Algorithm 1 and 2.

4.3.3. Tuning of the 0D model parameters

In this section we first detail the values of the 0D model parameters that were assigned following the tuning procedure. The latter was based on finding the best set of parameters that matched the physiological measures reported in Table 4.1 and other literature values [25], [57], [54], [48], [22], [54]. Such calibration procedure was performed with a trial-and-error strategy starting from suitable initial guesses for the parameters suggested by [26].

Table 4.3 shows the calibrated parameters of the 0D model regarding the heart chambers and, in particular, the elastances E_a and E_b and the duration of the contraction and relaxation periods. We underline the values of the elastances of the RV since they were specific object of a study (described in section 4.3) aimed at obtaining coherent results with the Patient 1's medical exams.

Table 4.4 shows instead the circulation RLC parameters assigned in the 0D model regarding the pulmonary and systemic venous systems and the systemic arterial system.

Heart chambers	$E_a(\frac{mmHg}{ml})$	$E_b(\frac{mmHg}{ml})$	$\Delta t_{contr}(s)$	$\Delta t_{relax}(s)$
Left atrium	0.07	0.09	0.17	0.17
Right atrium	0.06	0.07	0.17	0.17
Left ventricle	2.75	0.08	0.34	0.15
Right ventricle	0.42	0.16	0.34	0.15

Table 4.3: 0D model: calibrated parameters of the heart chambers.

Compartments	$\mathbf{R}(\frac{mmHgs}{ml})$	$\mathbf{L}(\frac{mmHgs^2}{ml})$	$\mathbf{C}(\frac{ml}{mmHg})$
Pulmonary venous system	0.0357	0.0005	16.00
Systemic arterial system	0.6400	0.0050	1.20
Systemic venous system	0.2600	0.0005	60.00

Table 4.4: 0D model: calibrated parameters of the pulmonary and systemic venous systems and the systemic arterial system.

Table 4.5 shows the assigned values for the maximum and minimum resistances of the four heart valves. In the *Pre* scenarios of both patients, to simulate the absence of the pulmonary valve, we set its maximum resistance value (R_{max}) equal to the minimum one (R_{min}).

Cardiac valves	$R_{min}(\frac{mmHg s}{ml})$	$R_{max}(\frac{mmHg s}{ml})$
Mitral	0.0075	75006.2
Aortic	0.0075	75006.2
Tricuspid	0.0075	75006.2
Pulmonary (<i>Healthy, Post</i>)	0.0075	75006.2
Pulmonary (<i>Pre</i>)	0.0075	0.0075

Table 4.5: 0D model: calibrated parameters of the heart valves.

In Table 4.6 we report instead the calibrated parameters for the RLC circuits at the inlet and outlet zones of the configuration described in Algorithm 1. These values were applied for the *Healthy*, *Pre* and *Post* scenarios of both patients.

Compartments	$\mathbf{R}(\frac{mmHg s}{ml})$	$\mathbf{L}(\frac{mmHg s^2}{ml})$	$\mathbf{C}(\frac{ml}{mmHg})$
Inlet zone	0.0321	0.0025	2.00
Outlet zone	0.0225	0.0018	0.05

Table 4.6: 0D model. Algorithm 1: calibrated parameters of the pulmonary artery compartments in the *Healthy*, *Pre* and *Post* scenarios for both patients.

All the described parameters were assigned in the same way for both patients. Table 4.7 shows instead the results of the calibration of the RLC parameters at the inlet and outlets of the artery when simulating with Algorithm 2. We particularly focused on the tuning of the outlet resistances imposing at the two now differentiated outlets appropriate values in order to either obtain the Murray flow repartition (*Murray* simulations) or to follow the formula for the resistances in equation (3.40) (*Splitting* simulations). Since the geometries of the two patients, and therefore their outlet sections, are different, the assigned values of the resistances were not the same for the two patients.

We specify that the values reported in Table 4.7 were considered, regarding each patient, for both the two *Healthy/Pre* and *Post* meshes. Indeed, the substantial difference between the two geometries of each patient only regarded the inflow region which wasn't subject of the repartition analysis from the 0D point of view.

Simulation	Compartments	\mathbf{R} ($\frac{mmHg \cdot s}{ml}$)	\mathbf{L} ($\frac{mmHg \cdot s^2}{ml}$)	\mathbf{C} ($\frac{ml}{mmHg}$)
Patient 1 <i>Murray</i>	Inlet zone	0.0321	0.0025	2.00
	Right outlet zone	0.0050	0.0018	0.05
	Left outlet zone	0.0230	0.0018	0.05
Patient 2 <i>Murray</i>	Inlet zone	0.0321	0.0025	2.00
	Right outlet zone	0.0044	0.0018	0.05
	Left outlet zone	0.0290	0.0018	0.05
Patient 1 <i>Splitting</i>	Inlet zone	0.0321	0.0025	2.00
	Right outlet zone	0.0110	0.0018	0.05
	Left outlet zone	0.0230	0.0018	0.05
Patient 2 <i>Splitting</i>	Inlet zone	0.0321	0.0025	2.00
	Right outlet zone	0.0100	0.0018	0.05
	Left outlet zone	0.0290	0.0018	0.05

Table 4.7: 0D model. Algorithm 2: calibrated parameters of the pulmonary artery compartments in the *Murray* and *Splitting* simulations of Patient 1 and Patient 2.

During the tuning procedure, we monitored both the 3D and the 0D compartments making sure that the different hemodynamic quantities were coherent with both average values taken from literature and (in case of the right ventricle volume) the specific values measured in the clinical exam of Patient 1.

We will now describe the main quantities of the 0D model that we monitored:

1. The RV volume and pressure in the 0D model;
2. The 0D variables Q_{IN} , $Q_{OUT,Right}$ and $Q_{OUT,Left}$ representing the average-in-space flow rates at the inlet and outlets of the 3D model;
3. The 0D variables P_{IN} , P_{OUT} , $P_{OUT,Right}$ and $P_{OUT,Left}$, representing the average-in-space pressures at the inlet and outlets of the 3D model;

The calibration procedure was performed in parallel for all these quantities, verifying their variation for each simulation in relation to the variation of the parameters, and making sure none of values were too far away from the acceptable quantities. We now show the results of the calibration for the *Healthy* scenario of Patient 1.

RV volume and pressure

The first quantity that we monitored was the RV volume since we had information on the actual values of this parameter for Patient 1. By calibrating the elastances of the RV 0D model, we tried to reproduce the corresponding values reported in Table 4.8. We compared the obtained values of RVEDV, RVESV and RVEF with the medical ones. We ensured for all three values to have an error below 10% with respect to the patient's value, where the error was calculated as $\frac{|reference_value - obtained_value|}{reference_value}$.

Patient 1	Measures	Computations	Errors
RVEDV	110ml	112ml	1.8%
RVESV	58ml	54.58ml	5.9%
RVEF	47%	51.26%	9.1%

Table 4.8: Comparison between the RV clinical measures and the values obtained for Patient 1.

The process we followed to obtain these results mainly consisted in the tuning of the elastances of the right ventricle, shown in Table 4.3: we decreased the value of E_a and increased the value of E_b in order to obtain an ejection fraction compatible with the one of Patient 1.

In [25] it is stated that a normal range of values for the RVEDV in a male is $163ml \pm 25ml$, with this interval representing the *mean* \pm *SD*. For the RVESV the range is instead $57ml \pm 15ml$. Regarding the RVEF, [25] refers to a normal range with $66 \pm 6\%$. So the patient's value for the RVESV was in range but the RVEDV and the RVEF were below the normal range.

Another important quantity is the Stroke volume which we measured as RVEDV-RVESV obtaining the value of $57.42ml$. According to [25], a normal stroke volume belongs to the range $106 \pm 17ml$. Therefore this value was very low for Patient 1 and, since it represents the volume of blood pumped out of the heart during the systole, a low stroke volume implies a lower flow of blood.

In Figure 4.4, on the top right, we can see the trend of the right ventricle volume in time during the last three heartbeats of the simulation. The X in green represents the RVEDV while the one in red is the RVESV. On the top left of the same figure there is the trend of the RV's pressure in time. The X in blue represents the right ventricular systolic pressure which takes the value of $27.17mmHg$. According to [54] a right ventricular systolic pressure greater than $35mmHg$ is considered pathological and a possible indicator of pulmonary hypertension (PH). According to Patient 1's clinical exams, no PH is diagnosed, therefore this result was coherent with the medical one.

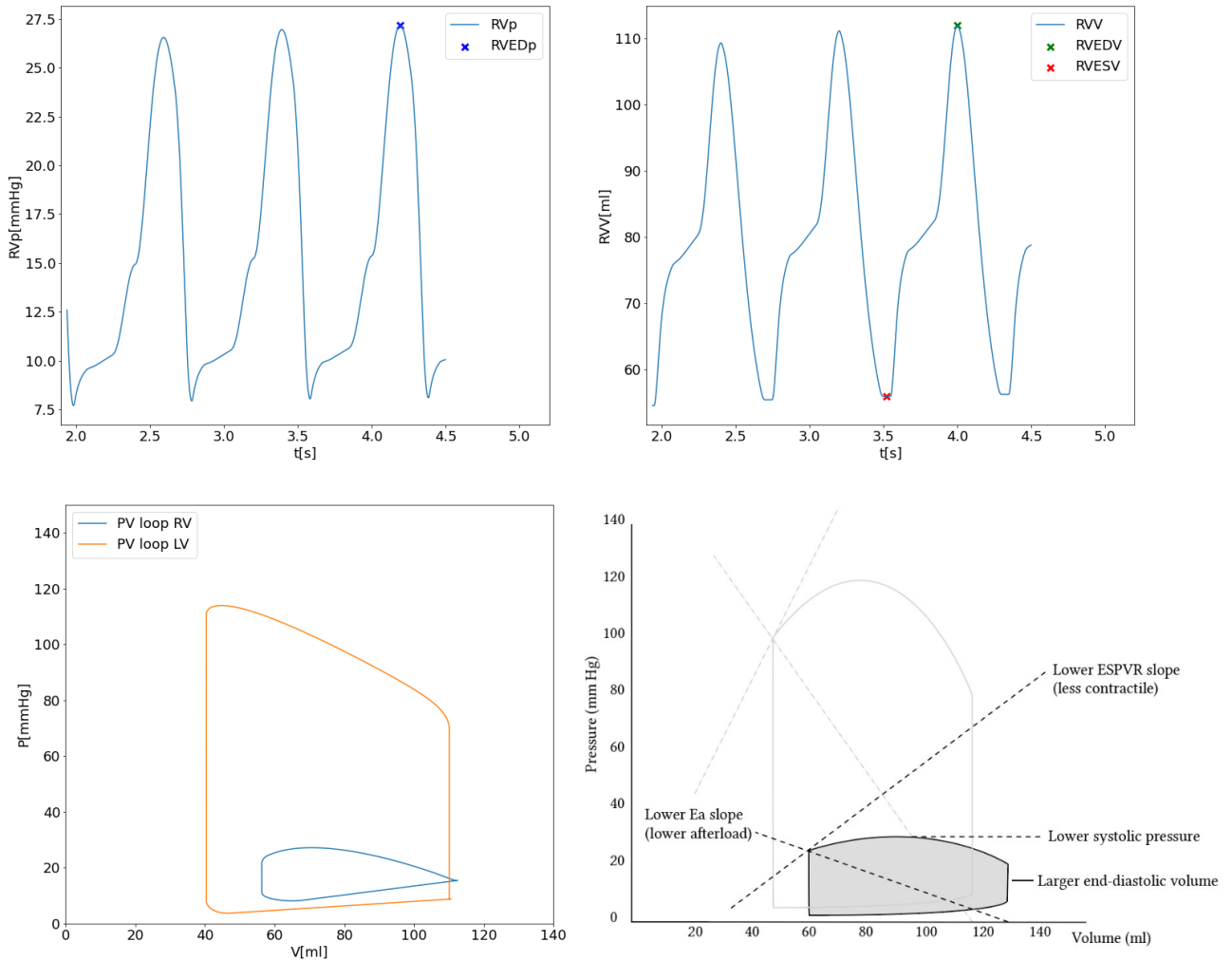


Figure 4.4: Right ventricle (RV) calibration on Patient 1, *Healthy* scenario. Top Left: RV Pressure variation. Top Right: RV Volume variation. Bottom Left: Obtained RV PV loop. Bottom Right: Normal RV PV loop [57].

Another important quantity we compared with the literature one is the right and left ventricle Pressure-Volume (PV) loop, which is a graph of each ventricle's pressure plotted with its relative volume in time. The comparison between the obtained PV loops, at the last simulated heartbeat, and the ones reported in [57] for a healthy person is shown respectively on the bottom left and right of Figure 4.4. The pressures seem to be quite in accordance with the ones of a healthy person. Instead it is clear that, while the end-systolic values of the volumes of both ventricles are quite similar to the healthy ones, the end-diastolic ones are lower.

$Q_{IN}, Q_{OUT,Right}, Q_{OUT,Left}$

During the calibration simulations we also monitored the average-in-space flow rates at the artificial boundaries, which are reported in Figure 4.5, on the left. In particular the last three heartbeats of the simulation are shown. From this graph it is clear how the flow at the inlet (Q_{IN}), which is the biggest one, divides itself at the bifurcation in a non symmetrical way ($Q_{OUT,Right}, Q_{OUT,Left}$). This result raised the question of whether this repartition was the most natural one, and we tried to answer to this question in section 4.3.4.

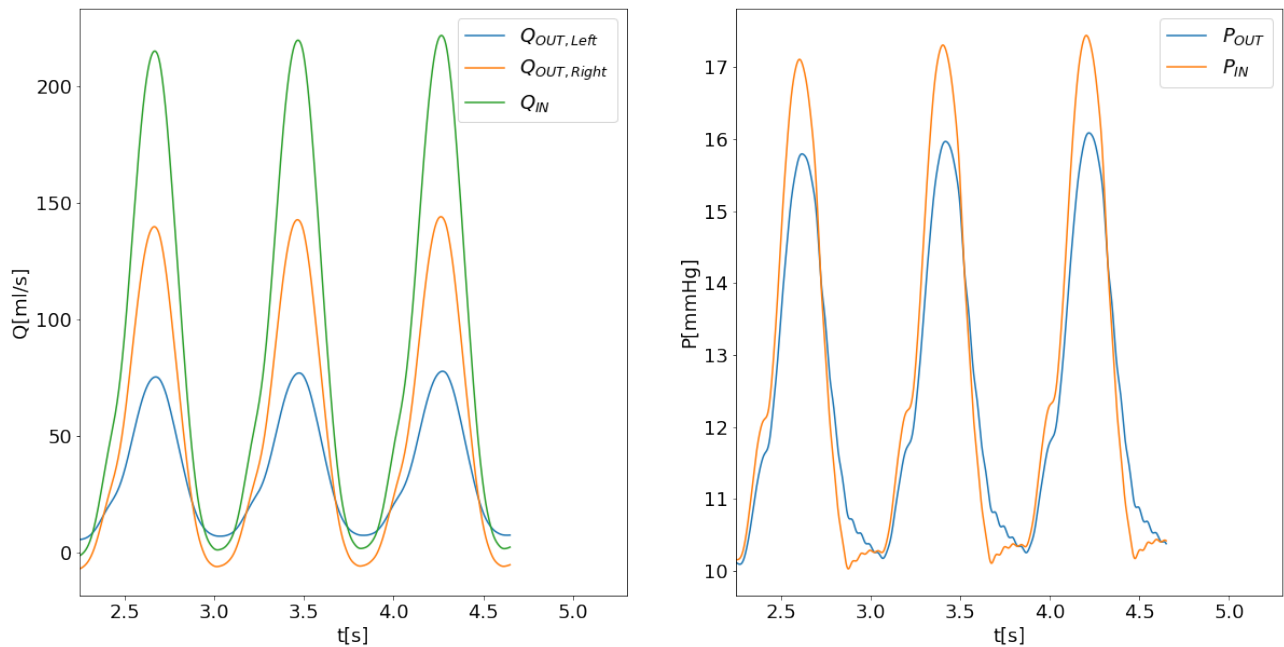


Figure 4.5: *Healthy* scenario of Patient 1. Flow rate (left) and pressure (right) at the artificial boundaries during the last three heartbeats of the simulations, in view of the calibration procedure.

We proceeded by calculating some averaged values in time and comparing them with the ones we found in literature for healthy conditions. We calculated first of all the mean flow through each of the three artificial boundaries and compared the obtained results with the ones of [48], as shown in Table 4.9. The mean flows were estimated from the last three heartbeats, shown on the left of Figure 4.5. We considered the mean flow at the inlet (Q_{IN}) as the mean flow in the main pulmonary artery (MPA) which is the pulmonary trunk before the bifurcation. Regarding the Right Pulmonary Artery (RPA) and the Left Pulmonary Artery (LPA), we compared the literature mean flows in the two branches with the mean flows calculated at the two outlets ($Q_{OUT,Right}, Q_{OUT,Left}$).

The results show a slightly lower flux compared to the normal one for the main artery and the left branch. This could be expected since the RVEDV of Patient 1 was lower than the norm. Indeed, if the ventricle dilates less, the stroke volume (the volume of blood pumped out of the heart during the systole) is lower and this causes the velocity of the blood exiting the ventricle to decrease too. The last row of Table 4.9 shows instead the percentage of blood reaching the right (R) and left (L) branch after the repartition at the main bifurcation. The obtained values seem to penalize more the flux entering the left branch, although the fact that more blood goes to the right side is respected.

mean flow rate [ml/s]	Literature [48]	Computations
MPA (Q_{IN})	95.30	87.63
RPA ($Q_{OUT,Right}$)	52.51	52.79
LPA ($Q_{OUT,Left}$)	42.79	34.84
Repartition (R-L) %	55-45	60-40

Table 4.9: Calibration on Patient 1, *Healthy* scenario. Comparison between the obtained flow rates and the literature ones [48].

P_{IN} , $P_{OUT,Right}$, $P_{OUT,Left}$

Finally, we compared the mean and peak pressures at the three artificial boundaries. On the right of Figure 4.5 we report the trend of the pressure at these boundaries. For the first set of simulations, performed with Algorithm 1 (*Healthy, Pre* and *Post*) the left and right outlet pressures were the same. We once again computed the mean on the three heartbeats shown in Figure 4.5. The term $mPAP$ is the mean pressure in the pulmonary artery while $sPAP$ and $dPAP$ are, respectively, the systolic and diastolic values of the pressure in the artery. The results are shown in Table 4.10 and, in general, we can see a lower range of pressures if we compare the obtained values, particularly in the systolic phase, to the ones found in [22]. Regarding the mean pressure, in [54] it is stated that a normal $mPAP$ should be around 15mmHg, which confirms the ranges found in [22] and reported in the table. The lower values of pressures both in average and during the systole can be explained by the lower stroke volume reported in the clinical exams, since a decreased flux from the right ventricle causes lower pressures in the pulmonary artery. Concerning another possible indicator for PH, the typical threshold of $mPAP > 20mmHg$ [47] is respected.

The main parameters on which we focused when calibrating the pressure and flow rate were the RLC circuit components at the inlet and at the outlet of the 3D model, respectively in the dark green and light blue boxes of Figure 3.7. In particular, we verified that higher

resistances and lower capacities had the effect of decreasing the flow rate and increasing the pressure of the branch in question.

mean pressure [mmHg]	Literature range [22] for $P_{IN}, P_{OUT,Right}, P_{OUT,Left}$	P_{IN}	$P_{OUT,Right}, P_{OUT,Left}$
sPAP	28 ± 7	17.44	16.09
dPAP	10 ± 3	10.03	10.09
mPAP	18 ± 4	12.73	12.47

Table 4.10: Calibration on Patient 1, *Healthy* scenario. Comparison between the obtained pressures and the literature ones [22].

4.3.4. Specific calibration on the 0D quantities of Algorithm 2

Concerning Algorithm 2, we performed some further studies in order to appropriately set the parameters shown in Table 4.7 of two RLC circuits at the outlets of the 3D model, in the light and dark blue boxes of Figure 3.9. In particular, we focused on the resistances $R_{OUT,Right}$ and $R_{OUT,Left}$.

4.3.4.1. On the imposition of the outlet resistances

As anticipated in section 3.5.2.3, while for the *-Murray* simulations we had to proceed by manually tuning the resistances $R_{OUT,Right}$ and $R_{OUT,Left}$ in order to obtain Murray's flow repartition, the flow repartition obtained by imposing the resistances calculated with the formula in (3.41) was very similar to the repartition predicted by the Chnafa law in (3.45), for both patients. We therefore avoided the tuning procedure of the resistances in this case and adopted the resistance formula for the *-Splitting* simulations.

Table 4.11 shows the percentage of flow entering the right (R) and left (L) pulmonary branches in the *-Splitting* simulations of both patients. These values were calculated by computing the mean flows at the two outlets during the last three simulated heartbeats. The first three columns show the results obtained by imposing the resistance values calculated with the formula in (3.41) in the three *Splitting* simulations, the last column shows instead the flow repartition predicted by the Chnafa law.

Regarding Patient 1, in all three simulations (first three columns) the flow seems to split itself so that approximately two thirds of it enters the right branch and one third enters the left one. This repartition is very close in all cases to the one predicted by the Chnafa law in (3.45), shown in the last column.

Regarding Patient 2, a similar analysis can be performed. The flow repartition for this patient seems to be more pronounced in all the simulations, with more than three quarters

of the flow entering the right pulmonary artery. Once again this results are quite coherent with the prediction performed with the Chnafa law (3.45) shown in the last column.

Flow repartition (R - L) in %	Healthy-Splitting simulation	Pre-Splitting simulation	Post-Splitting simulation	Estimate of (3.41)
Patient 1	66 - 34	66 - 34	67 - 33	67 - 33
Patient 2	76 - 24	76 - 24	76 - 24	75 - 25

Table 4.11: Comparison between the flow repartition of the Right (R) and Left (L) branch obtained by imposing the resistances according to (3.41) (first three columns) and the ones predicted by the Chnafa law in (3.45) (last column).

4.3.4.2. Study on choice of the area value of Patient 2's branches

The other study we performed was strictly linked to the first one and only involved Patient 2. Both the formulas to predict the flow repartition (3.42 and 3.44) and the one to directly calculate the outlet resistances (3.40) contained some terms that depended on the area or diameter of the two branches of the artery. A question that arose when applying these formulas regarded Patient 2's geometry. Indeed, unlike Patient 1, the two branches of this patient, and in particular the left one, significantly varied in dimension from the bifurcation point up to the outlets and thus the sections were not uniquely determined. For this reason, we evaluated different possibilities:

1. Considering the exact values of the diameters and areas at the outlets;
2. Considering the exact values of the diameters and areas at the bifurcation level;
3. Considering an intermediate value calculated as the mean among values taken at three different points along the branches.

In Figure 4.6, we can see how D_3 , which is the diameter at the outlet, is less than half of the diameter measured at the bifurcation level (D_1).

Table 4.12 shows the percentage of flow entering the right (R) and left (L) pulmonary branches in the *Post-Splitting* simulation of Patient 2 considering all three options (*Post-Splitting* column). We compared these values to the ones predicted by the Chnafa law in (3.45) to see if in one of these cases the repartition was coherent with the predicted one as for Patient 1 3.5.2.3. Regarding the second two rows of the table (Bifurcation values and Mean values) it is clear that the predicted values are not achieved. In particular, in the obtained results the flow repartition between the right and the left branches

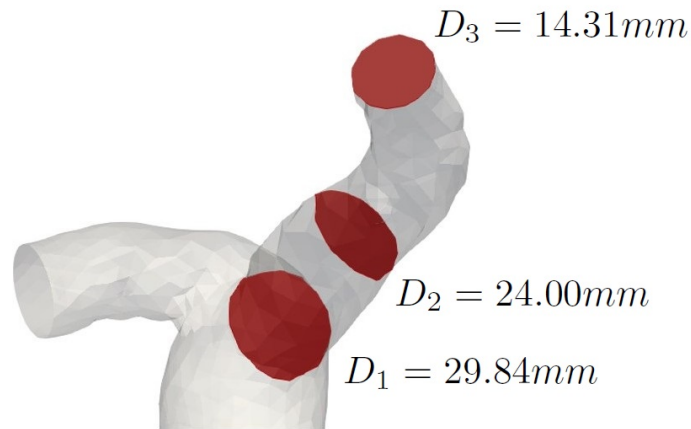


Figure 4.6: Diameter variation of the left branch of Patient 2's pulmonary artery.

seems to be more pronounced with respect to the one predicted. Concerning the first row (Outlet values), the predicted result was instead achieved. For this reason, our choice of the sections fell on the ones at the outlets, which corresponded to option 1, for all the *-Splitting* simulations of this patient. This choice is the one reported in Table 4.11 and it is equivalent to the assumption of the hypothesis that the higher pressure imposed by the smaller sections at the outlets of the branches are felt by the flow when it reaches the bifurcation.

R-L branches	Post-Splitting repartition in %	Repartition predicted by (3.45) in %	Diameters in mm
Outlet values	76-24	75-25	24.33-14.28
Bifurcation values	67-33	56-44	29.32-26.91
Mean values	71-29	60-40	27.55-22.16

Table 4.12: Comparison between the flow repartition of the two branches (R and L) of Patient 2 obtained in the *Post-splitting* simulations, the repartition estimated by the law in (3.45) and the diameters of the two branches considering different sections.

The last column of Table 4.12 shows the measured diameters in the three cases (at the bifurcation level, outlet level and calculated as a mean) for Patient 2. By comparing these values with the flow repartitions it is possible to notice a coherence between the outlet sections and the unbalance of the flow repartition between the two branches. Indeed, the two branches of Patient 2, at the bifurcation level (second row), have a similar diameter,

and therefore the flow repartition obtained by imposing a pressure depending on these is more balanced. Considering instead the outlet diameters (first row of both tables), which are very different, leads to a repartition in which more than a quarter of the flow enters the right branch. Finally, if we adopt a mean value of the diameters (third row), we obtain a repartition that is milder than the previous one but more pronounced than the one obtained with the bifurcation diameters.

5 | Numerical Results

In this chapter we detail the numerical results of all the simulations. Section 5.1 is dedicated to the simulations implemented with Algorithm 1: *Healthy*, *Pre* and *Post* simulations, described in section 3.4.4, focusing on the effectiveness of the PVR operation. In section 5.2 we instead assess the importance of assigning the correct boundary conditions at the outlets of the 3D model exploiting Algorithm 2, described in section 3.5.1. We employed 2D graphs of mean quantities of interest and 3D visualizations obtained with Paraview at different instants of the velocity, pressure and WSS.

5.1. Comparison between the *Healthy*, *Pre* and *Post* simulations

Once ensured that the quantities described in section 4.3 were accurate enough to describe the *Healthy* simulation of the two patients, we proceeded by analysing the results of the three simulations of Algorithm 1 using 3D visualizations in time thanks to Paraview. We performed the first three simulations (*Healthy*, *Pre* and *Post* simulations) applying Algorithm 1 and compared different quantities, in particular the velocity and pressure fields and the WSS.

Among the six heartbeats we had simulated, we decided to analyse these quantities at three instants belonging to the last heartbeat, in the interval of time $4.0 - 4.8s$, in order to ensure the stability of the solution. As reference for the values of the velocity in the artery, we considered the velocity at the inlet (Q_{IN}), being the interface quantity assigned by the 0D model. For the same reason, we considered as reference for the pressure the one at the two outlets (P_{OUT}).

Figure 5.1 shows, respectively on the left and right, the inlet velocity profile and the outlet pressure profile during the last heartbeat in the *Healthy* simulation of Patient 1. The points marked by the blue, green and red crosses represent, respectively, the beginning of the systole ($t = 4.1s$), the systolic peak ($t = 4.45s$) and the diastolic phase ($t = 4.45s$). These instants were chosen since they are representative of the whole heartbeat.

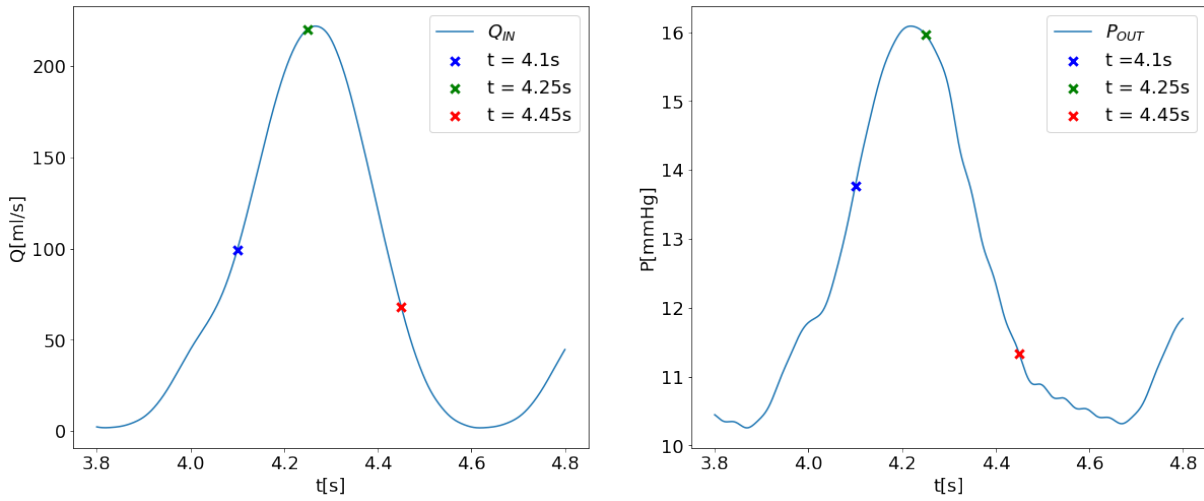


Figure 5.1: Patient 1, *Healthy* simulation. Left: Inlet flow rate. Right: Outlet pressure field.

5.1.1. Velocity field

Concerning the velocity field, we compared for both patients the three simulations *Healthy*, *Pre* and *Post* at the three cited relevant instants of time. In Figure 5.2 we present the result of this comparison. The first column shows for both patients the velocity profile respectively at the beginning of the systole (row 1 and 2), at the systolic peak (row 3 and 4) and during the diastole (rows 5 and 6) in the *Healthy* simulation. The central column shows instead the *Pre* simulation at the same instants and the last column is the *Post* simulation. To obtain these visualizations we made use of the *surface LIC* visualization of Paraview.

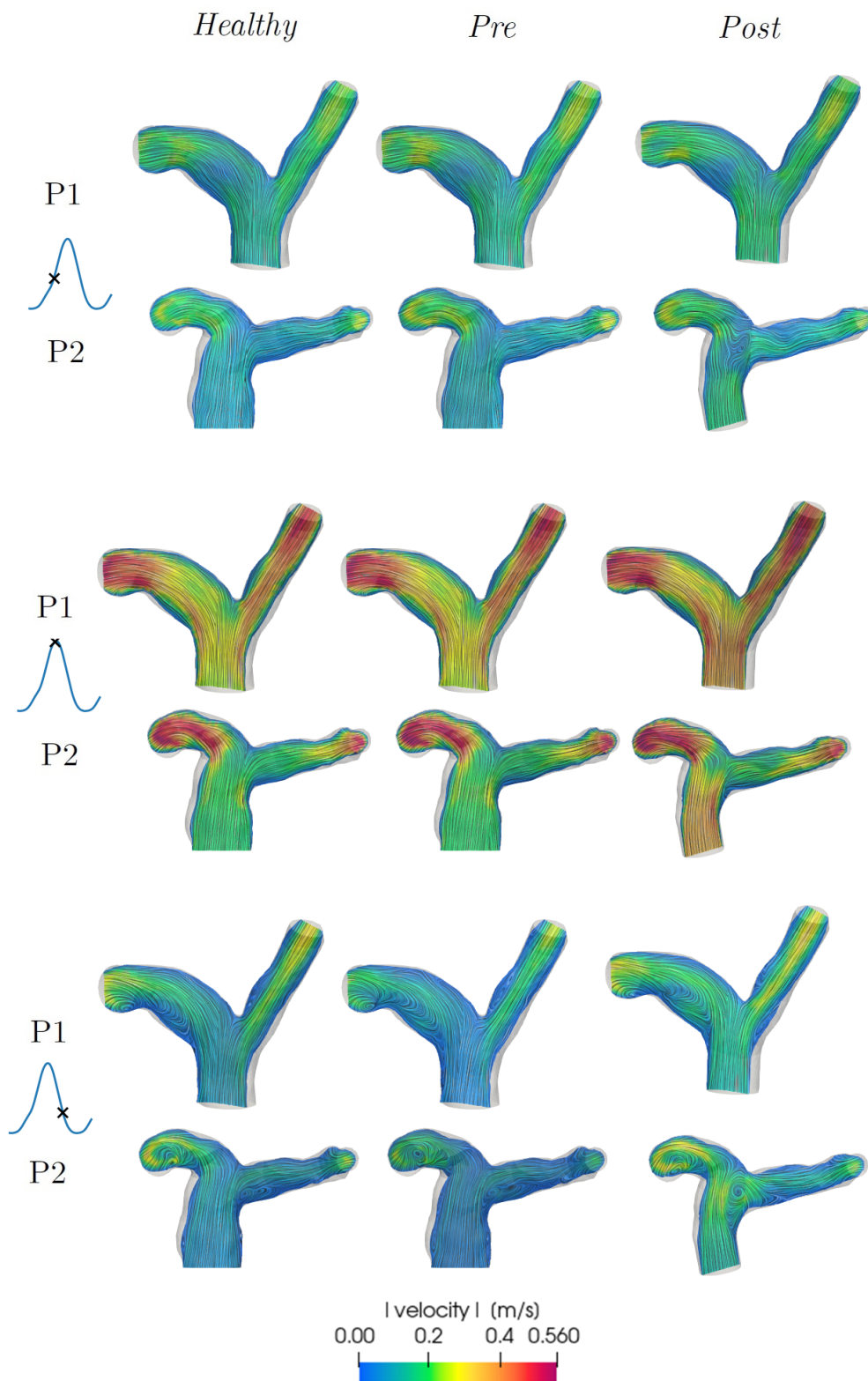


Figure 5.2: Velocity field in the *Healthy* (left), *Pre* (center) and *Post* (right) simulations for both patients at three significant heartbeat instants.

From this global view of the three simulations in time we can notice that in the *Post* simulation of both patients (right column) the velocity at the inflow seems to be slightly greater, especially at the systolic peak. This can be explained by the presence of the prosthetic stent which narrows the inflow zone of the artery of the patients. This phenomenon is more evident for Patient 2 since the geometry in the *Post* simulation of this patient has a greater difference from the one of the *Healthy/Pre* simulations. Concerning the instant of peak of the velocity (central rows), we can see from the colors how the velocity field is slightly higher for the first patient compared to the second one. This could be due to the more regular geometry of the first patient which allows the blood to be more free. Finally, we can notice how in general the biggest differences among the simulations can be seen, as expected, during the diastolic phase of the velocity (last two rows). In fact, in this phase the pulmonary valve becomes more relevant by closing. We can see how for Patient 1 the velocity in the *Post* configuration is similar to the one in the *Healthy* one but with slightly higher values; this is actually a positive result since, as said, the *Healthy* simulation corresponds to the best simulation with the native geometry of the patient, however the velocity for this patient, estimated through the medical exams, was quite low in mean with respect to a truly healthy person.

Regarding Patient 2, the *Post* simulation highlights the formation of a vortex toward the left branch of the pulmonary artery. As we noticed during the reconstruction of the stent (section 2.6.2), the valve for this patient was not positioned perpendicularly to the artery, therefore this deformed geometry could explain the formation of the vortices. In fact, if we recall Figure 2.9, we can see how the stent for Patient 2 seems to channel the blood toward the right branch of the artery and this could cause a recirculation toward the left one, making it more challenging for the blood to reach the outlet of this branch.

We then decided to further analyse this matter by focusing only on the diastolic phase of the velocity and by changing the type of visualization in order to see more clearly the streamlines. In Figure 5.3 we report the results of the velocity streamlines obtained with the *glyph* filter of Paraview. We chose to focus on specific zones of interest which consisted respectively in the right branch for Patient 1 (first row) and in the left one for Patient 2 (second row). The results are presented for each of the three simulations with a saturated scale in order to better highlight the differences.

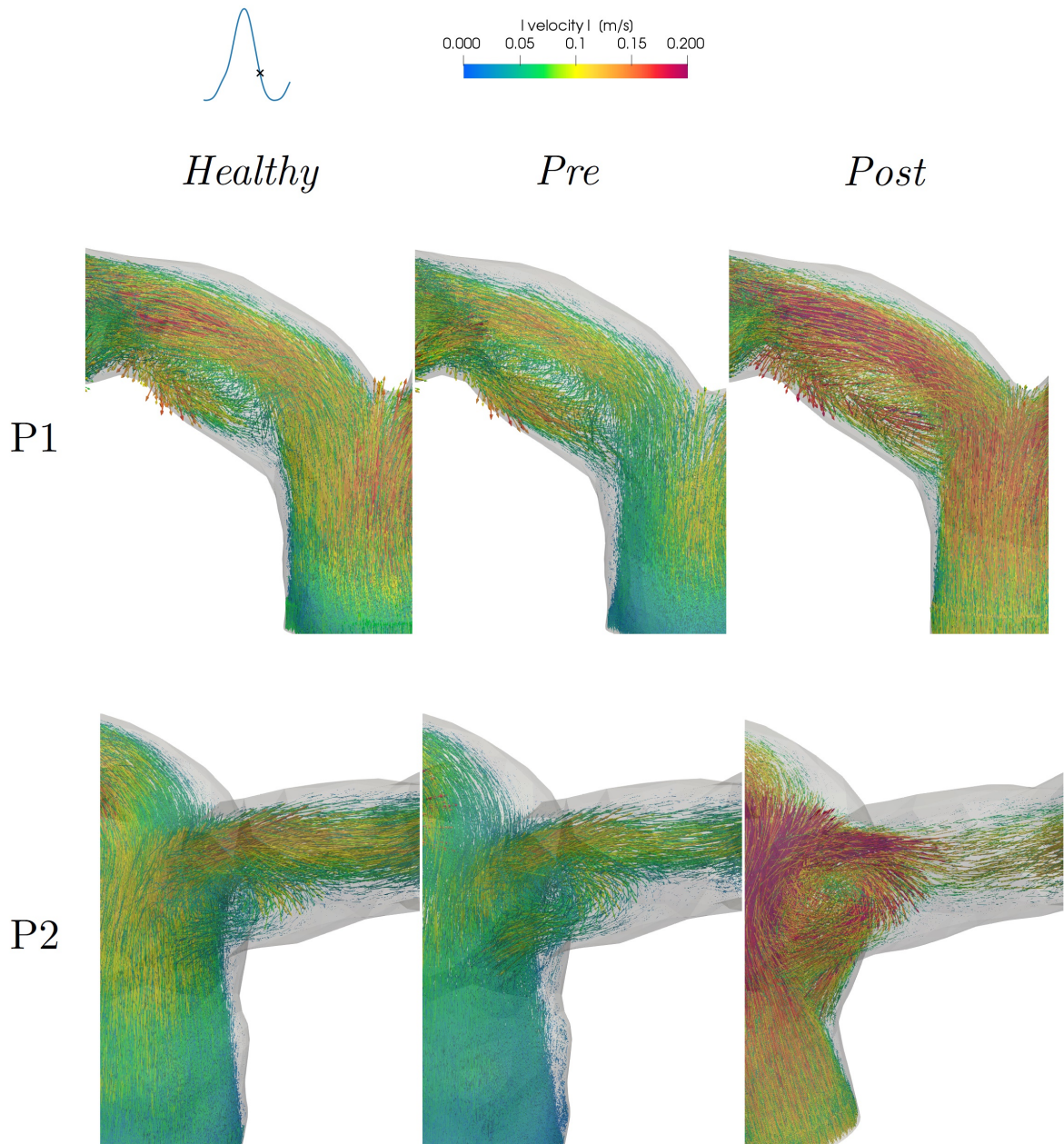


Figure 5.3: Velocity field during the diastolic phase in the *Healthy* (left), *Pre* (center) and *Post* (right) simulations. Top: Patient 1's right branch. Bottom: Patient 2's left branch.

From Figure 5.3 the increased velocity and recirculation due to the stent addition in the *Post* simulation are evident for both patients. Regarding Patient 1, a recirculation region can be seen in the right branch in all three simulations. The main difference between the *Healthy* and *Pre* simulations is that the blood seems to recirculate slightly more in the *Pre* operative condition reaching less effectively the outlet of the right branch. In the *Post*

simulation, instead, the velocity has as said a greater magnitude and as in the *Healthy* simulation, the recirculation does not seem to predominate over the blood reaching the right outlet.

Regarding Patient 2, a recirculation region can be seen instead in the left branch, in all three simulations. Once again this phenomenon predominates a bit more in the *Pre* simulation with respect to the *Healthy* simulation, while, regarding the *Post* simulation it seems that fewer lines of flow manage to reach the left branch and are instead channeled toward the right one. Moreover, the recirculation region of the *Post* simulation is both bigger and slightly translated with respect to the other two cases. In particular, it seems to be closer to the main pulmonary trunk, right behind the prosthetic valve.

The formation of vortexes is in general an interesting aspect from a medical point of view. Indeed, recirculation regions can lead to degradation of the arterial walls [44]. Moreover, high flow recirculation can have a significant contribution to the generation of the turbulent fluctuations in the post-stenosis regions [35]. Although there are no stenosis in these patients, the valve stent does alter the flow, particularly in Patient 2, so the recirculation phenomenon could cause a transition to a turbulent flow. Indeed, although we have modeled blood as a homogeneous fluid, its nature is actually that of a suspension where cell-cell interactions mediated by the plasma during turbulent velocity fluctuations could give rise to viscous shear stresses[2]. The transition to turbulence in a suspension may cause or accelerate the onset of atherosclerotic lesions by causing a critical injury in the wall resulting from areas of local stasis and/or jet-stream impingement upon the arterial wall [53].

5.1.2. Pressure field

Another 3D field that we examined for all three simulations of both patients was the pressure one. In Figure 5.4 we report, as for the velocity, the pressure profiles at significant instants for both patients. In particular, the first column shows the pressure respectively at the beginning of the systole (row 1 and 2), at the systolic peak (row 3 and 4) and during the diastole (rows 5 and 6) in the *Healthy* simulation. The central column shows instead the *Pre* simulation in the same instants and the last column shows the *Post* simulation.

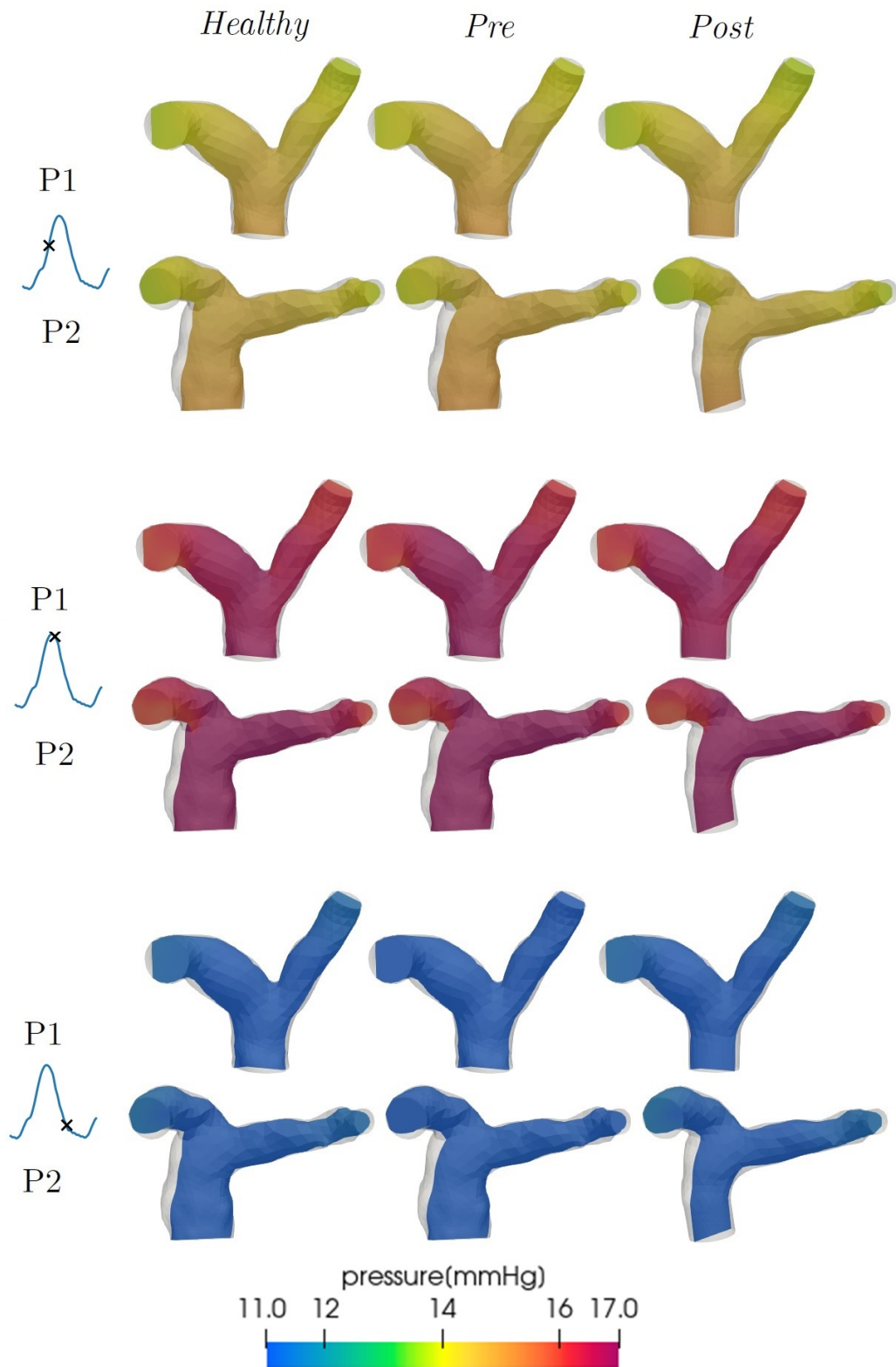


Figure 5.4: Pressure field in the *Healthy* (left), *Pre* (center) and *Post* (right) simulations for both patients at three significant heartbeat instants.

From Figure 5.4 it is clear that the biggest difference, regarding the pressure in the artery of both patients, is from a temporal point of view with respect to a spatial one. Indeed, by looking at this figure in time (from top to bottom) we can see that the pressure values of all simulations are very close to each other at each instant and the real difference can be noticed only when comparing different moments of the heartbeat. In particular, for both patients along the whole artery the values of the pressure during the beginning of the systole (top two rows) are in between the peak values (central rows) and the diastolic ones (bottom rows). This is in general coherent with what we anticipated since the pressure is expected to grow during the systolic phase, as the contraction occurs, and then to decrease during the diastole. The fact that the pressure values of the whole domain are concentrated in a small range at each instant can be explained with the fact that the right side of the heart does not present pressure jumps as big as the ones in the left side. Moreover, as said, the peak values of pressure of Patient 1 were not expected to be very high because of the medical data we had analysed. From the first four rows of the figure, we can notice how the pressure seems to assume slightly lower values toward the outlet regions. This is coherent with the fact that these regions have a smaller diameter with respect to the rest of the artery and the velocity of the flow is higher.

Since the phase of interest of the heartbeat was mainly the diastolic one, we decided to analyse further the pressure in this phase. As for the velocity, we chose a more saturated scale in order to better highlight the differences among the simulations. In Figure 5.3 we can see the results of this operation. By looking at this figure, the trend of the pressure seems to be the same in all cases: lower at the inlet and increasing toward the two outlets. This trend is opposite to the one of the systolic phase and this is coherent with the fact that the velocity during the diastole slows down. On the other hand, the values assumed by the pressure in the three simulations are not the same, although very close. Indeed, in the *Pre* simulation the pressure seems to assume slightly lower values with respect to the *Healthy* and *Post* simulations. Therefore the pulmonary valve replacement operation seems to restore the higher pressures of the *Healthy* simulation. Regarding Patient 2, a small zone of lower pressure can be seen in the *Post* simulation. This is may be connected with the vortex cited before since the pressure drop behind the prosthetic stent may cause a backflow. In general it seems that the pressure is altered much less by the presence of absence of the valve with respect to the flow rate.

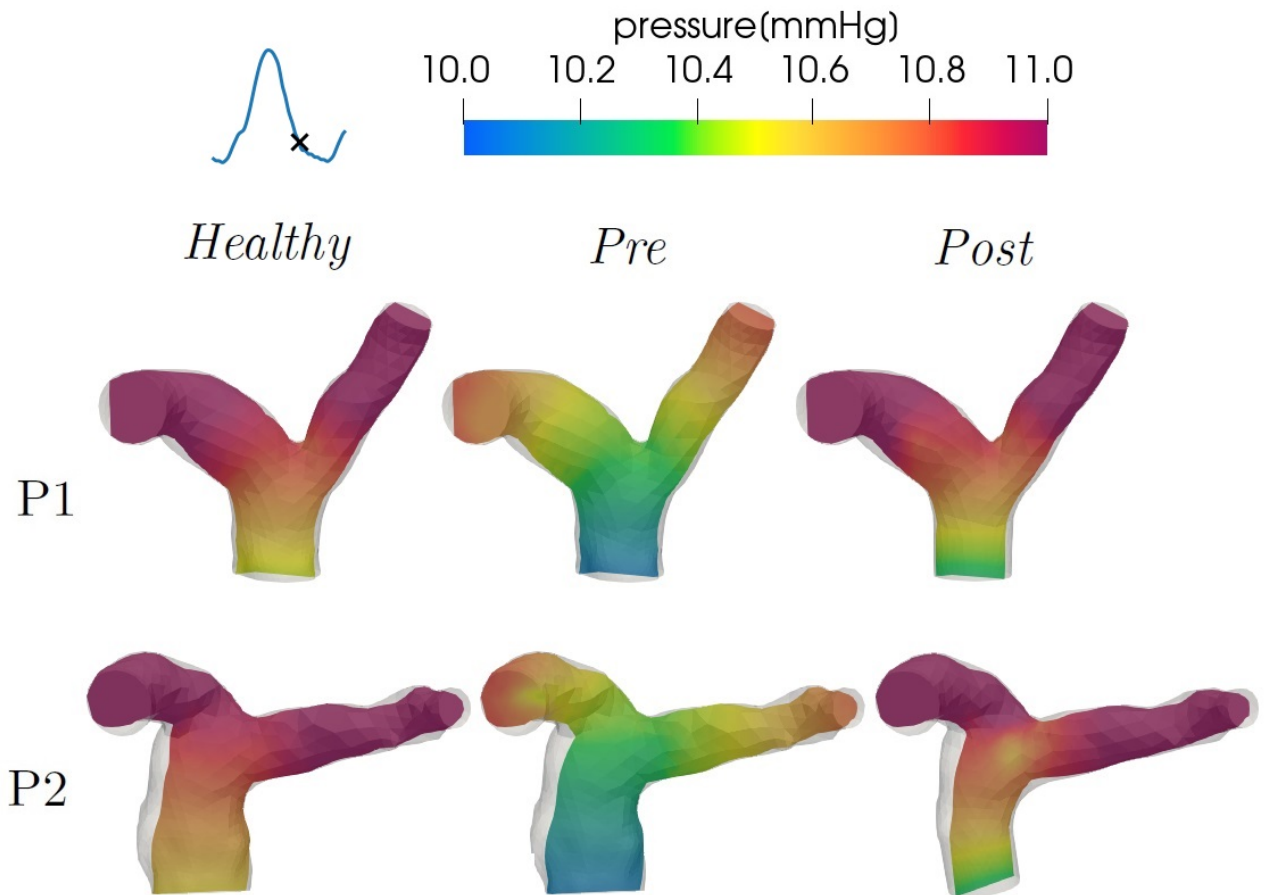


Figure 5.5: Pressure field during the diastolic phase in the *Healthy* (left), *Pre* (center) and *Post* (right) simulations for Patient 1 (top) and Patient 2 (bottom).

5.1.3. Wall Shear Stress analysis

Another important quantity that we monitored is the WSS. We made use of the software Paraview in order to visualize the results regarding this quantity for both patients at the systolic peak. Figure 5.6 shows this comparison.

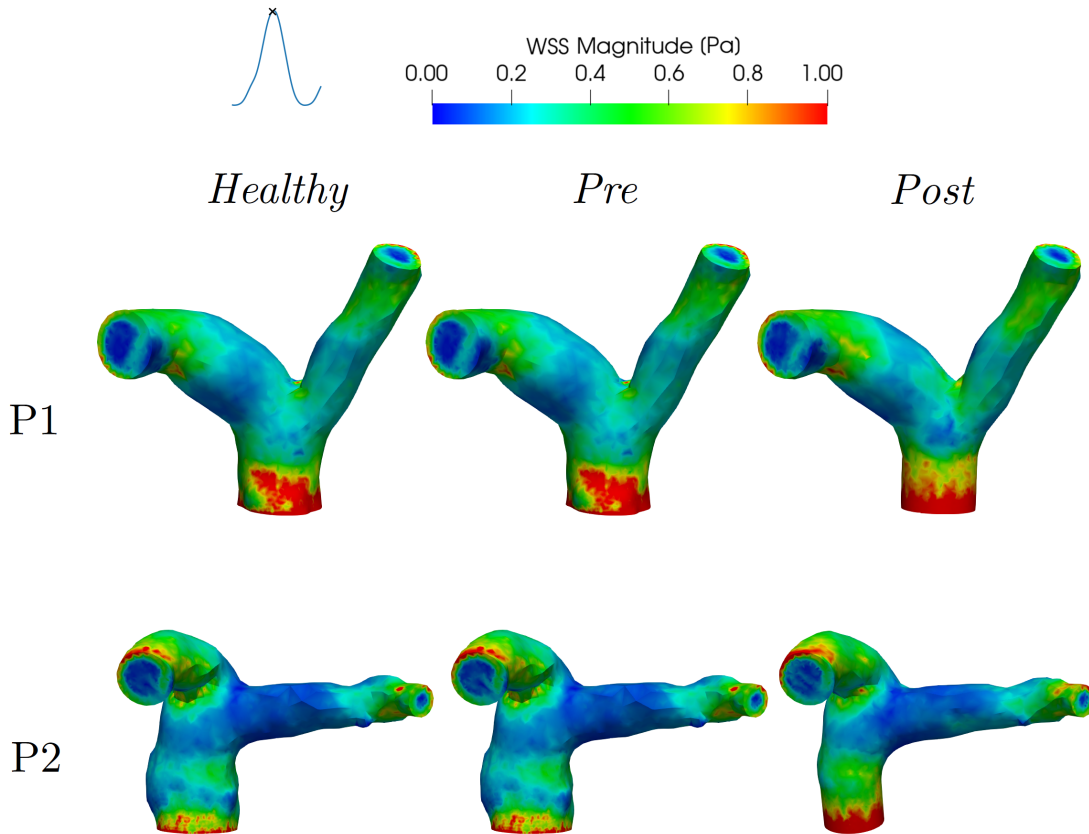


Figure 5.6: WSS in the *Healthy* (left), *Pre* (center) and *Post* (right) simulations for both patients at the peak of the systole.

We report specifically the moment of the heartbeat where the flow is at its maximum since higher values of WSS can be observed in this instant. Regarding the areas where the WSS is higher, we can notice the artificial boundaries and in particular the inflow zone. Since the WSS is defined as the magnitude of the tangential component of the velocity gradient, it can be expected that at the inlet, where the velocity profile is assigned as flat, the WSS assumes higher values. Other regions where the WSS is high are the areas where the geometries of the arteries are more tortuous. We can notice a larger WSS, for example, in the right branches of the arteries and in particular in the one of Patient 2.

Regarding the specific values of the WSS, we compared them to the average ones in

healthy conditions. In particular, [49] defines the threshold for the maximum WSS in healthy conditions as around $2 - 2.4Pa$. Our results, during the systolic peak were quite coherent with this definition, belonging in mean to the range $[0 - 2.5Pa]$.

Comparing the different scenarios at the peak of the systole, no meaningful differences can be noticed. We therefore decided to analyse the *TAWSS*, which is the Time Averaged WSS of the last heartbeat of the simulations, employing a more saturated scale in order to see the possible effects of the absence of the valve and of the implantation of the prosthetic stent. Figure 5.7 shows the results of this study. From this figure we can see how in the *Post* simulation, the TAWSS assumes slightly higher values in the inflow region. This is coherent both with the results seen for the velocity, which also increases in this simulation, and with the post-operative configuration, since, with the prosthetic stent implanted, the geometry of the patients' arteries is narrower. In general we notice a slightly lower TAWSS for Patient 2 compared to Patient 1. A low TAWSS indicates a low mean local velocity and therefore long residence times of the blood near the vessel boundaries [20]. The low values of TAWSS in the left branch of Patient 2 suggest an inclination to recirculation phenomena and stagnation of the blood. These results are coherent with the ones seen for the velocity profile in section 5.1.1.

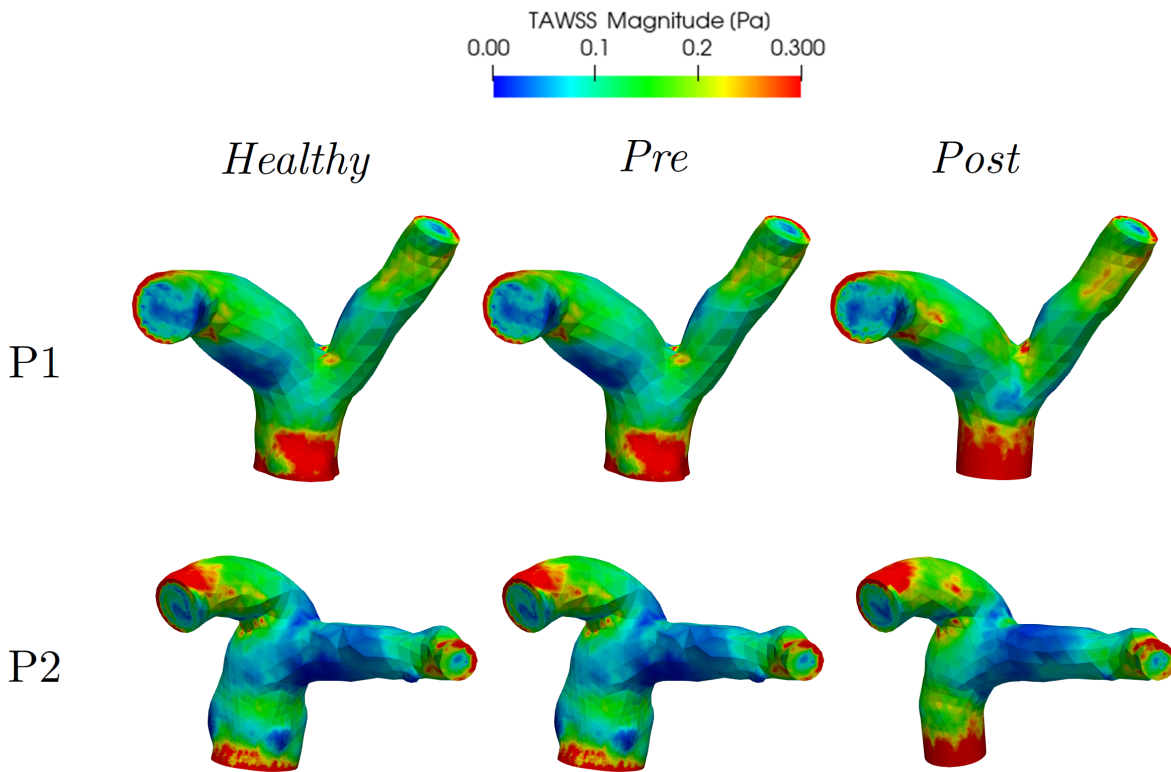


Figure 5.7: TAWSS of the last simulated heartbeat in the *Healthy* (left), *Pre* (center) and *Post* (right) simulations of both patients.

5.1.4. Analysis of 0D quantities of interest

We then decided to analyse further some quantities of the 0D model. We first of all compared the flow passing through the pulmonary valve (diode) placed in the 0D model. In Figure 5.8, on the left, we can see the trend of this quantity during the last simulated heartbeat for all the three simulations of Patient 1. On the right of the same figure we show instead the trend of the pressure in the pulmonary trunk, in the 0D model. The effect of the absence of the pulmonary valve in the *Pre* simulation (in yellow) is clear from the formation of a very large backflow during the diastole, where the flow, at its minimum, is around 50% in absolute value of the maximum flow reached during the systole. According to medical indications, a pulmonary regurgitation of 47% is considered as severe, so this backflow effect would be an indication for surgery. The effect of the backflow can be seen also from the graph of the pressure on the right of Figure 5.8, since there is a greater pressure gradient in time during the diastole of the *Pre* simulation (in yellow). Moreover, from these two graphs, if we analyse the *Healthy* and the *Post* lines (which are respectively in blue and green), we can see that, regardless of the different geometry

given by the addition of the stent in the *Post* simulation, the insertion of a functioning valve restores a flux very close to a healthy condition.

The results for Patient 2 are very similar to the ones for Patient 1 although the backflow effect is slightly larger.

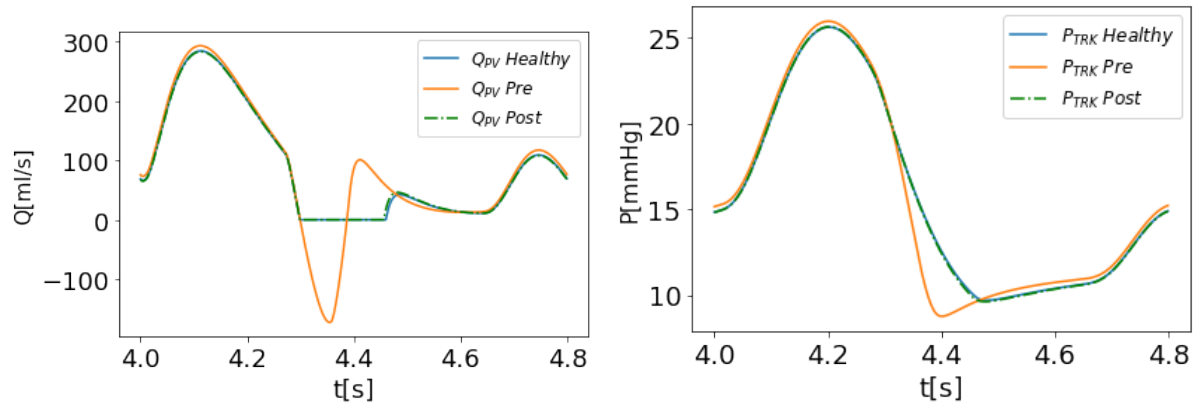


Figure 5.8: Patient 1. Left: Comparison between the flow at the pulmonary valve in the 0D model (Q_{PV}) in the three simulations. Right: Comparison between the pressure at the pulmonary valve in the 0D model (p_{TRK}) in the three simulations.

Having noticed this large backflow in the Pre operative simulation, we investigated more closely its effects on the right ventricle. In particular, Figure 5.9 shows a comparison between the PV loops of the RV in the three simulations of Patient 1. We can see how the zone of isovolumetric relaxation of the ventricle (the vertical blue and green lines on the left) is no longer present in the Pre simulation (in yellow). Indeed, without the pulmonary valve closing, as the ventricle relaxes, its volume increases instead of staying constant. This effect is one of the typical consequences, from a medical point of view, of PV regurgitation: an overload on the right ventricle which causes a bigger dilatation. Once again this effect seems to disappear when the prosthetic valve is implanted in the Post simulation (in green) and the PV loop of the right ventricle is similar to the one of the Healthy simulation (in blue).

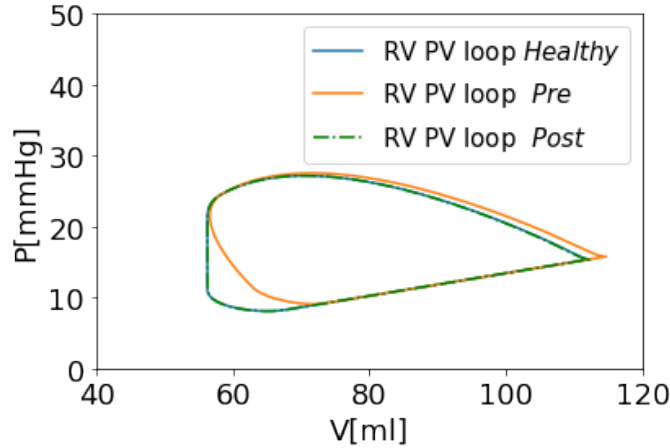


Figure 5.9: Patient 1. Comparison between the PV loops obtained by the 0D model in the 3 simulations.

5.2. On the importance of differentiating the outlet boundary conditions

In this section we analyse the results obtained with Algorithm 2 and compare them to the ones just described in order to assess the importance of differentiating the two outlet boundary conditions of the 3D model.

5.2.1. Study on the flow repartition in the three *Healthy* scenarios

Since one of our goals was to analyse the variation of the flow repartition induced by the imposition of different boundary conditions at the 3D outlets, first of all we decided to compare the flows in the left and right branches for the three *Healthy* scenarios of both patients from the results of the 0D part of the model. Figure 5.10 shows the results of this comparison during the three last heartbeats we simulated. We can notice that, in all three simulations and for both patients, the quantity of flow entering the right branch is bigger with respect to the one entering the left one. Moreover, the importance of the patient-specificity of the simulations is confirmed by the fact that, if we refer to the *Healthy* simulation, where the outlet resistances are equal to each other, the flow splits of the two patients are not the same. The mean values of the flow rates in the two branches and the respective proportions are shown in Table 5.1 for Patient 1 and Patient 2. By looking at the column *Healthy* of the table, it is clear that even with a similar total flow (MPA), and equivalent resistance values at the outlets, the flow split between

the right and left pulmonary arteries (RPA and LPA) of Patient 2 is more unbalanced (60-40 against 74-26). This phenomenon can be observed also in the *Healthy-Murray* and *Healthy-Splitting* simulations.

Regarding these last two simulations, in yellow and green in Figure 5.10, we can also notice that in the *Healthy-Murray* simulation the flow in the right branch is the highest during the systole, while in the left branch a backflow occurs during the diastolic phase. The same phenomenon occurs also if we look at the green line, although it is less evident. If we refer to the *Repartition* rows of Table 5.1, we have a confirmation of this result. Indeed, for each patient, the most unbalanced result is the *Healthy-Murray* simulation, while the *Healthy-Splitting* simulation lies in between the other two. This final result was expected, indeed, if we refer to the resistance values described in Table 4.7, it is clear that a bigger difference among the resistances entails a bigger difference among the flows rates of the branches too.

	Mean flux	Healthy	Healthy-Murray	Healthy-Splitting
Patient 1	MPA [<i>ml/s</i>]	81.72	84.10	83.59
	RPA [<i>ml/s</i>]	32.64	62.60	55.45
	LPA [<i>ml/s</i>]	49.08	21.49	28.15
	Repartition (R-L) %	60-40	74-26	66-34
Patient 2	MPA [<i>ml/s</i>]	81.38	84.19	83.61
	RPA [<i>ml/s</i>]	59.84	69.25	63.30
	LPA [<i>ml/s</i>]	21.58	14.97	20.35
	Repartition (R-L) %	74-26	82-18	76-24

Table 5.1: Mean flow in the main, right and left pulmonary arteries (MPA, RPA and LPA respectively) and flow repartition at the bifurcation of Patient 1 and Patient 2 in the Healthy scenarios.

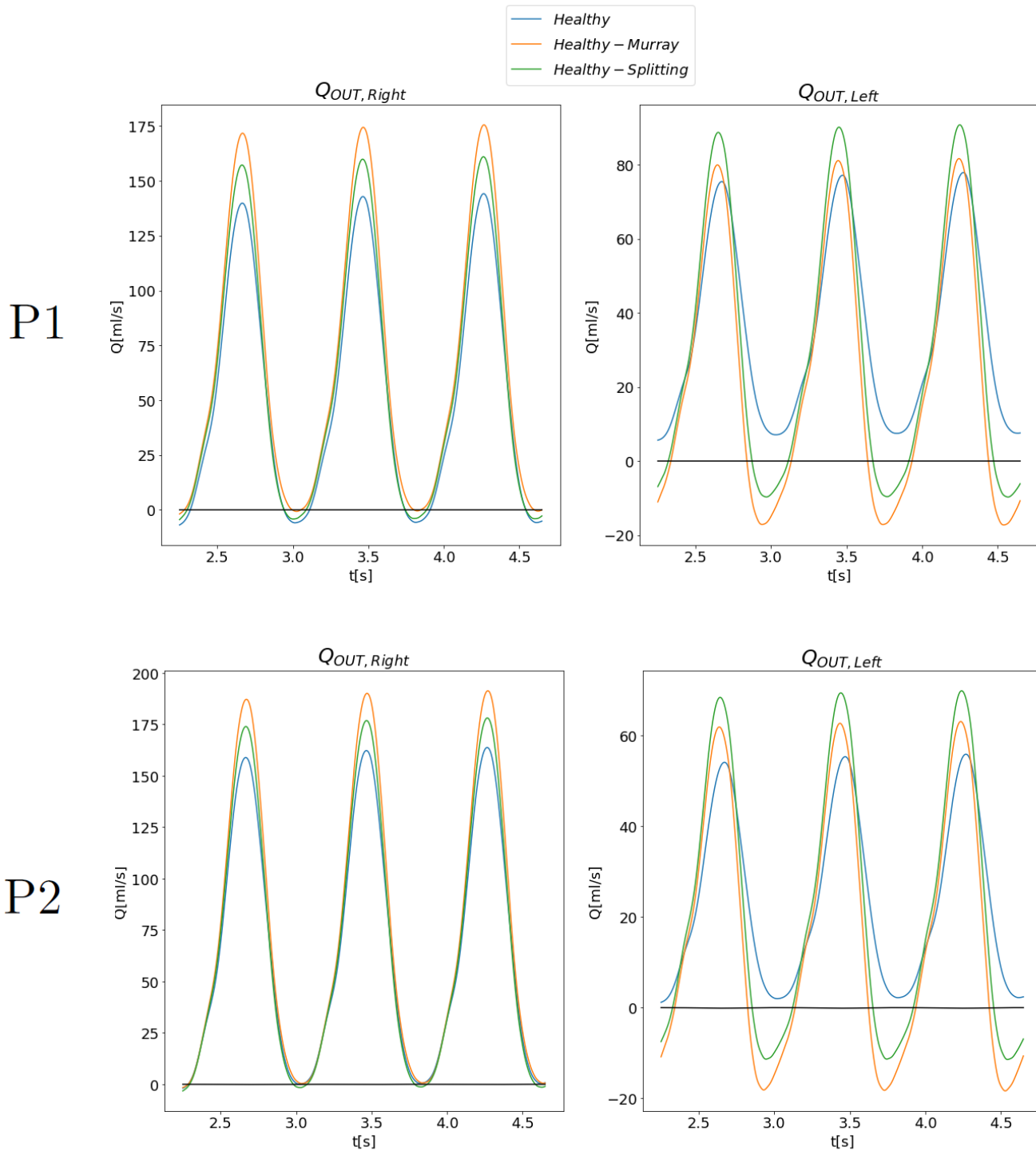


Figure 5.10: Comparison among the flow rates in the two branches of the artery in the *Healthy*, *Healthy-Murray* and *Healthy-Splitting* simulations during the last three heartbeats of Patient 1 (top) and Patient 2.

5.2.2. Study on the outlet pressures in the three *Healthy* scenarios

We then performed a study on the pressures at the outflows to verify the actual pressures imposed at the two outlets in the *Healthy-Murray* and *Healthy-Splitting* simulations of the two patients. In Figure 5.11 we report the pressure trends during the last three heartbeats on the right and left outlets of the two patients in the three *Healthy* scenarios. By looking at the graphs it is clear how the green and yellow lines have a lower peak with respect to the blue one for both patients. This is also verified by the values reported in Table 5.2 which shows the mean values in time of the two outlet pressures in the *Healthy*, *Healthy-Murray* and *Healthy-Splitting* simulations, respectively, for Patient 1 at the top and for Patient 2 at the bottom. The rows named *Difference* shows, for both patients, the pressure difference between the two outlets and we can notice how, while in the first column of the two tables (*Healthy*) this difference is 0, the other two columns (*Healthy-Murray* and *Healthy-Splitting*) show the different imposition of the pressures. This can be also noticed by the trends of the green and yellow lines of Figure 5.11, which are different if we compare the two branches (left and right). Finally, from the rows named *Difference* of Table 5.2, we can also see how the pressure difference between the branches is higher for the *Healthy-Murray* simulation of Patient 1 with respect to the corresponding simulation of Patient 2 (0.19 against 0.12). Once again, this confirms the importance of the patient-specificity of the geometry since a bigger pressure difference does not imply a bigger difference in the flow proportion of the two patients. Patient 2, indeed, as we saw in section 5.2.1 had a bigger difference regarding the flow split in every simulation.

	Mean pressure	Healthy	Healthy-Murray	Healthy-Splitting
Patient 1	RPA [mmHg]	12.47	11.08	11.35
	LPA [mmHg]	12.47	11.27	11.39
	Difference [mmHg]	0	0.19	0.04
Patient 2	RPA [mmHg]	12.47	11.08	11.37
	LPA [mmHg]	12.47	11.20	11.32
	Difference [mmHg]	0	0.12	0.05

Table 5.2: Mean pressures assigned at the right and left outlets (RPA and LPA) of Patient 1 and Patient 2 in the three *Healthy* scenarios.

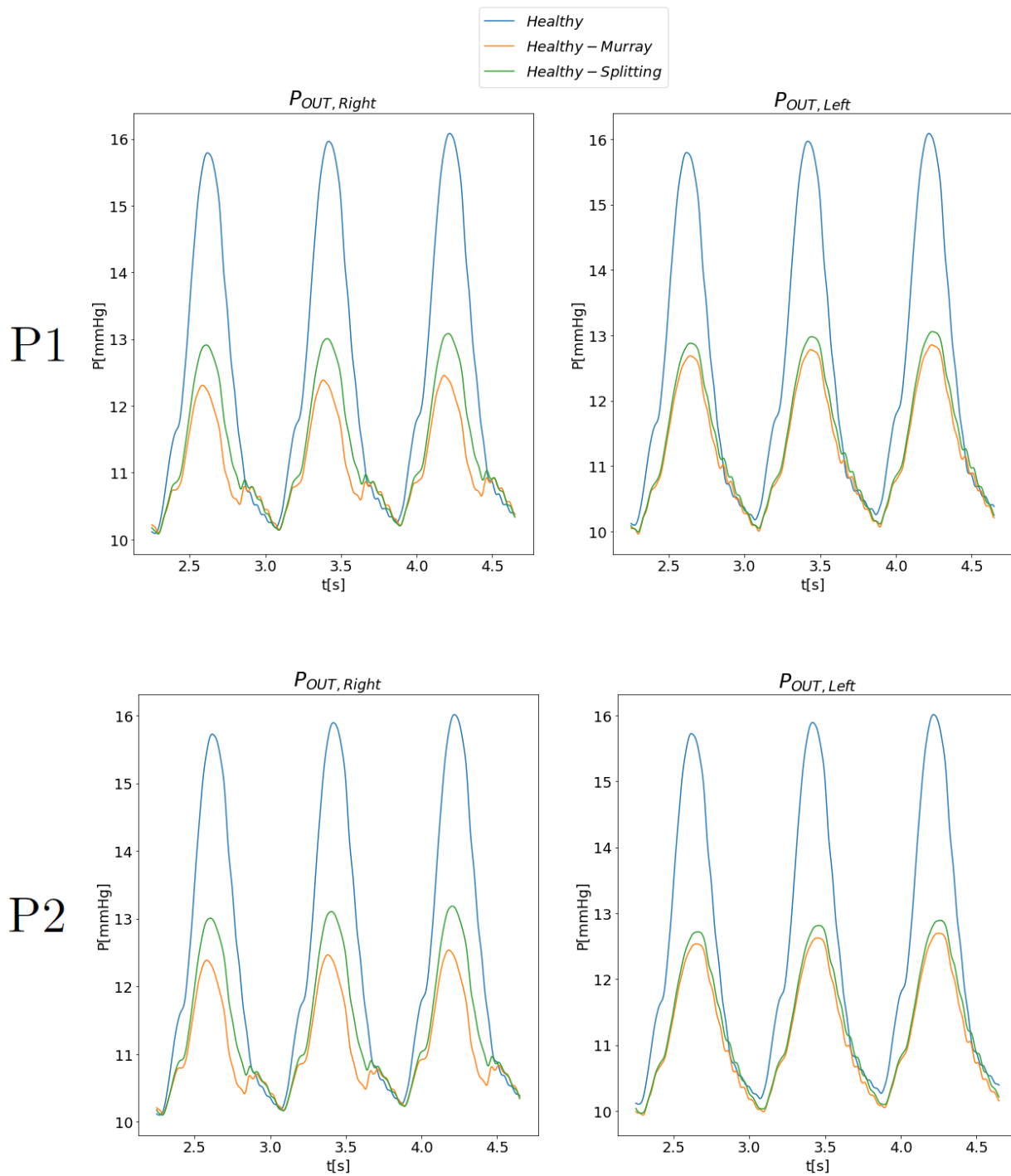


Figure 5.11: Comparison between the pressures in the two branches of the artery in the *Healthy*, *Healthy-Murray* and *Healthy-Splitting* simulations during the last three heartbeats of Patient 1 (top) and Patient 2.

5.2.3. Velocity field

Regarding the 3D views of the quantities, we first of all compared the velocity fields. We decided to focus on the diastolic phase since in this phase both the effects of the operation (see section 5.1) and the ones of the outlet differentiation were more evident. In Figures 5.12 and 5.13 we report a comparison of all the simulations at the diastolic instant $t = 4.45s$, respectively for Patient 1 and for Patient 2.

Referring to both patients, we can clearly see the effects of the imposition of different conditions at the outlets in the second and third rows of the figures, compared to the first row. During the diastolic phase, in fact, since the flow is diminishing, the traction at the left outlet seems to be too high, so the majority of the flow enters the right branch and some vortexes instead form in the left one, creating some backflow. Moreover, for both patients in the three *Murray* simulations (central rows), where the tractions at the outlets have a bigger difference, this effect is more evident if compared to the one of the *Splitting* simulations (last rows of figures). Regarding Patient 2, the *Post-Murray* and *Post-Splitting* simulations show that the recirculation region in the left branch is slightly translated toward the center of the artery bifurcation with respect to the Post simulation, possibly due to the greater backflow. These results seem to indicate the importance of differentiating in the proper way the boundary conditions at the outlets since different trends in the velocity fields can be observed.

In Figure 5.14 we compare instead the diastolic velocity of the blood in the sole simulations performed with Algorithm 2, for both patients. Each subfigure contains a zoom focused respectively on the bifurcation and right branch of Patient 1 (top) and on the bifurcation and left branch of Patient 2 (bottom). Regarding Patient 1, the main difference between the *-Murray* and *-Splitting* simulations (first and second row, respectively) lies in the repartition of the flow, especially in the Healthy cases on the left. The recirculation region in the right branch is a constant of all cases and the trend we had noticed with Algorithm 1, of the recirculation being more predominant in the Pre case than in the other two, can still be observed for each row. If we instead look at the results for Patient 2, it seems that the flow, in all cases, mainly enters the right branch in all the simulations, and a ricirculation region can be seen at the bifurcation, toward the left branch, in all cases. The geometry of the patient, together with the unbalanced conditions at the two outlets, seem to encourage the formation of the recirculation region and discourage the blood from entering the left branch.

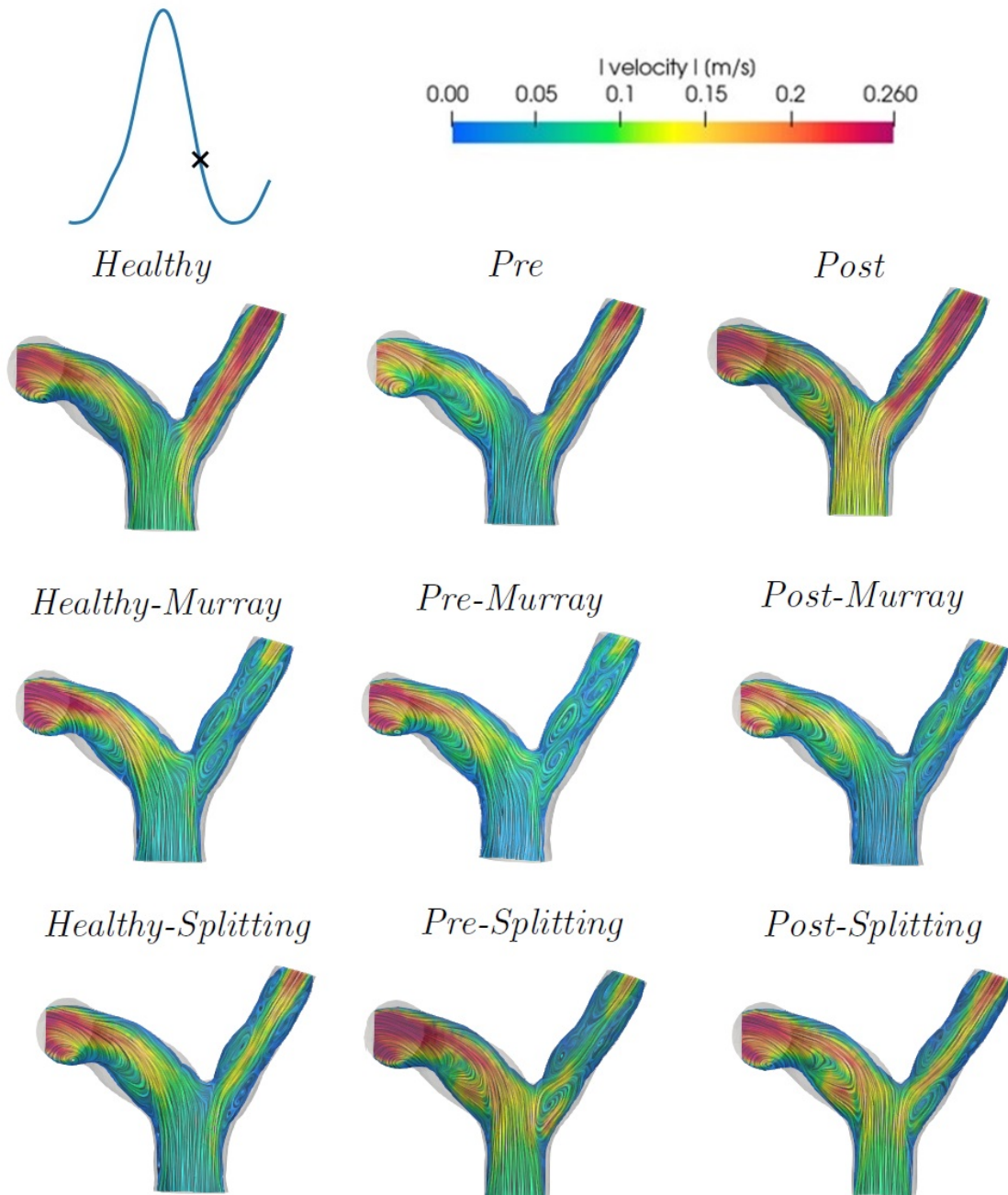


Figure 5.12: Patient 1: Comparison between the flow velocities during the diastole in all the nine simulations.

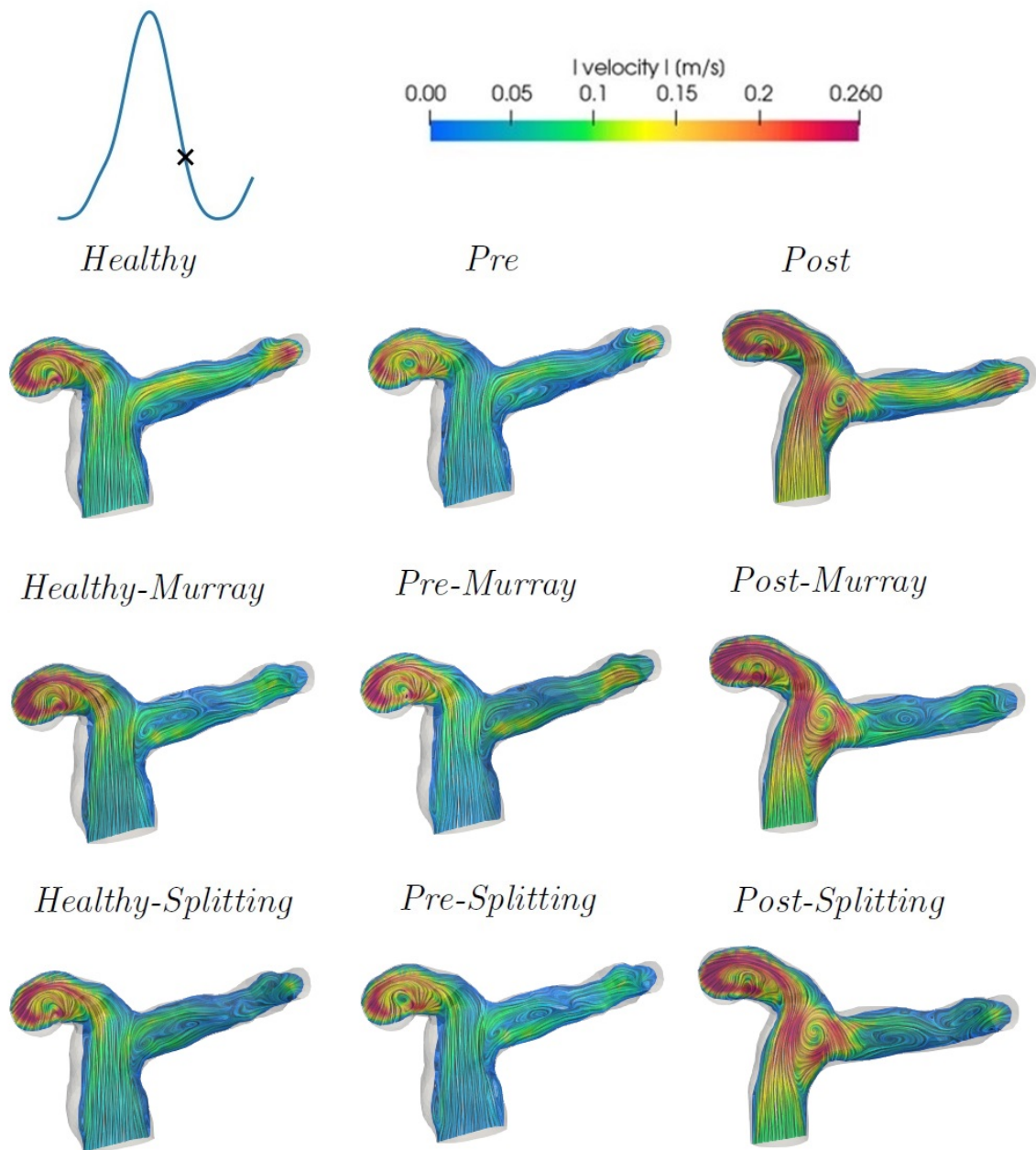


Figure 5.13: Patient 2: Comparison between the flow velocities during the diastole in all the nine simulations.

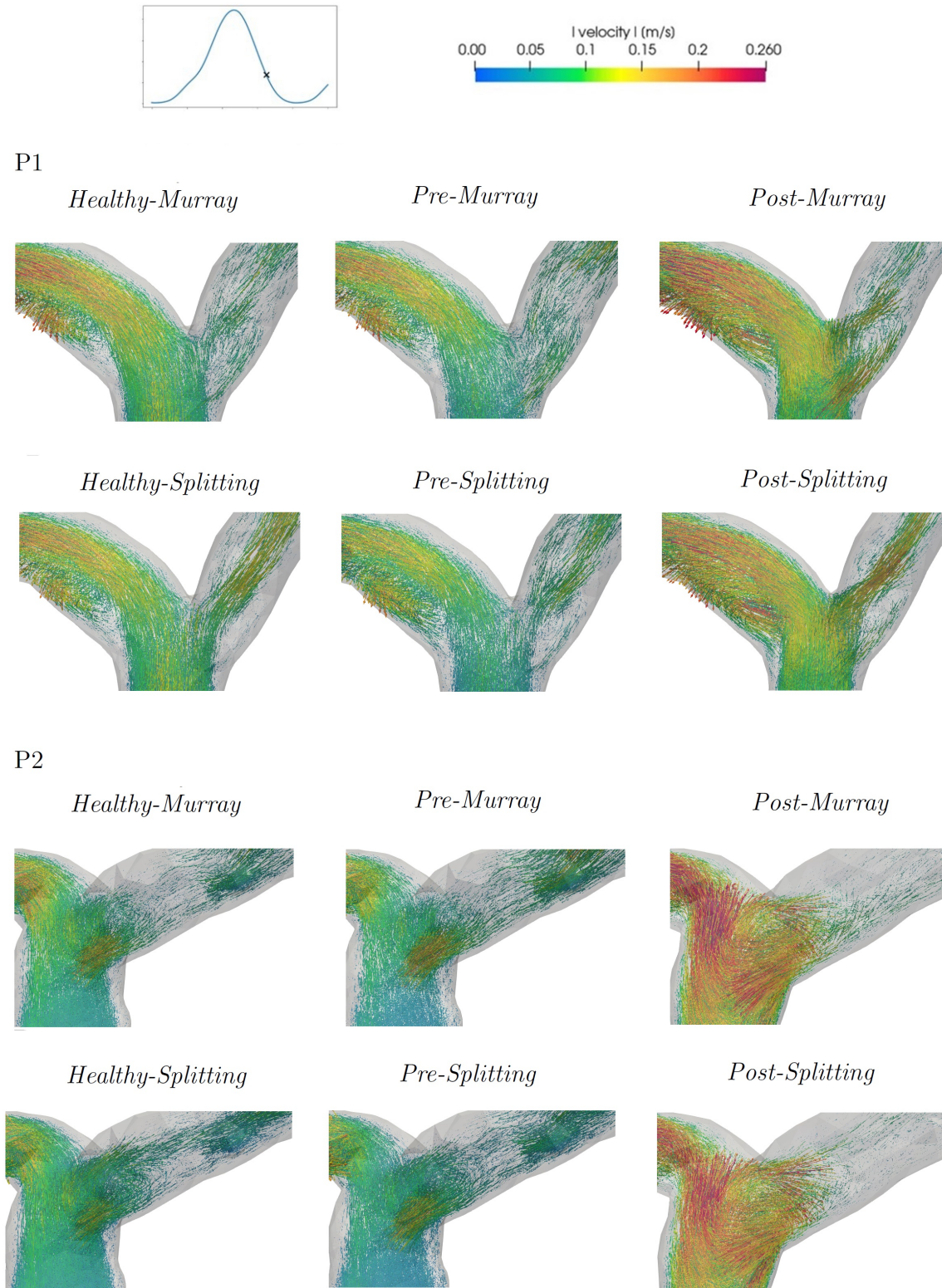


Figure 5.14: Comparison between the flow velocities during the diastole of both patients in the *Murray* (top) and *Splitting* (bottom) simulations.

5.2.4. Pressure field

We then proceeded by comparing the pressures during the diastolic phase of both patients in the *Post* simulations performed with Algorithm 2. Figure 5.15 shows the results for Patient 1 at the top and for Patient 2 at the bottom in the *Post-Murray* (left) and *Post-Splitting* (right) simulations. From this figure we can see the pressure difference at the two outlets, which is more evident in the *Murray* simulations with respect to the *Splitting* ones. However, also in the *Murray* simulations, the pressure gradient between the two branches is very small, if we refer to the scale of the figure. This is interesting if compared to the instead very unbalanced repartition of the flow that we have seen in the previous section.

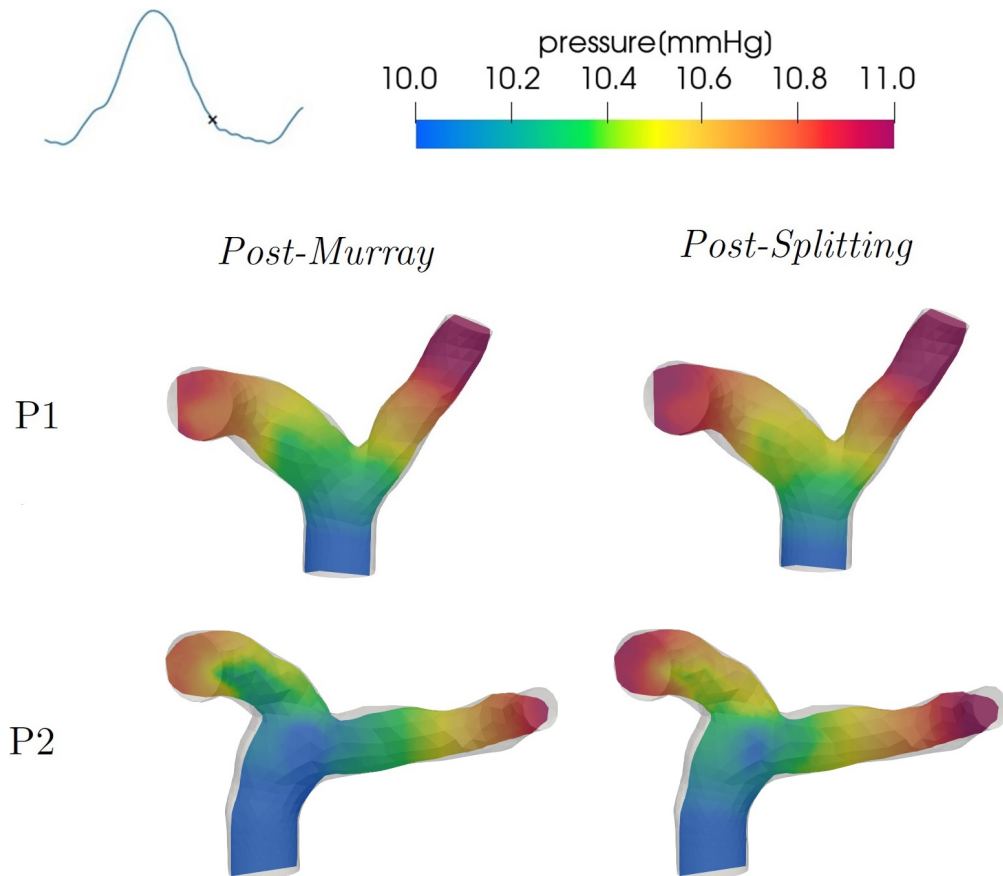


Figure 5.15: Comparison between the pressures during the diastole of both patients in the *Post-Murray* (left) and *Post-Splitting* (right) simulations.

For the pressure we also decided to analyse the moment of the systolic peak, which is shown in Figure 5.16, at the top for Patient 1 and at the bottom for Patient 2. In particular we

only compared the three Pre with the three Post simulations in order to analyse the effects of the imposition of different conditions at the outlets. The pressure scale of this figure was purposely chosen to be wider than the one of the previous figure, in order to capture the variance among the pressures. At this scale, where the pre or post operative condition of the patient does not affect the values of the pressure very significantly (looking at the figure along the columns), the imposition of different pressure boundary condition causes instead a variation of the pressure which is clearly visible (looking at the figure along the rows).

5.2.5. Wall Shear Stress analysis

The last quantity we analysed was the WSS and we focused on the systolic peak of the three pre-operative and the three post-operative simulations of the patients. The results can be seen in Figure 5.17. The greatest differences can be noticed if we compare a *Pre* simulation with a *Post* simulation in all cases (looking at the figure along the columns). The WSS is higher in all cases both in the inflow region and in the zone where the right branch bends. It is instead lower in the left branch of Patient 2 and right branch of Patient 1.

Comparing instead the figures along the rows, we can notice, as expected, a trend in which the zones coloured in red in the *Splitting* simulations (right column) are quantitatively in between the ones obtained with algorithm 1 (left column) and the ones in the *Murray* simulations (center column). This phenomenon is however very mild and in general the WSS pattern does not seem to differ significantly by differentiating the outlet boundary conditions.

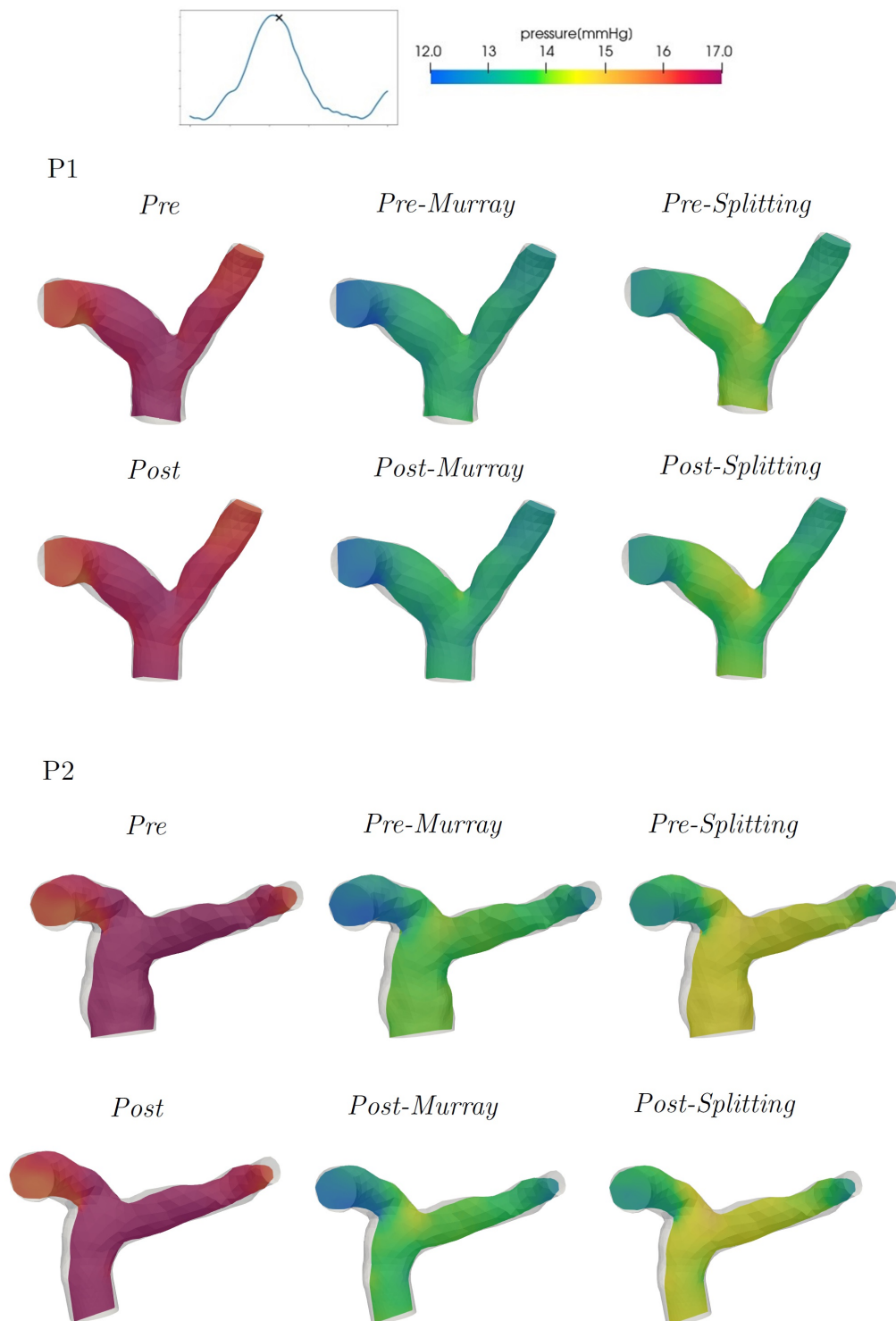


Figure 5.16: Comparison between the pressures during the systolic peak of both patients in the *Pre* (top) and *Post* (bottom) scenarios.

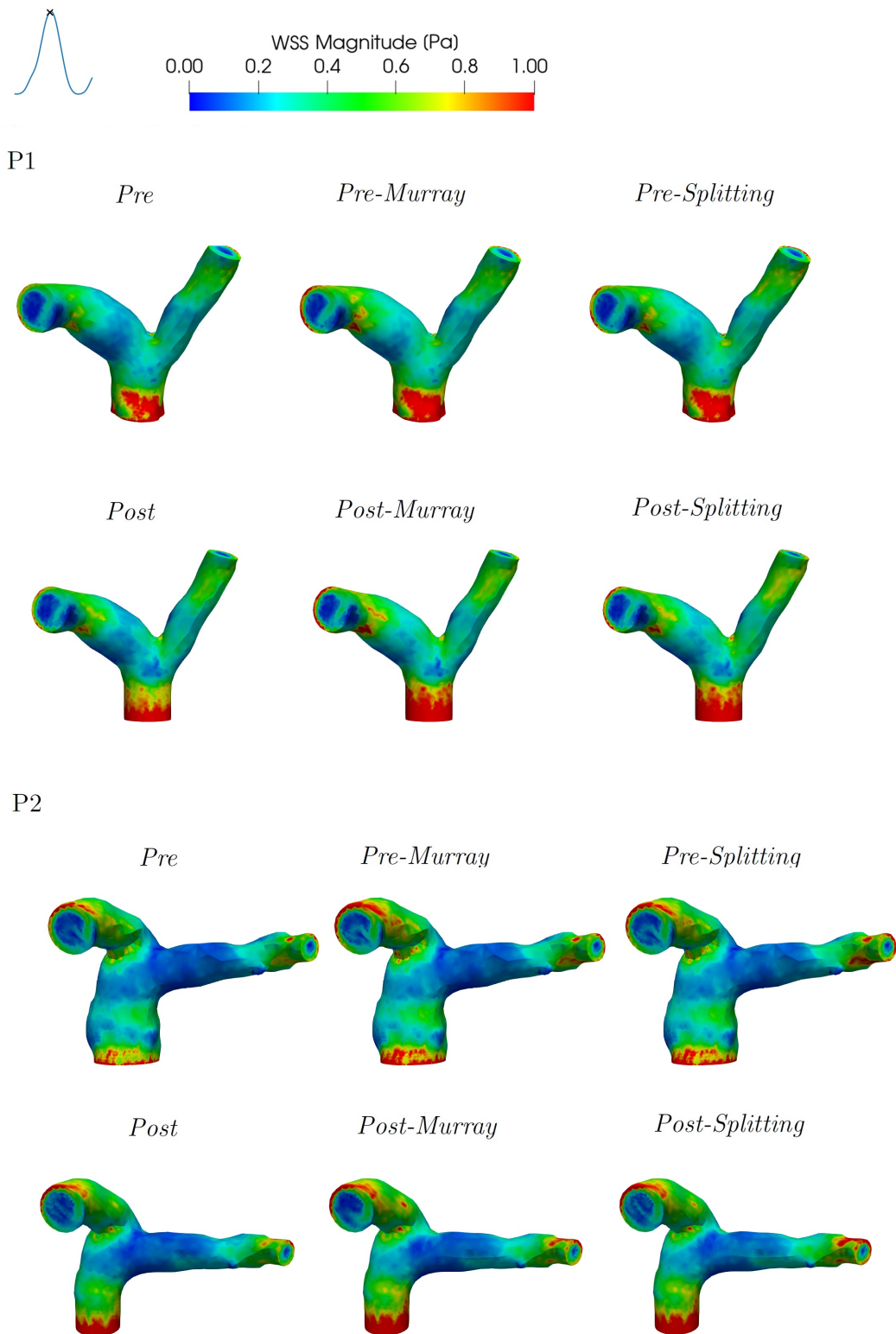


Figure 5.17: Comparison between the WSS during the systolic peak of both patients in the *Pre* (top) and *Post* (bottom) scenarios.

6 | Final remarks, limitations and future developments

The goal of our work was to provide a computational study of the hemodynamics in the pulmonary artery of two patients with a repaired congenital heart disease (Tetralogy of Fallot) following a prosthetic pulmonary valve replacement (PVR) operation. We adopted a 3D-0D geometric multiscale coupled fluid dynamics model of the heart circulation reconstructing the pulmonary artery geometry of the two patients from their CT scans. We compared a healthy, a pre-operative and a post-operative scenario in order to assess the effectiveness of the valve replacement operation and studied the flow repartition at the main pulmonary bifurcation with three different approaches for the imposition of the boundary conditions.

The main results of our work are the following.

1. We have found that the pulmonary valve replacement operation tends to restore the trend of the hemodynamic quantities making them closer to a healthier condition, in particular concerning the flow velocity. On the other hand, we have highlighted the importance of the valve positioning during the operation and this factor could be interesting to investigate from a medical point of view.
2. We have found that, for both patients, the post-operative scenario, where the inflow is narrowed due to the prosthetic stent of the valve, is characterised by a higher flow rate with respect to the healthy and pre-operative scenarios. This result can be considered as positive since the medical values we had at our disposal for Patient 1 indicated a low flow due to the low stroke volume.
3. We have noticed the formation of vortexes in one of the two branches of both patients, particularly in their pre-operative condition. From a medical point of view, the results on the formation of recirculation regions are interesting since an eventual transition to a turbulent regime may cause the onset of atherosclerotic lesions due to local stasis and jet-stream impingement upon the arterial wall.
4. From the study on the importance of the outlet boundary conditions to assess the

flow repartition, we have first of all proved the importance of the geometrical patient-specificity of the model, because of the different repartition of the flow for the two patients. Moreover, we have observed the formation of vortexes in the left branch of the two patients when differentiating the outlet boundary conditions and this effect was more evident when the two conditions differed the most. Therefore imposing the correct outlet BCs resulted being important to properly analyse a whole heartbeat.

We now address the limitations and further developments of our work.

1. The first limitation regards the results obtained for Patient 2. Indeed, despite being meaningful thanks to the geometric reconstruction from the patient's CT scans of the pulmonary artery, the results for this patient were not as accurate as the ones for Patient 1, since we did not have specific clinical measures.
2. Another limitation of our study was that we have worked under the hypothesis that the pre-operative artery geometry was equal to the post-operative one. The existence of CT scans of the patients from before the pulmonary valve replacement operation would have made our results more accurate.
3. Regarding the valve modeling, a 3D reconstruction of the prosthetic valve could be adopted, in order to avoid the use of the diode for the simulation of the leaflets in the 0D model. Indeed we would have expected a higher backflow at the 3D inflow region of the two patients in their pre-operative condition, due to the total absence of the pulmonary valve. This phenomenon was significantly noticed only in the 0D quantities, where however a clear indication for surgery was highlighted by the entity of the backflow and pressure overload on the ventricle.
4. Regarding the outlet boundary conditions, for more accurate simulations, we would have needed a measure for the patients' pressure in the branches of the arteries, in order to know which flow repartition to expect. Indeed, although the patient's geometry has proven to be important, having the two branches different shapes and sizes, the pressures are likely to differ too.
5. Finally, another limitation of our work regards the magnitude of some quantities, such as the WSS or the velocity, which may be slightly overestimated due to the rigid-wall assumption of our model. The overall flow patterns should not be significantly altered by relaxing this hypothesis [11], however, although the wall compliance has been modeled partly through the 0D part of the model, the model could be improved by considering an FSI approach in the 3D domain of the artery.

Tetralogy of Fallot is one of the most common cyanotic Congenital Heart Diseases [9]. However, not many works have been performed on this subject to this day. We therefore hope that our work will be seen as a starting point for future studies on patients with similar medical conditions.

Bibliography

- [1] E. S. American Heart Association. Tetralogy of fallot, 2022. URL <https://www.heart.org/en/health-topics/congenital-heart-defects/about-congenital-heart-defects/tetralogy-of-fallot>.
- [2] L. Antiga and D. Steinman. Rethinking turbulence in blood. *Biorheology*, 46:77–81, 02 2009. doi: 10.3233/BIR-2009-0538.
- [3] Artemiou P., Schusterova I., Tohatyova A., Cocherova J., Krcho P, and Sabol F. Follow-up after the ross procedure, how significant it is, case reports of three patients. *J Cardiothorac Surg.*, 10(144), 2015. doi: 10.1186/s13019-015-0369-8.
- [4] H. Baumgartner, J. De Backer, S. V. Babu-Narayan, W. Budts, M. Chessa, G.-P. Diller, B. lung, J. Kluin, I. M. Lang, F. Meijboom, P. Moons, B. J. M. Mulder, E. Oechslin, J. W. Roos-Hesselink, M. Schwerzmann, L. Sondergaard, K. Zeppenfeld, and E. S. D. Group. 2020 ESC Guidelines for the management of adult congenital heart disease: The Task Force for the management of adult congenital heart disease of the European Society of Cardiology (ESC). Endorsed by: Association for European Paediatric and Congenital Cardiology (AEPC), International Society for Adult Congenital Heart Disease (ISACHD). *European Heart Journal*, 42(6):582–615, 08 2020. ISSN 0195-668X. doi: 10.1093/eurheartj/ehaa554. URL <https://doi.org/10.1093/eurheartj/ehaa554>.
- [5] L. Bennati. A computational fluid structure interaction study in the carotids in presence of atherosclerotic plaque. Master’s thesis, Politecnico di Milano, 2019.
- [6] C. Bertoglio and A. Caiazzo. A tangential regularization method for backflow stabilization in hemodynamics. *Journal of Computational Physics*, 261:162–171, 2014. ISSN 0021-9991. doi: <https://doi.org/10.1016/j.jcp.2013.12.057>. URL <https://www.sciencedirect.com/science/article/pii/S0021999114000126>.
- [7] Bessonov, N., Sequeira, A., Simakov, S., Vassilevskii, Yu., and Volpert, V. Methods of blood flow modelling. *Math. Model. Nat. Phenom.*, 11(1):1–25, 2016. doi: 10.1051/mmnp/201611101. URL <https://doi.org/10.1051/mmnp/201611101>.

- [8] M. Boumpouli, M. H. Danton, T. Gourlay, and A. Kazakidi. Blood flow simulations in the pulmonary bifurcation in relation to adult patients with repaired tetralogy of fallot. *Medical Engineering Physics*, 85:123–138, 2020. ISSN 1350-4533. doi: <https://doi.org/10.1016/j.medengphy.2020.09.014>. URL <https://www.sciencedirect.com/science/article/pii/S1350453320301478>.
- [9] M. Boumpouli, E. L. Sauvage, C. Capelli, S. Schievano, and A. Kazakidi. Characterization of flow dynamics in the pulmonary bifurcation of patients with repaired tetralogy of fallot: A computational approach. *Frontiers in Cardiovascular Medicine*, 8, 2021. ISSN 2297-055X. doi: 10.3389/fcvm.2021.703717. URL <https://www.frontiersin.org/article/10.3389/fcvm.2021.703717>.
- [10] K. A. Brown KN. Aortic valve ross operation., 2022. URL <https://www.ncbi.nlm.nih.gov/books/NBK537249/>.
- [11] F. Capuano, Y.-H. Loke, and E. Balaras. Blood flow dynamics at the pulmonary artery bifurcation. *Fluids*, 4:190, 11 2019. doi: 10.3390/fluids4040190.
- [12] C. Chnafa, O. Brina, V. Pereira, and D. Steinman. Better than nothing: A rational approach for minimizing the impact of outflow strategy on cerebrovascular simulations. *American Journal of Neuroradiology*, 2018. ISSN 0195-6108. doi: 10.3174/ajnr.A5484. URL <http://www.ajnr.org/content/early/2017/12/21/ajnr.A5484>.
- [13] M. Fedele. marco-fedele/vmtk. <https://github.com/marco-fedele/vmtk>.
- [14] M. Fedele and A. Quarteroni. Polygonal surface processing and mesh generation tools for the numerical simulation of the cardiac function. *International Journal for Numerical Methods in Biomedical Engineering*, 37, 01 2021. doi: 10.1002/cnm.3435.
- [15] B. D. Gerard J Tortora. *Introduction to the human body : the essentials of anatomy and physiology*. John Wiley Sons, 8th edition, 2010. ISBN 9780470230169,0470230169.
- [16] S. Ghiselli, C. Carro, N. Uricchio, G. Annoni, and S. M. Marianeschi. Mid- to long-term follow-up of pulmonary valve replacement with BioIntegral injectable valve. *Eur J Cardiothorac surg*, 59(2):325–332, 11 2020.
- [17] R. Guibert, K. McLeod, A. Caiazzo, T. Mansi, M. A. Fernández, M. Sermesant, X. Pennec, I. E. Vignon-Clementel, Y. Boudjemline, and J.-F. Gerbeau.
- [18] R. Gupta, A. C. Cheung, S. H. Bartling, J. Lisauskas, M. Grasruck, C. Leidecker, B. Schmidt, T. Flohr, and T. J. Brady. Flat-panel volume ct: Fundamental principles,

- technology, and applications. *RadioGraphics*, 28(7):2009–2022, 2008. doi: 10.1148/rg.287085004. URL <https://doi.org/10.1148/rg.287085004>. PMID: 19001655.
- [19] itk. An open-source, cross-platform library that provides developers with an extensive suite of software tools for image analysis. <https://itk.org/>.
- [20] D. Katritsis, L. Kaiktsis, A. Chaniotis, J. Pantos, E. P. Efstathopoulos, and V. Marmarelis. Wall shear stress: theoretical considerations and methods of measurement. *Progress in cardiovascular diseases*, 49(5):307–329, 2007. ISSN 0033-0620. doi: 10.1016/j.pcad.2006.11.001. URL <https://doi.org/10.1016/j.pcad.2006.11.001>.
- [21] F. Kong, V. O. Kheifets, E. A. Finol, and X.-C. Cai. Simulation of unsteady blood flows in a patient-specific compliant pulmonary artery with a highly parallel monolithically coupled fluid-structure interaction algorithm. *International journal for numerical methods in biomedical engineering*, 35 7:e2952, 2019.
- [22] J.-W. Lankhaar, N. Westerhof, T. J. C. Faes, K. M. J. Marques, J. T. Marcus, P. E. Postmus, and A. Vonk-Noordegraaf. Quantification of right ventricular afterload in patients with and without pulmonary hypertension. *American Journal of Physiology-Heart and Circulatory Physiology*, 291(4):H1731–H1737, 2006. doi: 10.1152/ajpheart.00336.2006. URL <https://doi.org/10.1152/ajpheart.00336.2006>. PMID: 16699074.
- [23] LifeX. *lifex^x* (/,lafks/). a high-performance finite element library mainly focused on mathematical models and numerical methods for cardiac applications. <https://lifex.gitlab.io/lifex/>.
- [24] J. Liu, W. Yang, I. S. Lan, and A. L. Marsden. Fluid-structure interaction modeling of blood flow in the pulmonary arteries using the unified continuum and variational multiscale formulation. *Mechanics Research Communications*, 107:103556, 2020. ISSN 0093-6413. doi: <https://doi.org/10.1016/j.mechrescom.2020.103556>. URL <https://www.sciencedirect.com/science/article/pii/S0093641320300847>.
- [25] A. M. Maceira, S. K. Prasad, M. T. Khan, and D. J. Pennell. Reference right ventricular systolic and diastolic function normalized to age, gender and body surface area from steady-state free precession cardiovascular magnetic resonance. *European heart journal*, 27 23:2879–88, 2006.
- [26] F. Marcinnò. A computational study of blood dynamics in the pulmonary arteries. Master’s thesis, Politecnico di Milano, 2021.
- [27] S. Marianeschi. Application of artificial valves in right ventricular tract recon-

- struction. <https://peters-surgical.com/event/title-event/>, 2021. Accessed: 2022-02-28.
- [28] Matlab. A programming and numeric computing platform. <https://it.mathworks.com/products/matlab.html>.
- [29] mitk. The medical imaging interaction toolkit. [https://www.mitk.org/wiki/The_Medical_Imaging_Interaction_Toolkit_\(MITK\)](https://www.mitk.org/wiki/The_Medical_Imaging_Interaction_Toolkit_(MITK)).
- [30] C. D. Murray. The physiological principle of minimum work. i. the vascular system and the cost of blood volume. *Proceedings of the National Academy of Sciences of the United States of America*, 12(3):207–214, 1926. ISSN 00278424. URL <http://www.jstor.org/stable/85001>.
- [31] T. R. of the University of California. Tetralogy of fallot, 2022. URL <https://surgery.ucsf.edu/conditions--procedures/tetralogy-of-fallot.aspx>.
- [32] A. J. Pappano and W. Gil Wier. 6 - hemodynamics. In A. J. Pappano and W. Gil Wier, editors, *Cardiovascular Physiology (Tenth Edition)*. Elsevier, Philadelphia, tenth edition edition, 2013. ISBN 978-0-323-08697-4. doi: <https://doi.org/10.1016/B978-0-323-08697-4.00006-X>. URL <https://www.sciencedirect.com/science/article/pii/B978032308697400006X>.
- [33] Paraview. An open-source, multi-platform data analysis and visualization application. <https://www.paraview.org/>.
- [34] T. A. Pastor, T. Geva, M. Lu, V. E. Duarte, S. Drakeley, L. A. Sleeper, and A. M. Valente. Relation of Right Ventricular Dilation After Pulmonary Valve Replacement to Outcomes in Patients With Repaired Tetralogy of Fallot. *The American journal of cardiology*, 125,6:977–981, 2020. doi: 10.1016/j.amjcard.2019.12.017.
- [35] M. C. Paul, M. Mamun Molla, and G. Roditi. Large-eddy simulation of pulsatile blood flow. *Medical Engineering Physics*, 31(1):153–159, 2009. ISSN 1350-4533. doi: <https://doi.org/10.1016/j.medengphy.2008.04.014>. URL <https://www.sciencedirect.com/science/article/pii/S1350453308000829>.
- [36] R. Perfetti. *Circuiti elettrici*. Zanichelli, 2003. ISBN 9788808076472. URL <https://books.google.it/books?id=lhbCAAACAAJ>.
- [37] G. Polazzo, A. Sapienza, and A. Zaccaria. Mricostruzione geometrica dell’arteria polmonare in pazienti con valvola autoespandibile. Bachelor Thesis. Politecnico di Milano, 2021.

- [38] R. Ponzini, C. Vergara, A. Redaelli, and A. Veneziani. Reliable cfd-based estimation of flow rate in haemodynamics measures. *Ultrasound in Medicine Biology*, 32(10):1545–1555, 2006. ISSN 0301-5629. doi: <https://doi.org/10.1016/j.ultrasmedbio.2006.05.022>. URL <https://www.sciencedirect.com/science/article/pii/S0301562906016358>.
- [39] A. Quarteroni. *Numerical Models for Differential Problems*. Springer Publishing Company, Incorporated, 2nd edition, 2013. ISBN 8847055210.
- [40] A. Quarteroni, S. Ragni, and A. Veneziani. Coupling between lumped and distributed models for blood flow problems. *Computing and Visualization in Science*, 4:111–124, 12 2001. doi: 10.1007/s007910100063.
- [41] A. Quarteroni, A. Veneziani, and C. Vergara. Geometric multiscale modeling of the cardiovascular system, between theory and practice. *Computer Methods in Applied Mechanics and Engineering*, 302:193–252, 2016. ISSN 0045-7825. doi: <https://doi.org/10.1016/j.cma.2016.01.007>. URL <https://www.sciencedirect.com/science/article/pii/S0045782516000098>.
- [42] A. Quarteroni, A. Manzoni, and C. Vergara. The cardiovascular system: Mathematical modelling, numerical algorithms and clinical applications. *Acta Numerica*, 26: 226. 365–590, 2017. doi: 10.1017/S0962492917000046. URL <http://infoscience.epfl.ch/record/229843>.
- [43] A. Quarteroni, F. Saleri, and P. Gervasio. *Calcolo Scientifico*. Springer-Verlag Italia Srl., 2017. ISBN 978-88-470-3952-0. doi: <https://doi.org/10.1007/978-88-470-3953-7>.
- [44] D. S. Rawat, M. Pourquie, and C. Poelma. Numerical Investigation of Turbulence in Abdominal Aortic Aneurysms. *Journal of Biomechanical Engineering*, 141(6), 04 2019. ISSN 0148-0731. doi: 10.1115/1.4043289. URL <https://doi.org/10.1115/1.4043289>. 061001.
- [45] F. Regazzoni, M. Salvador, P. C. Africa, M. Fedele, L. Dede', and A. Quarteroni. A cardiac electromechanics model coupled with a lumped parameters model for closed-loop blood circulation. part i: model derivation, 2020. URL <https://arxiv.org/abs/2011.15040>.
- [46] T. F. Sherman. On connecting large vessels to small. The meaning of Murray's law. *Journal of General Physiology*, 78(4):431–453, 10 1981. ISSN 0022-1295. doi: 10.1085/jgp.78.4.431. URL <https://doi.org/10.1085/jgp.78.4.431>.
- [47] G. Simonneau, D. Montani, D. S. Celermajer, C. P. Denton, M. A. Gatzoulis,

- M. Krowka, P. G. Williams, and R. Souza. Haemodynamic definitions and updated clinical classification of pulmonary hypertension. *European Respiratory Journal*, 53(1), 2019. ISSN 0903-1936. doi: 10.1183/13993003.01913-2018. URL <https://erj.ersjournals.com/content/53/1/1801913>.
- [48] B. T. Tang, T. A. Fonte, C. F. P., P. S. Tsao, J. A. Feinstein, and C. A. Taylor. Three-dimensional hemodynamics in the human pulmonary arteries under resting and exercise conditions. *Annals of Biomedical Engineering*, 39, 2011. ISSN 347–358. doi: <https://doi.org/10.1007/s10439-010-0124-1>.
- [49] B. T. Tang, S. S. Pickard, F. P. Chan, P. S. Tsao, C. A. Taylor, and J. A. Feinstein. Wall shear stress is decreased in the pulmonary arteries of patients with pulmonary arterial hypertension: An image-based, computational fluid dynamics study. *Pulmonary circulation*, 2 4>:470–6, 2012.
- [50] J. van der Ven, E. van den Bosch, A. Bogers, and W. Helbing. Current outcomes and treatment of tetralogy of fallot. *F1000 Research*, 8, 08 2019. doi: 10.12688/f1000research.17174.1.
- [51] vmtk. The vascular modeling toolkit. <http://www.vmtk.org/>.
- [52] vtk. An open source software for manipulating and displaying scientific data. <https://vtk.org/>.
- [53] F. C. C. S. A. M. S. P. N. Wesolowski, Sigmund A. The significance of turbulence in hemic systems and in the distribution of the atherosclerotic lesion. *Surgery*, 57: 155–62, 01 1965.
- [54] S. R. Wilcox, C. Kabrhel, and R. N. Channick. Pulmonary hypertension and right ventricular failure in emergency medicine. *Annals of emergency medicine*, 66 6:619–28, 2015.
- [55] E. E. Williams and I. El-Hamamsy. The ross procedure. *Operative Techniques in Thoracic and Cardiovascular Surgery*, 26(2):189–209, 2021. ISSN 1522-2942. doi: <https://doi.org/10.1053/j.optechstcvs.2020.12.004>. URL <https://www.sciencedirect.com/science/article/pii/S1522294221000076>.
- [56] W. Yang, M. Dong, M. Rabinovitch, F. Chan, A. Marsden, and J. Feinstein. Evolution of hemodynamic forces in the pulmonary tree with progressively worsening pulmonary arterial hypertension in pediatric patients. *Biomechanics and Modeling in Mechanobiology*, 18:1–18, 06 2019. doi: 10.1007/s10237-018-01114-0.
- [57] A. Yartsev. Ventricular pressure-volume loops.

<https://derangedphysiology.com/main/cicm-primary-exam/required-reading/cardiovascular-system/Chapter>

- [58] A. P. Yoganathan, E. G. Cape, H.-W. Sung, F. P. Williams, and A. Jimoh. Review of hydrodynamic principles for the cardiologist: Applications to the study of blood flow and jets by imaging techniques. *Journal of the American College of Cardiology*, 12(5):1344–1353, 1988. ISSN 0735-1097. doi: [https://doi.org/10.1016/0735-1097\(88\)92620-4](https://doi.org/10.1016/0735-1097(88)92620-4). URL <https://www.sciencedirect.com/science/article/pii/0735109788926204>.
- [59] J. Q. Zhou, A. F. Corno, C. H. Huber, P. Tozzi, and L. K. von Segesser. Self-expandable valved stent of large size: off-bypass implantation in pulmonary position. *European Journal of Cardio-Thoracic Surgery*, 24(2):212–216, 08 2003. ISSN 1010-7940. doi: [10.1016/S1010-7940\(03\)00178-7](https://doi.org/10.1016/S1010-7940(03)00178-7). URL [https://doi.org/10.1016/S1010-7940\(03\)00178-7](https://doi.org/10.1016/S1010-7940(03)00178-7).

List of Figures

1.1	The main elements of the human heart [42].	2
1.2	A schematic image of blood circulation in the heart [15].	4
1.3	Pressure variation of the right side of the heart during a heartbeat [32]. . .	5
1.4	Difference between a normal heart (left) and a heart with Tetralogy of Fallot (right) [31].	7
1.5	Initial palliation (left) and complete repair (right) of TOF [1].	8
1.6	Longterm complications of rTOF [4].	8
1.7	The Ross procedure: substitution of the aortic valve with the pulmonary valve (left) and pulmonary valve replacement (right).	10
1.8	The <i>No-React</i> [®] Injectable <i>BioPulmonic</i> TM Prosthesis (Bio Integral Surgical, Inc., Mississauga, ON, Canada) used in [16].	11
2.1	Left: Natural inflow of the pulmonary artery. Right: Post PVR inflow with the valve stent.	18
2.2	Patient 1. Example of a CT scan in mhd format.	20
2.3	Example of physical and artificial boundaries of a pulmonary artery.	21
2.4	Example of placement of the seeds at the inflow (on the right) and at the outflows (on the left) with VMTK.	21
2.5	Reconstructed geometries of the pulmonary arteries from the CT scans of Patient 1 (left) and Patient 2 (right).	22
2.6	Diagram of the modeling of the three scenarios: <i>Healthy</i> (native geometry + diode), <i>Pre</i> (native geometry, no diode) and <i>Post</i> (stent geometry + diode).	24
2.7	A) The pulmonary arteries with all the outlets for Patient 1 (top) and Patient 2 (bottom). B) The pulmonary arteries with just the two main outlets for Patient 1 (top) and Patient 2 (bottom).	25
2.8	Identification of the stent points from Patient 1's CT scans.	26
2.9	A) The arteries of Patient 1 (top) and Patient 2 (bottom) before the cutting operation at the level of the beginning of the valve zone. B) The arteries of the two patients after the cutting operation.	26

2.10	Generation of the <i>Post</i> meshes for Patient 1 (left) and Patient 2 (right). A) Cutting of the artery and construction of a stent of the correct size. B) Positioning of the stent. C) Attachment of the stent to the artery.	29
2.11	On the left the function Phi describing the geometry of Patient 1, on the right the edgelengh chosen for the meshes with respect to Phi.	30
2.12	Final meshes in the <i>Healthy/Pre</i> (top left and right respectively for Patient 1 and 2) and <i>Post</i> (bottom left and right respectively for Patient 1 and 2) scenarios.	31
3.1	3D domain of the model.	34
3.2	Example of backflow instability: the velocity vectors at the time of peak flow (left) and when the backflow begins during the diastole (center and right) [6].	38
3.3	Representation of the artery in 1D.	43
3.4	Top left: L network. Bottom left: L-inverted network. Top right: π network. Bottom right: T network.	46
3.5	0D circulation model [23]	48
3.6	Left: Graph of the time-dependent resistance of the 0D heart valves. Right: Heart chamber coupled with its valve (diode).	49
3.7	Geometric multiscale 3D-0D coupled model	54
3.8	Variant of the 0D model where the two pulmonary artery branches are differentiated.	59
3.9	Geometric multiscale 3D-0D coupled model with two RLC circuits at the outlets of the pulmonary artery.	60
4.1	Algorithm 1. Top: <i>Healthy</i> and <i>Post</i> scenarios, zoom of the zones of interest in Figure 3.7. Bottom: Pre scenario: zoom of the zone of interest in Figure 3.7 after the removal of the diode representing the pulmonary valve.	69
4.2	Algorithm 2. Top: <i>Healthy-Murray</i> and <i>Healthy-Splitting</i> , <i>Post-Murray</i> and <i>Post-Splitting</i> simulations: zoom of the zone of interest in Figure 3.9. Bottom: Algorithm 2. <i>Pre-Murray</i> and <i>Pre-splitting</i> simulations: Zoom of the zone of interest in Figure 3.9 but without the pulmonary valve (diode).	71
4.3	Example of two types of incorrect calibration. Left: Oscillations and non convergence of the linear solver. Right: Increasing flow rate at each heartbeat.	74
4.4	Right ventricle (RV) calibration on Patient 1, <i>Healthy</i> scenario. Top Left: RV Pressure variation. Top Right: RV Volume variation. Bottom Left: Obtained RV PV loop. Bottom Right: Normal RV PV loop [57].	80

4.5	<i>Healthy</i> scenario of Patient 1. Flow rate (left) and pressure (right) at the artificial boundaries during the last three heartbeats of the simulations, in view of the calibration procedure.	81
4.6	Diameter variation of the left branch of Patient 2's pulmonary artery.	85
5.1	Patient 1, <i>Healthy</i> simulation. Left: Inlet flow rate. Right: Outlet pressure field.	88
5.2	Velocity field in the <i>Healthy</i> (left), <i>Pre</i> (center) and <i>Post</i> (right) simulations for both patients at three significant heartbeat instants.	89
5.3	Velocity field during the diastolic phase in the <i>Healthy</i> (left), <i>Pre</i> (center) and <i>Post</i> (right) simulations. Top: Patient 1's right branch. Bottom: Patient 2's left branch.	91
5.4	Pressure field in the <i>Healthy</i> (left), <i>Pre</i> (center) and <i>Post</i> (right) simulations for both patients at three significant heartbeat instants.	93
5.5	Pressure field during the diastolic phase in the <i>Healthy</i> (left), <i>Pre</i> (center) and <i>Post</i> (right) simulations for Patient 1 (top) and Patient 2 (bottom).	95
5.6	WSS in the <i>Healthy</i> (left), <i>Pre</i> (center) and <i>Post</i> (right) simulations for both patients at the peak of the systole.	96
5.7	TAWSS of the last simulated heartbeat in the <i>Healthy</i> (left), <i>Pre</i> (center) and <i>Post</i> (right) simulations of both patients.	98
5.8	Patient 1. Left: Comparison between the flow at the pulmonary valve in the 0D model (Q_{PV}) in the three simulations. Right: Comparison between the pressure at the pulmonary valve in the 0D model (p_{TRK}) in the three simulations.	99
5.9	Patient 1. Comparison between the PV loops obtained by the 0D model in the 3 simulations.	100
5.10	Comparison among the flow rates in the two branches of the artery in the <i>Healthy</i> , <i>Healthy-Murray</i> and <i>Healthy-Splitting</i> simulations during the last three heartbeats of Patient 1 (top) and Patient 2.	102
5.11	Comparison between the pressures in the two branches of the artery in the <i>Healthy</i> , <i>Healthy-Murray</i> and <i>Healthy-Splitting</i> simulations during the last three heartbeats of Patient 1 (top) and Patient 2.	104
5.12	Patient 1: Comparison between the flow velocities during the diastole in all the nine simulations.	106
5.13	Patient 2: Comparison between the flow velocities during the diastole in all the nine simulations.	107

5.14	Comparison between the flow velocities during the diastole of both patients in the <i>Murray</i> (top) and <i>Splitting</i> (bottom) simulations.	108
5.15	Comparison between the pressures during the diastole of both patients in the <i>Post-Murray</i> (left) and <i>Post-Splitting</i> (right) simulations.	109
5.16	Comparison between the pressures during the systolic peak of both patients in the <i>Pre</i> (top) and <i>Post</i> (bottom) scenarios.	111
5.17	Comparison between the WSS during the systolic peak of both patients in the <i>Pre</i> (top) and <i>Post</i> (bottom) scenarios.	112

List of Tables

2.1	Information on the final hexahedral meshes of the two patients for the <i>Healthy/Pre</i> configuration.	31
2.2	Information on the final hexahedral meshes of the two patients for the <i>Post</i> configuration.	32
4.1	Clinical measures, corresponding to the ventricle parameters of Patient 1, used to calibrate the 0D model parameters.	75
4.2	Calibrated initial conditions for the 0D model. Algorithm 1 and 2.	75
4.3	0D model: calibrated parameters of the heart chambers.	76
4.4	0D model: calibrated parameters of the pulmonary and systemic venous systems and the systemic arterial system.	76
4.5	0D model: calibrated parameters of the heart valves.	77
4.6	0D model. Algorithm 1: calibrated parameters of the pulmonary artery compartments in the <i>Healthy</i> , <i>Pre</i> and <i>Post</i> scenarios for both patients. . .	77
4.7	0D model. Algorithm 2: calibrated parameters of the pulmonary artery compartments in the <i>Murray</i> and <i>Splitting</i> simulations of Patient 1 and Patient 2.	78
4.8	Comparison between the RV clinical measures and the values obtained for Patient 1.	79
4.9	Calibration on Patient 1, <i>Healthy</i> scenario. Comparison between the obtained flow rates and the literature ones [48].	82
4.10	Calibration on Patient 1, <i>Healthy</i> scenario. Comparison between the obtained pressures and the literature ones [22].	83
4.11	Comparison between the flow repartition of the Right (R) and Left (L) branch obtained by imposing the resistances according to (3.41) (first three columns) and the ones predicted by the Chnafa law in (3.45) (last column).	84
4.12	Comparison between the flow repartition of the two branches (R and L) of Patient 2 obtained in the <i>Post-splitting</i> simulations, the repartition estimated by the law in (3.45) and the diameters of the two branches considering different sections.	85

5.1	Mean flow in the main, right and left pulmonary arteries (MPA, RPA and LPA respectively) and flow repartition at the bifurcation of Patient 1 and Patient 2 in the Healthy scenarios.	101
5.2	Mean pressures assigned at the right and left outlets (RPA and LPA) of Patient 1 and Patient 2 in the three Healthy scenarios.	103

List of Symbols

BCs Boundary Conditions

CFD Computational Fluid Dynamics

CHD Congenital Heart Disease

CT Computed Tomography

LPA Left Pulmonary Artery

LVEDV Left Ventricle End Diastolic Volume

MPA Main Pulmonary Artery

PA Pulmonary Artery

PAH Pulmonary Artery Hypertrophy

PR Pulmonary Regurgitation

PVR Pulmonary Valve Replacement

RPA Right Pulmonary Artery

rTOF Repaired Tetralogy of Fallot

RV Right Ventricle

RVEDV Right Ventricle End Diastolic Volume

RVEF Right Ventricle Ejection Fraction

RVESV Right Ventricle End Systolic Volume

RVH Right Ventricle Hypertrophy

RVOTO Right Ventricle Outflow Tract Obstruction

TOF Tetralogy of Fallot

VSD Ventricular Septal Defect

Acknowledgements

I would first of all like to thank my advisor, Professor Christian Vergara, for all his teachings and insightful feedbacks. Thank you also to my co-advisor, Doctor Ivan Fumagalli, for his help and advice throughout the whole project.

I would also like to thank Doctor Stefano Marianeschi and the Niguarda Hospital of Milan for their interest in our study and for supplying us with the medical data.

Thank you to my parents, for always believing in me and for being by my side rooting for me every day, and to my grandmother, because I know how proud she would be.

Thank you to Matteo for his daily support and for sharing this journey with me and making it so much better.

Finally, I would like to thank my closest friends: Gloria, for basically being my sister, Chiara, Alessandra and Eleonora, because I know I can always count on them, Martina and Sara, for the friendship and shared experiences in these five years.

